Across the natural sciences, most phenomena trace back to elementary dynamics that occur at extremely small atomic distances (1 Å = 10^{-10} m) and, at the same time, develop over ultrafast femtosecond time scales (1 fs = 10^{-15} s). To understand and harness these basic processes, such as a transition of a single molecule for example, direct observation and immediate control are vital.

To that end, this work demonstrates the first femtosecond videography as well as the first ultrafast electronic and structural control at the atomic scale. Lightwave-driven scanning tunneling microscopy (STM) allows us to track single-molecule vibrations, steer molecular transitions with atomic forces and resolve angstrom-scale near fields – all with sub-optical-cycle temporal precision, for the first time.

We apply tip-confined terahertz waveforms in STM to drive one-electron tunneling through a select orbital of a single molecule with combined 0.6 Å and ~100 fs spatio-temporal precision. This process resolves the first single-molecule femtosecond snapshot and tracks a vibration of an individual molecule in space and time. Moreover, to control matter dynamically in the most direct way, we introduce femtosecond atomic forces as a novel stimulus that steers structural motion locally, with atomic precision. The forces – derived from tailored tip-confined electric-field waveforms – push key atoms of a molecular switch to coherently steer a select ultrafast structural rotation. This motion can be driven so vigorously that the switching rate of the molecule is modulated by up to 39%, on the femtosecond scale. To observe such unidirectional transitions, we implement a novel single-shot detection strategy: Ultrafast action spectroscopy monitors every individual switching event of the molecule to resolve the statistics with an accuracy of 10^{-4}. Finally, we measure the first quantitative, atomically confined near-field waveform, introducing a direct spatio-temporal access to light-matter dynamics at atomic length scales.

These novel experiments set the stage for a variety of exciting future studies across the natural sciences, including attosecond and single-spin microscopy and videography of complex reactions, elementary energy exchange as well as local phase transitions that involve order and correlations in solids.

Cover: The tip of an ultrafast STM (top-left) hovers over a molecular switch (bottom, connected red and black spheres). Femtosecond atomic forces (shock waves) induce vigorous motion of a select atom (red sphere) of the molecule to control its reactivity on ultrafast time scales.

Universität Regensburg
Institut für Experimentelle und Angewandte Physik
Prof. Dr. Rupert Huber & Prof. Dr. Jascha Repp

Dominik Peller Femtosecond videography and control of single-molecule dynamics with atom-scale lightwaves

Dominik Peller

Femtosecond videography and control of single-molecule dynamics with atom-scale lightwaves

Femtosecond videography and control of single-molecule dynamics with atom-scale lightwaves

Dissertation
zur Erlangung des Doktorgrades der
Naturwissenschaften
(Dr. rer. nat.)
der Fakultät für Physik der Universität Regensburg

vorgelegt von
Dominik Peller
aus Landshut
im Jahr 2020

Das Promotionsgesuch wurde eingereicht am: 8. Juni 2020.
Die Arbeit wurde angeleitet von: Prof. Dr. Rupert Huber.

Prüfungsausschuss:	Vorsitzender:	Prof. Dr. Klaus Richter
	1. Gutachter:	Prof. Dr. Rupert Huber
	2. Gutachter:	Prof. Dr. Jascha Repp
	weiterer Prüfer:	Prof. Dr. Isabella Gierz-Pehla

To my parents.

Acknowledgements

I have spent marvelous years studying, doing research, gaining professional experience and having a great time in Regensburg. First and foremost, I need to thank wonderful friends and great colleagues who I am in debt to for their invaluable companionship.

Rupert Huber and Jascha Repp have been a dream team of mentors.

Rupert has inspired my entire perspective on science and profession. He revealed the fascination of ultrafast phenomena to me, both through intense dialogue and hands-on in our labs. He has always been available, encouraged the most fruitful teamwork one could imagine, and supported me on a professional as well as personal level to a unique extent. In particular, I am grateful for the countless mind-opening experiences he enabled, such as conference trips and my semester abroad, which I benefit from way beyond science. Most of all, I appreciate that Rupert promotes a strong effort, and genuinely honors individual success.

Jascha has always made time to directly teach me the exciting physics of atomic systems and tunneling microscopy, and share his precise and fair take on science. He is known for being constantly available to give hands-on support, provide inspiration, or solve any lab issue, all in an instructive and cheerful way. What I am most grateful for is that Jascha has always created a warm and welcoming atmosphere, has often openly valued my contributions to our projects, and has given me encouraging personal feedback, from the early days that we worked together on.

The recent years would not have been nearly as enjoyable without the many wonderful labmates, colleagues and students, many of whom became close friends of mine.

Carmen Roelcke and Lukas Kastner have been great lab companions. Most of this work is our common achievement, and I am very grateful for the trustful and humorous way we have been working together over the recent years. Besides, what I've always cherished most was grabbing a cup of refreshing coffee in the morning with Carmen, and rocking our street bikes with Lukas.

Also, intense research and good times with Thomas Buchner, Alexander Neef, Florian Albrecht and Johannes Hayes have contributed to this work, and have been very enjoyable.

The projects I shared with Philipp Merkl were extremely fun, too.

Working with our collaboration partners Nikolaj Moll, Franco Bonafé, Dominik Sidler, Michael Ruggenthaler and Ángel Rubio was extremely pleasant and instructive.

Also, I am very grateful to Tyler Cocker, who taught me how to handle an optics lab, for our teamwork and staying friends beyond.

For many years now, I have followed a curriculum similar to that of Fabian Mooshammer. From our first joint research project till today, it was good to tackle all these challenges together.

Weekly climbing with Markus Plankl and hiking with Simon Maier has been very refreshing.

In particular, I have greatly enjoyed all the hilarious evening walks with Christian Meineke.

In addition, I would like to thank everybody else who I worked together with, but have not mentioned by name here. This includes the entire Huber and Repp research groups as well as our permanent staff. Especially Ulla Franzke, Martin Furthmeier, Andreas Pöllmann and Christoph Rohrer have been invaluable colleagues who enable all this research with their reliability and precision.

Apart from the university context, I am incredibly thankful for all the personal support I have received, and for the moments I could share with wonderful friends.

Thanks to my parents for their pure love and truly unconditional support from home.

Thanks to Max Held and Fabian Diewald for all our precious adventures. I treasure the passions and depth that I share with Max. And all the mountain trips with Fabian that are too silly to experience with anybody else are just priceless.

Thanks to Verena Berthold for our long-term marathon friendship.

Thanks to Elif Ziehmer for you very special compassion.

And thanks to H. G. S. and friends for pointing to moment.

In addition, particular thanks go to Christian Meineke, Lukas Kastner, Carmen Roelcke and Johannes Hayes for proofreading my thesis, to Rupert Huber and Jascha Repp for assessing this work, and to Klaus Richter, Rupert Huber, Jascha Repp and Isabella Gierz-Pehla for conducting my oral examination.

Contents

1 Introduction: Elementary dynamics in nature **1**

2 Ultrafast videography and electronic control of single molecules **9**

2.1 Lightwave-controlled scanning tunneling microscopy 14

2.2 Femtosecond snapshots of individual molecules' orbitals 28

2.3 Single-electron injection triggers ultrafast structural dynamics 44

3 Femtosecond atomic forces choreograph reactions of a molecular switch **53**

3.1 Single-shot detection of unidirectional switching events 61

3.2 Tip-confined fields coherently control femtosecond switching dynamics 69

3.3 Femtosecond forces selectively steer key atoms 81

4 Quantitative sampling of atomic-scale near-field waveforms **89**

4.1 Interference sampling using a single-molecule voltage sensor 91

4.2 Near-field waveform shaped by plasmonic features 95

4.3 Quantum-mechanical simulation of atom-scale light-matter interaction 109

5 Conclusion and outlook **117**

Scientific record **129**

References **135**

yoku mire ba
nazuna hana saku
kakine kana

When I look carefully ...
Nazuna *is blooming*
by the hedge!

— Basho (Japan, 1644–1694)

1 Introduction: Elementary dynamics in nature

The natural sciences have always evolved around one central question: *How does nature work?* Analytical thinking seeks insight by dissecting the world into its elementary building blocks. Therefore generations of scientists have discovered the microscopic processes at the heart of physical phenomena, (bio)chemistry and life. Intriguingly, the closer we look, the fainter do the boundaries between these disciplines appear. Often elementary processes and their dynamics – the origin of function – are not specifically attached to a certain field of research.

For example, reactions and transitions of atoms and molecules are the pivot of chemistry. Understanding how these building blocks of matter interact, separate and form new connections, is a prerequisite for many of today's industries, including polymer and petrochemistry, agriculture and the pharmaceutical industry. In detail, the physical laws of quantum mechanics describe the relevant atomistic excitations and respective molecular motion[1]. Biology, moreover, examines how such reactions can cooperate and balance each other to induce function in living cells.

Quantum coherence is another phenomenon that is closely related to nanoprocesses across all natural sciences. For example, coherently ordered states in solids give rise to non-trivial phases of matter: Phase coherence seems to lie at the heart of exotic states in many correlated materials[2]. From a technological point of view, coherent control of various degrees of freedom in condensed matter sets the stage for future information processing[3–6] and green-energy solutions[7]. Intriguingly, on the other hand, current research investigates to what extent life makes use of quantum coherence in the

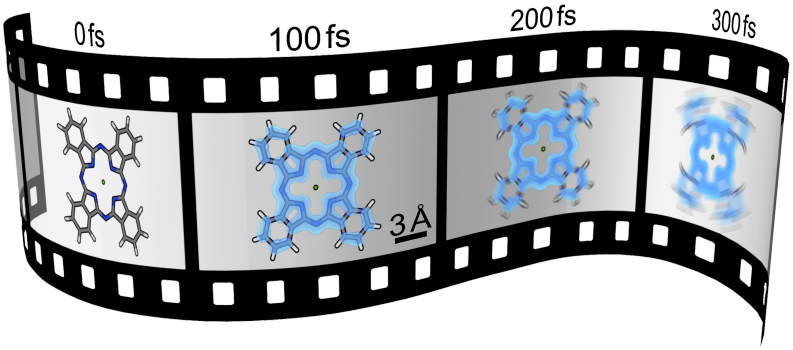

Figure 1.1 | Ultrafast molecular movie. Schematic illustration of a slow-motion movie (film strip) in which a single molecule (skeletal model) is time-resolved stroboscopically. The individual frames combine sub-angstrom and femtosecond spatio-temporal resolution, such that ultrafast dynamics – e.g. structural motion (blur) subsequent to orbital charging (blue glow) – can be directly observed.

bio-processes that evolution has shaped[8–11].

Moreover, energy conversion of atomistic degrees of freedom of matter are our microscopic key to harnessing elementary dynamics at will, across the disciplines. An essential question in catalysis, for example, is how a single adsorbed molecule exchanges vibrational quanta and hot electrons with a surface[12,13]. At the same time, optoelectronics provide a route to improving the efficiency of conventional solar cells, namely excitonic energy conversion in single molecules via singlet fission[14,15]. Evolution, however, has developed light-harvesting complexes with spectacular quantum efficiencies close to unity[9]. In this spirit, the elementary processes of life will likely fuel bio-inspired nanoengineering in the future.

A detailed understanding of such nanoprocesses is key to all modern life and natural sciences as well as nano- and biotechnologies. Fortunately, today, the elementary structure of the nanocosm can be directly imaged with highest-resolution scanning-probe, optical and electron microscopes (Nobel prizes in physics 1986 as well as in chemistry 2014 and 2017). While a spatial resolution down to the atomic length scale ($1\,\text{angstrom} = 1\,\text{Å} = 10^{-10}\,\text{m}$) is possible, the established microscopy methods in general only provide static images. But the nanoworld is in permanent motion. Still images are not sufficient to fully understand its excitations, atomistic transitions and coherent dynamics, as well as their consequences for macroscopic function of biological, chemical and physical systems.

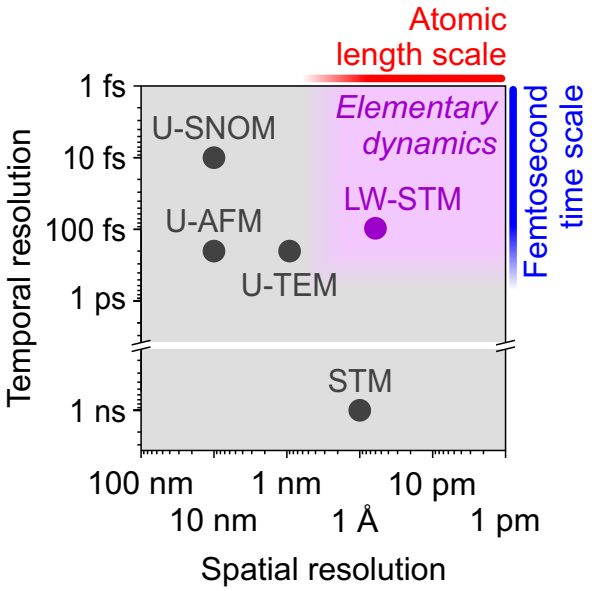

Figure 1.2 | Ultrafast microscopy techniques. Ultrafast scanning near-field optical microscopy (U-SNOM[16]), atomic force microscopy (U-AFM[17]) and transmission electron microscopy (U-TEM[18]) have demonstrated a temporal resolution down to a few femtoseconds, but lacked simultaneous atomic precision. Angstrom spatial scales have been resolved by scanning tunneling microscopy (STM[19]), but not faster than a nanosecond. Lightwave-driven STM (LW-STM[20], this work) provides the first access to the combined atomic and femtosecond spatio-temporal scales of elementary dynamics.

Instead, one would need to follow the interplay of these elementary processes in moving images, resolved in space and time simultaneously. And since many of these dynamics occur on extremely short time scales (1 femtosecond = 1 fs = 10^{-15} s), two central challenges must be mastered simultaneously: One needs an ultrafast[a] microscope that delivers atomic spatial and femtosecond temporal resolution at the same time, allowing one to record ultrafast movies of atomic and molecular dynamics (Fig. 1.1).

Several techniques have accessed either of these scales separately (Fig. 1.2). But so far, no microscope has combined the spatial *and* temporal precision necessary to directly watch ultrafast atom-scale dynamics in femtosecond movies. To really grasp the nanocosm with its vast richness of dynamics and transitions, a revolutionary new approach is required that opens the door to atomic femtosecond videography. This summarizes the central achievement of my thesis.

In this work, I will introduce how we recorded the first true *single-molecule movie*. I will demonstrate that combining atomically resolved tunnel microscopy with ultrafast lightwave control allows us to visualize individual molecules in motion, directly

[a]The conventional term "ultrafast" means faster than 1 picosecond = 1 ps = 10^{-12} s.

in femtosecond snapshots and movies, for the first time[20]. Moreover, I will present a novel mechanism to *control* atom-scale structural dynamics in the most direct and selective way, namely via femtosecond atomic forces[21]. Finally, I will demonstrate quantitative measurements of atom-scale near-field waveforms, which open the door to an uncharted territory of non-classical light-matter interaction on combined sub-cycle temporal and atomic length scales[22]. Together with related works[23], these recent milestones have triggered a whole new vibrant field of research[24–28]. In my thesis, I will outline the physical ideas behind lightwave-driven scanning tunneling microscopy (STM), summarize the technical cornerstones of implementing such an ultrafast microscope, and demonstrate experiments which show that this concept solves a number of challenges of modern nanoscience.

Chapter 2 will start with a brief introduction to the prospects and limits of state-of-the-art atomic tunneling microscopy on the one hand, and femtosecond nanophotonics on the other. This will illustrate that combining the core principles of these two fields promises a route towards molecular movies, coherent atomic control and light-matter dynamics at the limits of space (one atom) and time (one optical cycle). To this end, we build on a concept recently developed in the domain of ultrafast photonics: While light-driven dynamics are often governed by photonic quantum excitations, the idea to, in contrast, make use of the carrier wave of light to directly steer electron motion has paved the way for so-called lightwave electronics[5,29–35]. In this spirit, we design a lightwave-driven tunneling microscope where, similarly, ultrafast tip-confined electric-field waveforms steer electron dynamics on sub-cycle timescales.

I will outline the physical background of lightwave-driven STM and deduce the necessary technical requirements to implement the first low-temperature femtosecond STM[b] (section 2.1). We put our microscope to the test by imaging single molecules, where we can successfully record state-selective snapshot images of individual molecular orbitals, for the first time (section 2.2). Analyzing the spatial and temporal definition of the ultrafast current shows that sub-cycle lightwave control allows us to confine a single-electron tunneling event with combined sub-Å and ~100 fs spatio-temporal precision.

[b] Throughout this work, for simplicity, "STM" abbreviates both "scanning tunneling microscopy" as well as "scanning tunneling microscope", depending on the respective context.

This process enables us to charge organic molecules with a single electron, providing an impulsive trigger with femtosecond definition. In a pump-probe experiment, we time-resolve the response of the molecule to this electronic excitation and find that it entails an ultrafast structural motion of the molecular frame. For the first time, we track single-molecule vibrations directly in the time domain, probed locally and with femtosecond accuracy (section 2.3). When we alter the molecular species or the substrate, we observe motion patterns with the same phase relation, but different oscillatory frequencies between 0.3 THz and 0.5 THz. Our findings suggest that the observed mode is a frustrated vertical vibration of the molecule within its van-der-Waals adsorption potential on the surface. This clear observation of single-molecule motion opens the door to femtosecond videography of all kinds of atomic-scale elementary excitations.

At the same time, deliberate *control* of ultrafast atomic motion along a select degree of freedom has not been available so far, owing to the lack of an ideal control stimulus. While electronic charging induces motion in a rather indirect way, in order to selectively steer the course of atom-scale excitations, or even choreograph a chemical reaction, a novel control mechanism is required. To this end, in chapter 3, I will introduce femtosecond atomic forces as a new ultimate stimulus to directly steer select atoms of a nanosystem, coherently and locally, with sub-cycle precision. The ultrafast force is provided by a nano-confined electric-field waveform. We demonstrate the new dynamical force by means of a prototypical functional nanodevice, namely a single-molecule switch.

To examine the impact of the force on the switch, we develop a novel single-shot detection scheme that registers every single switching event of the molecule, separately for different directions (section 3.1). In this way, the statistics of transitions and reactions, which are purely probabilistic processes by nature, can be directly resolved, with simultaneous atomic and femtosecond resolution.

We find that, while leaving the electronic system in the ground state, atomically strong fields can locally and coherently steer a frustrated rotation of the molecule. Notably, we can drive amplitudes large enough to modulate the reaction probability of the switch by up to 39%, on the femtosecond scale (section 3.2). Moreover, the switch only reacts to forces when applied at specific regions of the molecule. Density functional theory (DFT) calculations show that these regions coincide with the key

atoms that determine the delicate energetics of the switch (section 3.3). In addition, our simulations confirm that when local fields deflect these key atoms, the molecular rotation can be controlled selectively. This illustrates the atomic spatial definition of the ultrafast force and demonstrates that it serves as an ideal local stimulus to coherently steer select degrees of freedom in atom-scale functional devices.

A full femtosecond movie of the locally driven switching probability summarizes the full impact of the sub-cycle atomic force. Separately for the different switching directions, our reaction microscope resolves the evolution of a single-molecule's reactivity in space and time, triggered by one quantum of charge, and coherently steered on femtosecond scales via local atomic forces.

These experiments demonstrate that tip-confined light fields can serve remarkable technical purposes, such as introducing new avenues for atom-scale videography and control. At the same time, even the fundamental properties of light-matter interaction at these spatio-temporal scales have a significant impact in numerous related domains that make use of nano-photonics. Prominent examples are (bio)chemical[36] and medical sensing[37], photoenergy harvesting[38,39] and nano-spectroscopy[16,40,41]. Different techniques have resolved sub-wavelength near fields in the time domain to observe light-matter interaction at the nanoscale[16,42]. Down at the dimensions of individual atoms, though, it has been predicted that near fields exhibit angstrom-scale structure, and may be strongly influenced by non-classical ultrafast quantum dynamics[43,44].

Such processes are probably key to light-matter interaction at the elementary scale of nature's building blocks, and therefore of utmost importance for nanoscience and technology. But for the lack of a quantitative atomic-scale near-field sensor, these local fields and their interactions have remained experimentally entirely uncharted territory so far.

We tackled this challenge and developed a technique to resolve the first atom-scale femtosecond waveform, directly calibrated in absolute units. Chapter 4 will introduce how we make use of a single-molecule switch as a gauged local field detector. In a tailored pump-probe scheme, tip-confined femtosecond fields translate into a molecular reaction rate that we measure and gauge self-consistently (section 4.1). As a result, we sample the first quantitative atomic near-field waveform, with femtosecond precision and calibrated in units of volts (section 4.2). The oscillatory near field

exhibits a number of distinct features remarkably different from the incident far-field waveform. We find that most of these characteristics are reproduced in detail by a classical numerical simulation of the plasmonic dynamics in our geometry.

Remarkably, classical electrodynamics can describe the near-field waveforms even quantitatively, with a deviation of the local peak field of only 2%, which is 3.5 mV in absolute values. This comes as a major surprise since the tip-confined fields drive extreme electron tunnel rates of approximately one charge per 100 fs. In such a scenario, one might in principle expect severe back-action of the carrier dynamics on the local fields, as well as strong screening effects from polarization and possibly accumulated charge imbalance[44]. To obtain a thorough understanding of the involved non-classical processes, we calculate the atom-scale light-matter interaction within our tunnel junction in a full quantum-dynamical simulation (section 4.3). The ab initio study confirms the assumptions in our sampling method, and shows that the accuracy of our near-field detection derives from a fundamental quantum-mechanical principle. This first observation of atomic femtosecond light fields opens the door to a new experimental domain of non-classical light-matter dynamics at the ultimate spatio-temporal scales.

Chapter 5 concludes my thesis with a short summary of our experimental findings and provides some perspectives on exciting physics that may be resolved in future lightwave STM studies.

Ultrafast videography and electronic control of single molecules

2

A vivid imagination of molecules that move and collide, interact, maybe form chemical bonds, and eventually separate again has inspired curious scientists over centuries. The dream of watching a single molecule move[45] has stimulated research and technology, has given rise to technical breakthroughs in imaging and spectroscopy, and served as a mission statement for major research facilities all over the globe. In this chapter, I will present the route that allowed us to resolve the first molecular movie, using a newly developed microscope that can unveil the inner structure of a single molecule with ultrafast temporal precision. First, I will introduce the key ideas and today's main applications of two major fields of research: Atom-level microscopy, on the one hand, and ultrafast lightwave control of matter, on the other.

Atom-scale tunneling microscopy. Scanning tunneling microscopy has initiated a new era in nanoscience, providing tools to probe the electronic properties of nanoobjects with atomic resolution[46]. Atom-level imaging, once considered a dream[47], has fundamentally changed the course of surface science and engineering. Previously unknown atomic surfaces could be resolved[48], and new quantum structures could be assembled atom by atom[49–51]. Also dynamical interactions and excitations of a variety of systems have been probed, including molecular vibrations[52] and single-atom magnetism[53,54]. In particular the ability to spectroscopically resolve electronic states with atomic resolution has boosted research on two-dimensional platforms[55,56], atomistic information storage[57,58] and strongly correlated materials[59].

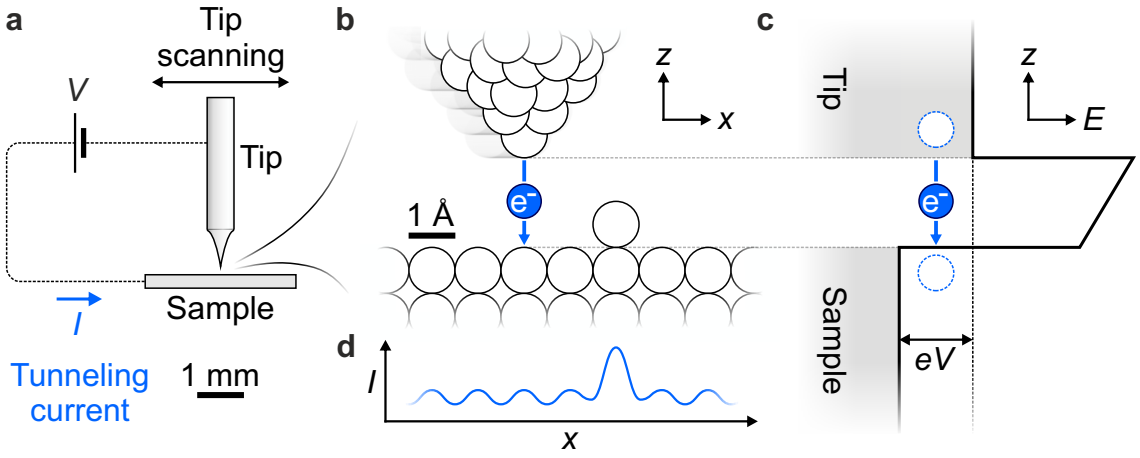

Figure 2.1 | Schematic of scanning tunneling microscopy. a, STM circuit diagram. When a bias voltage, V, is applied between tip and sample, electron tunneling across the atomic-scale junction (**b**) drives a current, I (blue arrows). **b**, Atoms of the tip apex and sample surface are sketched as circles. Electrons tunnel through the vacuum gap while the tip is scanning across the sample. **c**, A one-dimensional diagram of the potential landscape across the tunneling junction illustrates occupied electronic states (gray) in tip and sample, separated by a vacuum barrier. When the STM is electronically biased, a voltage window eV opens up where electrons can tunnel from occupied tip states into empty sample states, or vice versa. **d**, Recording the tunneling current as a function of tip position, atom-scale features of the sample surface such as an individual protruding atom can be sensed.

The basic idea in scanning tunneling microscopy is to utilize an atomically sharp metal needle as a movable probe, which controls a tunnel current confined to sub-Å dimensions (Fig. 2.1). This tip is brought close to a sample until the electronic wave functions of tip apex and sample overlap. When a bias voltage is applied between tip and sample (Fig. 2.1a), electrons can tunnel across the junction, giving rise to a current that depends sensitively on the geometry and the energetics of local electronic states, down to the atomic scale (Fig. 2.1b).

In a one-dimensional picture, the vacuum gap between tip and sample constitutes a potential barrier that separates tip and sample electronic states (Fig. 2.1c). Biasing of this landscape by a voltage V offsets tip and sample states by eV (e, elementary charge), and thereby opens a so-called "bias voltage window" where electrons can tunnel from occupied tip into empty sample states, or vice versa. The tunneling current thereby encodes information about the local properties of the sample. Consequently,

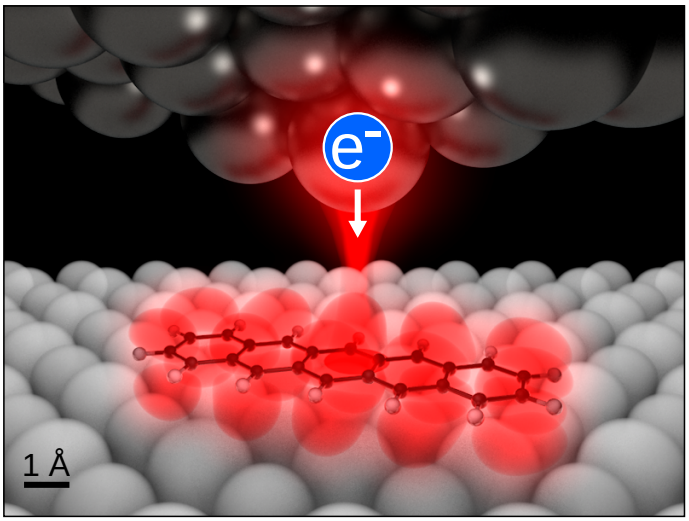

Figure 2.2 | Single-molecule STM. Illustration of electron tunneling between the tip apex (top spheres) and a single molecule adsorbed on a flat substrate (bottom spheres). When the electronic wavefunctions of tip and molecule (red) overlap, electron injection (blue symbol with arrow) can be steered with sub-molecular spatial precision.

when the tip is scanned across the sample and the tunnel current is recorded as a function of tip position, atom-scale maps of the sample topography, or other local observables, can be obtained (Fig. 2.1d).

In particular, imaging of individual molecules has accessed the elementary building blocks of biology and chemistry, one by one. In contrast to ensemble studies, tunneling microscopy can observe single molecules in their unique surroundings[60,61], and even synthesize[62] and manipulate them[63], by virtue of a movable source of tunnel current. When a molecule is approached by the tip, at a certain distance, the electronic states around the very front-most apex atoms begin to protrude into the molecule (Fig. 2.2). Then electrons can tunnel into an unoccupied molecular orbital, selected via external biasing. Moving the tip across the molecule, the tunneling current directly encodes the density of the molecular orbital, with a spatial resolution determined by the electronic definition of the atomically sharp tip apex.

Since its invention the STM has provided a direct view into the realm of atoms and molecules. While this technique now routinely provides static images of atomic surfaces, recording ultrafast movies of the nanoworld *in motion*, however, has remained a dream. This is because conventional tunnel microscopes cannot define tunnel currents faster than a nanosecond[19], as they are limited by the bandwidth of the electronic circuitry. To resolve atom-scale dynamics that occur on the femtosecond scale and even faster, the temporal resolution of tunnel microscopes needs to be improved by orders of magnitude.

Ultrafast nano-photonics. Meanwhile, the idea to control matter with ultrashort light pulses has prompted a vivid field of research exploring light-matter interaction on femtosecond time scales. Ultrafast photonics has started to examine processes faster even than a single field cycle of light. To this end, electronic motion has been directly steered via the oscillating carrier wave of tailored light pulses – a principle often dubbed lightwave electronics. In particular, phase-stable femtosecond pulses have driven electron-ion recollision in gases[29,30] and directly controlled ultrafast internal dynamics in matter[31–33], including Dirac currents in topological surface bands[34] and spin degrees of freedom[5,35]. Meanwhile, the ongoing innovation of phase-locked high-field sources that generate few- to half-cycle waveforms in the terahertz (1 THz $= 10^{12}$ Hz) frequency range is opening new avenues for ultrafast electric biasing of condensed matter.

Moreover, tailored plasmonic nanostructures including antennas[35,64–66], nanogaps[67–69] and tips[70–74] can confine and enhance electromagnetic waveforms in extremely sub-wavelength volumes (Fig. 2.3). Exploiting such strong near fields has improved a variety of optical processes across scientific domains. Plasmonic fields have, for example, pushed spectroscopic sensitivity in chemical[36] and medical[37] sensing, enhanced photoenergy harvesting[38,39] and paved the way for nanosources of electrons[75]. Additional *temporal* control of such locally oscillating, ultrafast fields provides direct access to a plethora of nanooptical dynamics. For example, intense near fields have steered the emission of electrons from sharp tips, exploring a fascinating regime of light-matter interaction at the crossover between ballistic acceleration[72], interferometric backscattering[70], quiver motion[71], and Rabi oscillations[73]. Technologically, near-field confinement at sharp tips has facilitated femtosecond nanoimaging[16,18,23–25,76] and -spectroscopy[16,40,41,76].

Yet, even though these phenomena fundamentally rely on atom-scale light-matter interaction, many aspects of ultrafast near fields are not accessible by experiments, or have even remained completely open questions. For example, the influence that a single atom on a surface can exert on the amplitude and the spatial distribution of local near fields – a crucial issue for surface enhanced Raman spectroscopy – is a matter of current debate. While modern theory approaches predict that near fields can be drastically influenced by single-atom structural features[43], quantitative experimental evidence has been out of reach so far.

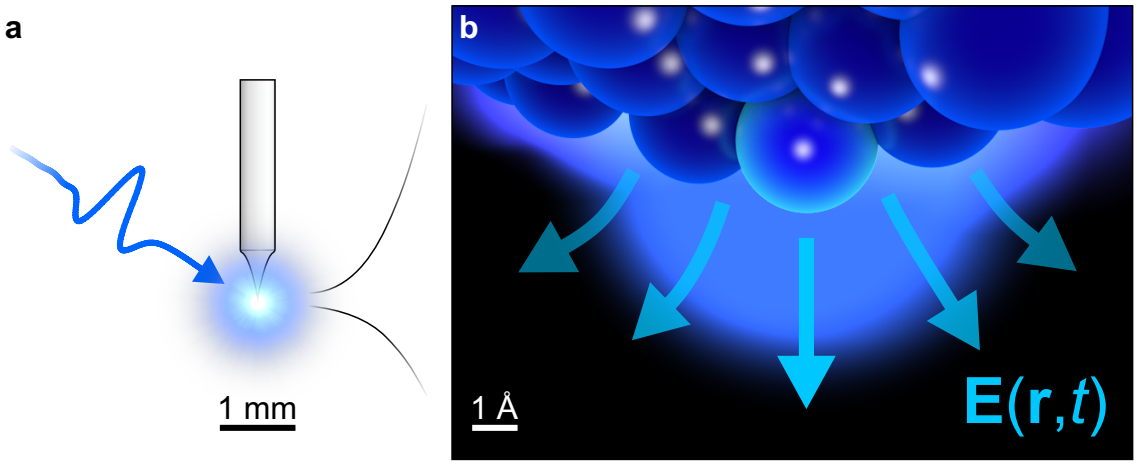

Figure 2.3 | Tip-confined near fields. a, When electromagnetic waves (blue waveform) interact with metallic objects, plasmonic motion of the surface electrons can cause strongly enhanced near fields in the vicinity of sharp geometric features. These near fields can be structured with extreme sub-wavelength definition, down to even atomic dimensions. **b**, Such atomistic femtosecond dynamic fields (arrows), i. e. in the vicinity of an irradiated tip apex, entail rich physics, ranging from ballistic to quantum light-matter interaction. In particular, lightwaves can be utilized to control local ultrafast electron dynamics.

Most fascinatingly, the ultrafast dynamics of atom-scale light-matter interaction hold a wealth of possibly non-classical phenomena yet to be explored by experiments. This regime is almost entirely uncharted territory: bare understanding in which scenarios atomic near fields obey classical electrodynamics or quantum-mechanical laws has mostly relied on theoretical modeling so far[43,44].

In the following I will demonstrate that combining atom-scale tunnel microscopy with femtosecond lightwave control allows us to solve a number of challenges across nanoscience and technology at once. Not only can tip-confined near fields provide tunnel microscopy with femtosecond temporal imaging resolution (this chapter), but this combination also introduces new mechanisms to control matter coherently, at the atom level (chapter 3). And, most fundamentally, this alliance grants us seminal access to atomic light-matter interaction at the elementary scales of space and time, opening our eyes to the interplay of (even nonclassical) radiative and matter dynamics (chapter 4).

2.1 Lightwave-controlled scanning tunneling microscopy

During the last decades, a number of attempts have aimed at improving the temporal resolution of scanning tunneling microscopy with the aid of ultrafast light pulses. Figure 2.4 illustrates the different approaches. While all-electronic tunneling microscopes (Fig. 2.4a) are limited to the nanosecond scale by their finite bandwidth[19], the toolbox of ultrafast photonics can provide much faster stimuli. The central goal has been to introduce an ultrashort trigger to the microscope junction in order to obtain temporal tunnel control via optical techniques.

In the first attempt at combining ultrafast lasers with STM, optical pulses were used to induce a surface photovoltage that momentarily increases the tunnel current[77]. This seminal work was followed by a number of experiments that combined ultrafast optics and tunnel microscopy in different ways.

In some cases, particular structures were designed in order to generate fast voltage transients, and subsequently propagate them to the STM junction. As a prominent example, photoconductively gated STM incorporated photoconductive switches into the STM electronics (Fig. 2.4b). Ultrashort laser pulses were employed to generate carriers and thereby close the tunneling circuitry transiently[78]. Later it was shown, however, that this approach is limited by capacitive charging instead of providing actual tunnel control[79].

Other designs generated fast field transients directly on the substrate and used striplines to propagate the pulses to the STM junction[80] (Fig. 2.4c). This technique known as junction-mixing STM could confine tunnel currents to a combined nanometer and picosecond window. Yet, the major limitation is that this design drastically restricts possible samples, because all experiments must be performed on a transmission line. Altogether, all schemes where voltage pulses are propagated into the tunneling gap via transmission elements suffer from limited electronic bandwidths.

Further approaches have directly focused laser pulses at optical frequencies onto the junction of an STM, like in the seminal experiment mentioned above[77] (Fig. 2.4d). From a technical point of view, all of these attempts suffered from an ever-present concern, which is optically induced heating and, hence, periodic tip expansion that

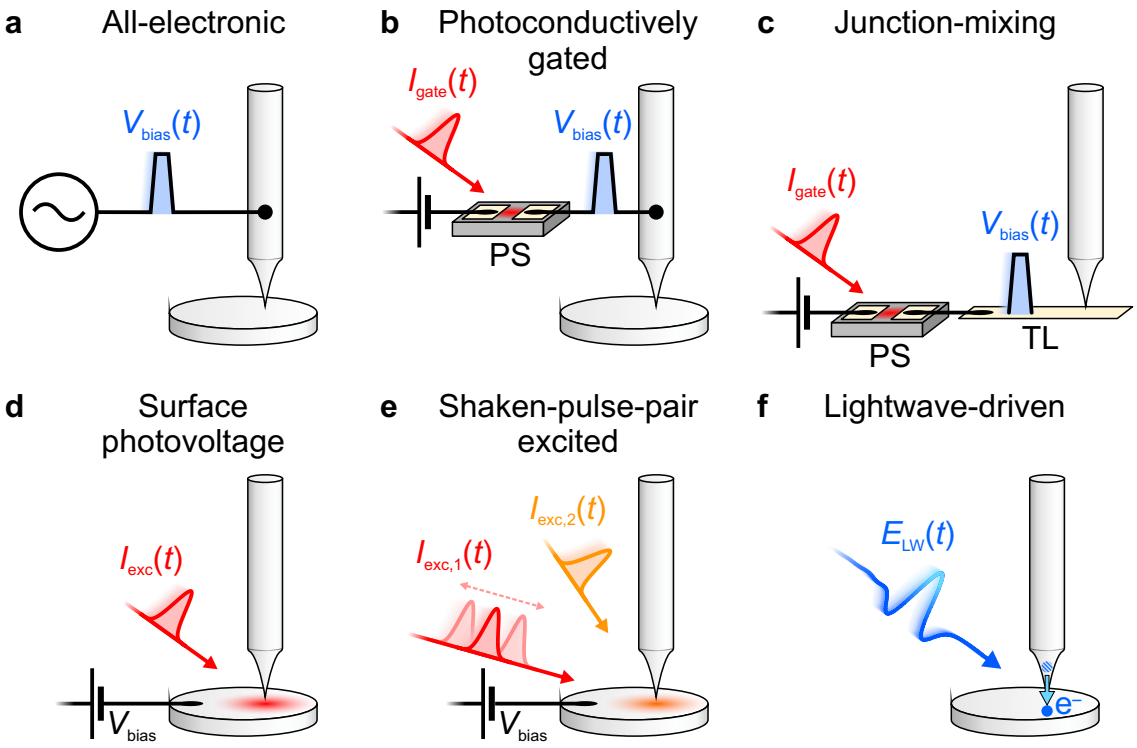

Figure 2.4 | Fast STM techniques. Schematic diagrams illustrating techniques that have aimed at introducing ultrafast temporal resolution in STM. **a**, All-electronic biasing employs an arbitrary wave generator to pre-compensate the dispersion of the electronic circuitry, and directly apply voltage pulses $V_{\mathrm{bias}}(t)$ to the STM junction. **b**, In photoconductively gated STM, optical excitation of a photoconductive switch (PS) transiently closes the biasing circuitry. This scheme is supposed to convert an optical gating pulse $I_{\mathrm{gate}}(t)$ (intensity envelope) into a bias voltage pulse $V_{\mathrm{bias}}(t)$. **c**, Similarly, junction-mixing STM generates a voltage pulse with a photoconductive switch. Here, $V_{\mathrm{bias}}(t)$ is coupled to and propagated along a transmission line (TL) that serves as a substrate. **d**, Pulsed optical excitation ($I_{\mathrm{exc}}(t)$, intensity envelope) of the sample can induce a surface photovoltage that affects the tunnel current on ultrafast time scales. **e**, Shaken-pulse-pair STM employs pulse pairs $I_{\mathrm{exc},1}(t)$ and $I_{\mathrm{exc},2}(t)$ (intensity envelopes) mutually delayed by an oscillatory time interval to obtain temporal resolution while reducing artifactual tip expansion. **f**, In lightwave-driven STM, a phase-stable electromagnetic waveform $E_{\mathrm{LW}}(t)$ directly adds a bias field to the tunnel junction. Thereby electron tunneling (blue arrow) can be steered with sub-cycle temporal accuracy.

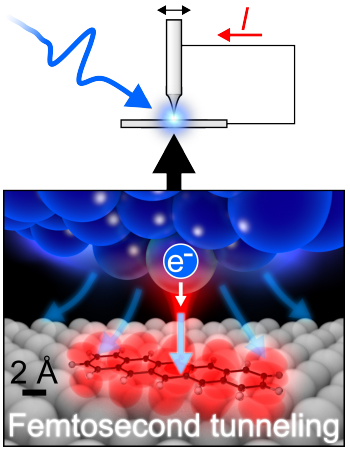

Figure 2.5 | Lightwave scanning tunneling microscopy. When lightwaves are coupled to an STM (top), they can induce near fields in the tunnel junction (bottom). These ultrafast fields may be exploited to steer local electron tunneling with femtosecond temporal definition, and even control atom-scale objects directly and coherently. Measuring the ultrafast tunnel current, I, driven through a molecular orbital (red), for example, allows us to probe single-molecule dynamics with combined femtosecond and atomic spatio-temporal resolution.

overwhelms all other effects. To a certain extent, technical tricks can extract non-thermal transient signals[81,82] (Fig. 2.4e). Of particular interest are excitations that cause a surface photovoltage since this can directly modify the tunneling current.

But still, the full dynamics locally driven by the light pulses can be hard to interpret. Indeed, local electron heating and multiphoton excitation may drive the electronic systems of tip and sample out of equilibrium on short time scales. Harnessing such a photoexcited STM to extract the pure dynamics of the sample might be rather complex though: In contrast to steady-state STM where the observables directly reflect sample properties, in a photoexcited STM, non-equilibrium dynamics of microscope and sample need to be disentangled somehow. In addition, at optical frequencies, metallic tips and substrates feature plasmonic resonances that impede straightforward coupling of ultrashort pulses with large bandwidths to the junction.

To avoid all these drawbacks, we pursue a different approach (Fig. 2.4f). The key idea of lightwave-controlled STM (or short: lightwave STM) is to directly steer electron tunneling in an STM by the carrier wave of an ultrashort light pulse. Figure 2.5 illustrates this process. When suitable pulses are focused directly onto the tunneling junction, their carrier wave translates into a quickly oscillating electric-field distribution at the tip apex. This near field is intended to act classically, adding an ultrafast AC bias potential between tip and sample, which would allow direct control of femtosecond tunnel processes. When an electric circuit between tip and sample is closed and pulses are injected repeatedly, the tunneled charges should add up to a measurable current, I, that directly encodes the ultrafast tunnel dynamics of the

involved electronic states.

This process has been successfully employed to image carrier dynamics in semiconductor nanodots with a combined 2 nm and 500 fs spatio-temporal resolution[23]. Whereas this seminal experiment drove huge tunnel currents of thousands of electrons per pulse, we aim to enter a novel regime of lightwave-driven tunneling. We want to control *state-selective* tunnel dynamics of a *single* electron with combined *atomic* spatial and *femtosecond* temporal precision. In the following I will derive the requirements to achieve this ambition.

Ultrafast bias fields via terahertz waveforms. In general, light-matter interaction manifests in between the two poles of perturbative quantum absorption and classical, field-driven dynamics (Fig. 2.6). For a given scenario where electromagnetic waves act on a system that provides an electronic transition, the Keldysh parameter, κ, quantifies the balance between these two regimes[83]:

$$\kappa = \sqrt{\frac{\epsilon}{2U_\mathrm{P}}} = \frac{\sqrt{2m\epsilon}\,\omega}{eE}. \tag{2.1}$$

This quantity essentially describes the ratio between the excitation or ionization energy ϵ of a system and the ponderomotive energy $U_\mathrm{P} = \frac{e^2E^2}{4m\omega^2}$, which is the kinetic energy that a free electron would acquire by field-induced acceleration during one optical cycle. m and e are the electron mass and elementary charge, E describes the electric-field amplitude and ω denotes the frequency of the driving field. Also, one can show that κ denotes the ratio between the ballistic tunneling time and the oscillation period. Intuitively, at high optical frequencies ω, the photon energy $\hbar\omega$ is large and thus, (multi-)photon absorption is likely (Fig. 2.6a). This perturbative regime $\kappa > 1$ can be described by a power series of photon contributions. When the photon energy $\hbar\omega$ is small compared to the excitation energy ϵ, or the applied field E is very intense, however, electromagnetic waves act rather classically, accelerating charges and distorting potential landscapes within the exposed matter on sub-cycle time scales (Fig. 2.6b). In this strong-field regime $\kappa < 1$, the carrier wave of light can be directly used as an ultrafast bias, which may eventually drive electron tunneling on sub-cycle timescales – precisely the control mechanism desired in lightwave STM.

For this purpose, pulses in the terahertz spectral domain are particularly well-suited

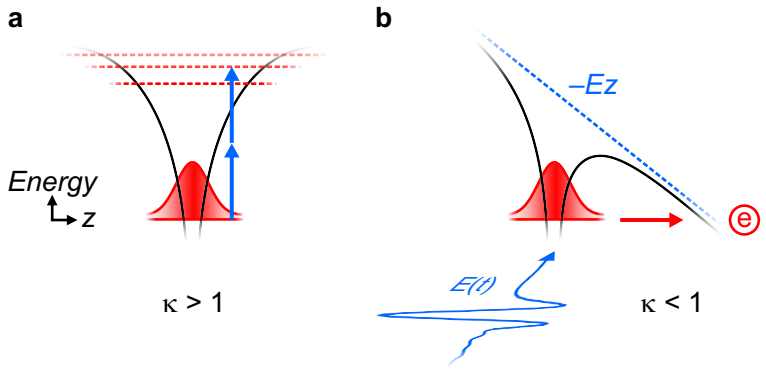

Figure 2.6 | Regimes of light-matter interaction. A schematic one-dimensional potential landscape (black lines) hosts a bound electronic state (red wavepacket). When electromagnetic radiation interacts with the system, two extremal processes can be described. **a**, At a Keldysh parameter $\kappa > 1$, multiphoton excitation (blue arrows) to energetically higher states (red dashed lines) is more likely. **b**, In the opposite strong-field regime $\kappa < 1$, the electric field $E(t)$ (blue waveform) adds a transient slope $-Ez$ (blue dashed line) to the potential landscape, which may enable electron tunneling (red arrow).

for several reasons. Light fields oscillating at terahertz frequencies are fast enough to probe the dynamics of typical low-energy elementary excitations of matter, which feature energies ranging from millielectronvolts to few electronvolts that translate into femtosecond time scales. At the same time, terahertz electric-field waveforms can be accurately tailored and time-resolved with sub-cycle precision. The toolbox of nonlinear optics facilitates generation of terahertz waveforms with a duration shorter even than a single oscillation cycle of the carrier wave. Electro-optic techniques allow us to observe such waveforms directly in the time domain, like in an oscilloscope for light. Making use of dispersive media, the pulses' phase can be tuned such that the resulting waveforms essentially consist of only a single prominent field crest – an ideal ultrashort bias spike.

Figure 2.7 shows such a sub-cycle terahertz waveform. When pulses of this kind are coupled into an STM, their unidirectional field crest may be expected to translate into an ultrafast voltage pulse across the junction. To steer electron tunneling, this transient voltage must be comparable with typical electronic tunnel resonances on the order of $\epsilon \approx 1\,\mathrm{eV}$. For a typical tip-sample tunnel distance of several angstroms, near fields $E \approx 0.1\,\mathrm{V/Å}$ are required. These numbers yield a convincingly low Keldysh

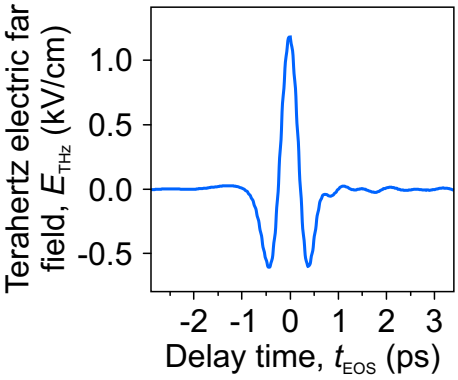

Figure 2.7 | Sub-cycle terahertz waveform. Terahertz electric-field transient generated by optical rectification in lithium niobate, and detected electro-optically. The waveform contains only one single prominent half-cycle in the positive field direction, and after a delay time of just 1 ps, virtually no trailing field oscillations follow. Such a quasi-unidirectional field spike appears ideally suited for ultrafast biasing of a lightwave-controlled STM.

parameter $\kappa \approx 0.02$ at $\omega/2\pi = 1\,\mathrm{THz}$, which is why terahertz pulses are expected to controllably steer purely field-driven tunnel dynamics in lightwave STM.

In addition, suitable terahertz pulses are so low in energy that they avoid thermal tip expansion. With typical pulse energies of 1 pJ, even at high repetition rates towards 1 MHz such a terahertz beam exhibits a power of only 1 μW approximately. As the experiments presented below confirm, these pulses allow lightwave control of electron tunneling without compromising the stability and atomic precision of STM.

Optical source requirements. An optical source for lightwave STM needs to fulfill a number of design requirements. The generated pulses must possess a well-characterized waveform with a tunable carrier-envelope phase (CEP). In this way, the transients can be tailored to steer the microscope in a desired manner. To achieve the highest possible temporal resolution, and ideally obtain single-electron tunnel control with only one field crest, the shortest technically possible waveforms are required, shorter even than one oscillation cycle of the carrier wave. For repetitive experiments with pulse trains, CEP stability across all pulses is mandatory such that all waveforms are identical. In this way, experiments where the same well-defined conditions are required over and again become feasible.

Following the ongoing development of high-power femtosecond lasers, terahertz sources generating high field strengths (>1 kV/cm) at simultaneous large repetition rates (>1 MHz) have become available. In lightwave STM, a high repetition rate of the pulse source directly translates into a large number of tunneled electrons, promising strong tunnel currents to be detected. As a benchmark, state-of-the-art current preamplifiers employed in STM technology achieve a noise level as low as

850 fA at a bandwidth of 1.1 kHz (ref. 84), which allows for millisecond acquisition times. In STM measurements where the signal bandwidth can be further restricted, the tunnel current typically exhibits a noise level around 100 fA, corresponding to a charge flow of approximately half a million electrons per second. An optical source with a repetition rate larger than 500 kHz should therefore yield practical acquisition times. Moreover, designing a source that can also deliver individual pulses as well as pulse trains at select low repetition rates will enable single-shot experiments and access statistical dynamics induced by a single electron tunnel event, as will be demonstrated in chapter 3.

At the same time, the peak field of each pulse needs to be strong enough to address typical tunnel resonances in the STM energetically. As will be elaborated in detail in chapter 4, the tip-substrate geometry acts as an antenna for lightwaves coupled into the gap. Focussing terahertz radiation with a wavelength of $\lambda \approx 300\,\mu$m down to the diffraction limit[85] $d_{\mathrm{lim}} = \frac{\lambda}{2\,\mathrm{NA}}$ (NA, numerical aperture) still yields a spot size large enough to illuminate a macroscopic fraction of tip and substrate. Due to their dielectric properties at terahertz frequencies, the metallic structures plasmonically propagate the waveforms into the atom-sized gap. In this process the fields are localized in an extremely sub-wavelength volume and thereby strongly enhanced. Antenna theory provides a rough estimation of this effect[86]: Terahertz frequencies are enhanced by approximately five orders of magnitude in a gap a few angstroms wide. Consequently, to achieve atomically strong near fields on the order of $E_{\mathrm{NF}} \approx 1\,\mathrm{V/Å}$ across the tunnel junction, waveforms with amplitudes $E_{\mathrm{FF}} \approx E_{\mathrm{NF}}/10^5 \approx 1\,\mathrm{kV/cm}$ need to be available in the far field.

Optical source. Taking all these considerations into account, the terahertz source schematically illustrated in Fig. 2.8 has been designed and implemented. A high-stability ytterbium-based femtosecond laser and amplifier system delivers pulses in the near-infrared (NIR) spectral region, centered at a wavelength of 1030 nm, with a pulse length of approximately 240 fs (full width at half maximum, FWHM, of the intensity). The repetition rate can be tuned from 610 kHz down to single shots at a constant pulse energy of 16 μJ. This laser primarily serves to generate terahertz pulses via nonlinear optics, but also, a small fraction of the pulse energy is split off to produce short gate pulses for electro-optic detection of the terahertz waveforms.

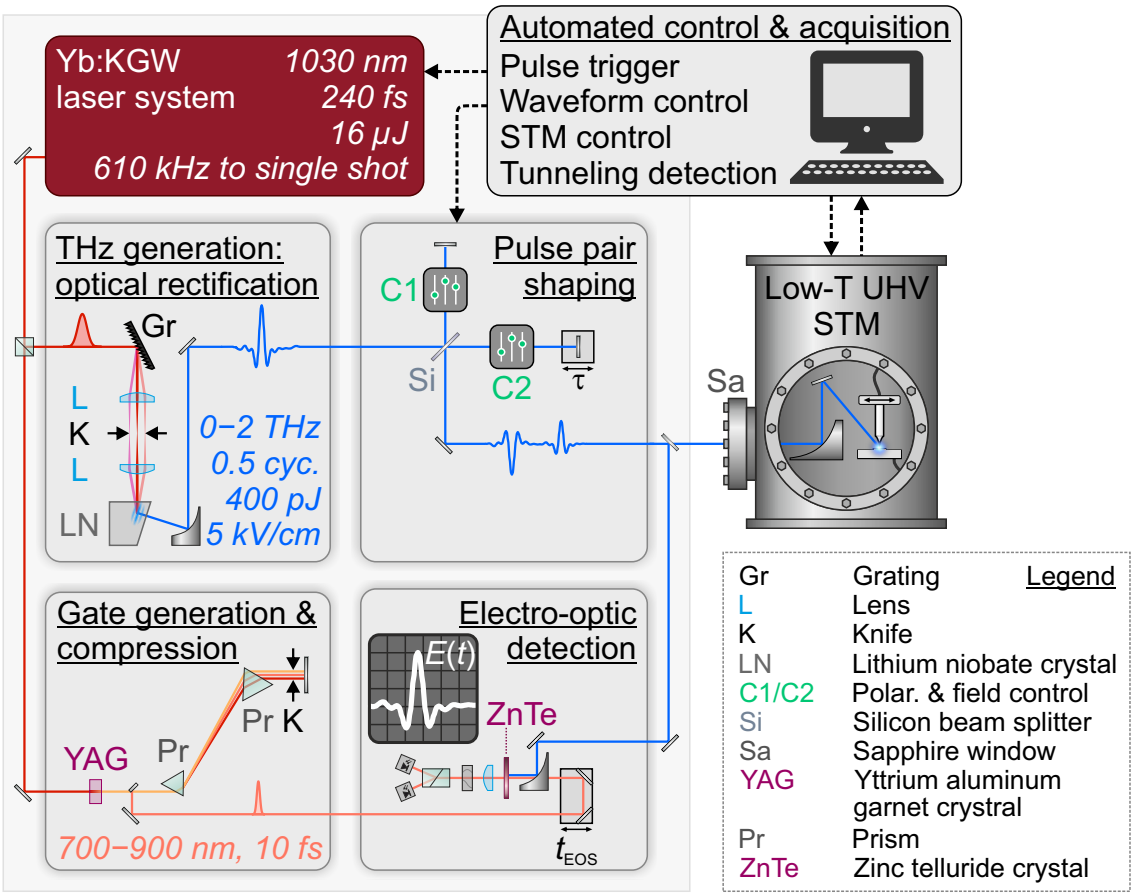

Figure 2.8 | Optical lightwave-STM setup and logics. Sub-cycle lightwaves are generated and custom-tailored in several steps. We derive femtosecond infrared pulses from a commercial high-power laser system (red, top left) and exploit optical rectification in a nonlinear-optical crystal to generate strong and broadband terahertz waveforms (left). Then we split the pulses into pairs that can be mutually delayed and separately shaped (center). The field strength and polarization of the individual waveforms in a pair are individually tailored, before the pulses are coupled into the STM vacuum chamber through a low-dispersion viewport. In situ, the pulses are focussed onto the tunnel junction with optics mounted to the STM scanhead. The same focussing geometry is emulated on the optical table to accurately characterize the waveforms. To this end, even shorter gate pulses are generated in an optical filamentation process (bottom left) and subsequently shaped so they can sample the terahertz waveforms electro-optically, directly in the time domain (bottom). All the pulse generation and shaping, STM operation as well as data acquisition are computer-controlled and united in one logical platform (top right, arrows). In this overview, only key optical components are shown and labeled in a legend (bottom right). The relevant parameters of the pulses are given in the figure.

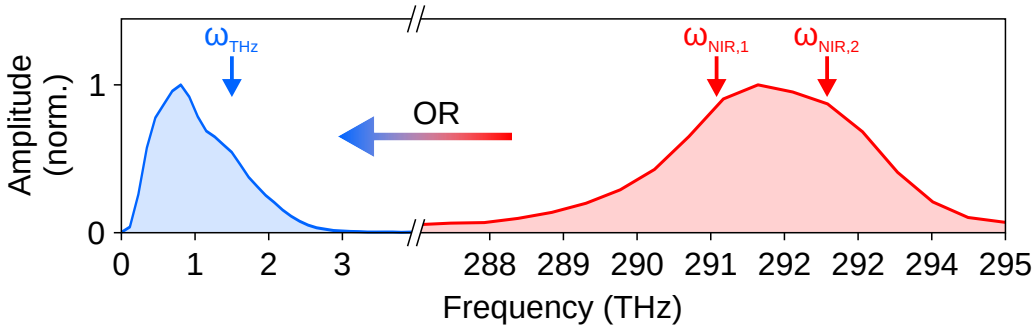

Figure 2.9 | Terahertz generation via optical rectification. The optical source provides near-infrared spectral components ω_{NIR} around 292 THz (red). Optical rectification (OR) in a lithium niobate crystal converts this spectrum into its difference frequencies ω_{THz} in the low-terahertz range (blue).

Terahertz waveform generation. Terahertz pulses are generated by so-called optical rectification in a lithium niobate ($LiNbO_3$) crystal. In a simple picture, this process can be rationalized as follows[87,88]:

The short laser pulses contain a range of spectral components, which is mandatory due to the quantum mechanical energy-time uncertainty. The laser amplifier we employ provides wavelengths, λ_{NIR}, ranging from 1025 nm to 1034 nm (intensity FWHM).

When such a light pulse interacts with a dielectric medium, the electric carrier wave of light $E(t)$ accelerates bound electrons within their local potential energy surfaces. The optical response can often be described by expressing the polarization $P(t)$ as a power series in the field strength $E(t)$. Particularly, the polarization term may contain a second-order contribution

$$P^{(2)}(t) = \varepsilon_0 \chi^{(2)} E^2(t) \tag{2.2}$$

where ε_0 denotes the vacuum permittivity and $\chi^{(2)}$ is called second-order nonlinear susceptibility[a]. This nonlinear response causes the reemitted radiation to contain frequencies different from those of the driving field, as a consequence of the electrons' anharmonic motion pattern.

Optical rectification denotes the case where electrons, accelerated by several fre-

[a] In general, the material-specific susceptibility is a complex-valued, frequency-dependent tensor.

quencies $\omega_{\mathrm{NIR},1}$ and $\omega_{\mathrm{NIR},2}$ at once, reemit radiation at the difference frequency $\omega_{\mathrm{THz}} = \omega_{\mathrm{NIR},2} - \omega_{\mathrm{NIR},1}$. Lithium niobate turns out to be very efficient in difference-frequency conversion from near-infrared to low-terahertz frequencies. Figure 2.9 show the amplitude spectrum of the laser source, together with a terahertz spectrum generated by optical rectification.

Such nonlinear optical phenomena can be used for efficient frequency conversion of coherent light. In this case, the radiation generated at different positions in the medium must interfere constructively in a certain emission direction. To achieve this so-called phase-matching condition[88] in lithium niobate, a geometry based on pump pulses with tilted pulse fronts has proven most efficient[87,89].

Figure 2.10 illustrates the non-collinear phase matching geometry. In lithium niobate, the group velocity of the optical pump pulses $v_{\mathrm{gr}}^{\mathrm{NIR}} = 0.45c$ is larger than the phase velocity of the generated terahertz radiation $v_{\mathrm{ph}}^{\mathrm{THz}} = 0.20c$ (c, vacuum speed of light). Hence a single ray of pump light would emit terahertz radiation under an angle of $\mathrm{acos}(v_{\mathrm{ph}}^{\mathrm{THz}}/v_{\mathrm{gr}}^{\mathrm{NIR}}) = 63\,\mathrm{deg}$ in a way that resembles Cherenkov radiation (Fig. 2.10a). When a physical beam of pump light with a finite lateral extent is propagated through the crystal, tilted pulse fronts can be applied to ensure constructive interference of all terahertz radiation generated at different crystal positions (Fig. 2.10b).

In the present optical setup, the pulse fronts of the pump pulses are tilted by diffracting the beam off a blazed grating (Fig. 2.10c). Since the different spectral components of the pump pulses are diffracted by different angles, a telescope setup is employed for imaging of the tilted pulse fronts into the nonlinear crystal. The generated terahertz radiation is emitted in a divergent way under an angle of 63 deg with respect to the incident pump beam. After collimation with an off-axis parabolic mirror, the pulses enter a part of the setup where they are conditioned for flexible lightwave-STM experiments.

The pulses contain frequencies ranging from 0.1 THz to 2 THz (Fig. 2.9) and describe a cosine-like sub-cycle waveform (Fig. 2.7) with an envelope as short as 0.5 cycles of the center frequency (FWHM of the intensity envelope). Directly after generation, the pulse energy amounts to approximately 400 pJ, allowing for peak field strengths of approximately 5 kV/cm in a diffraction-limited far-field focus generated with a numerical aperture of 0.1.

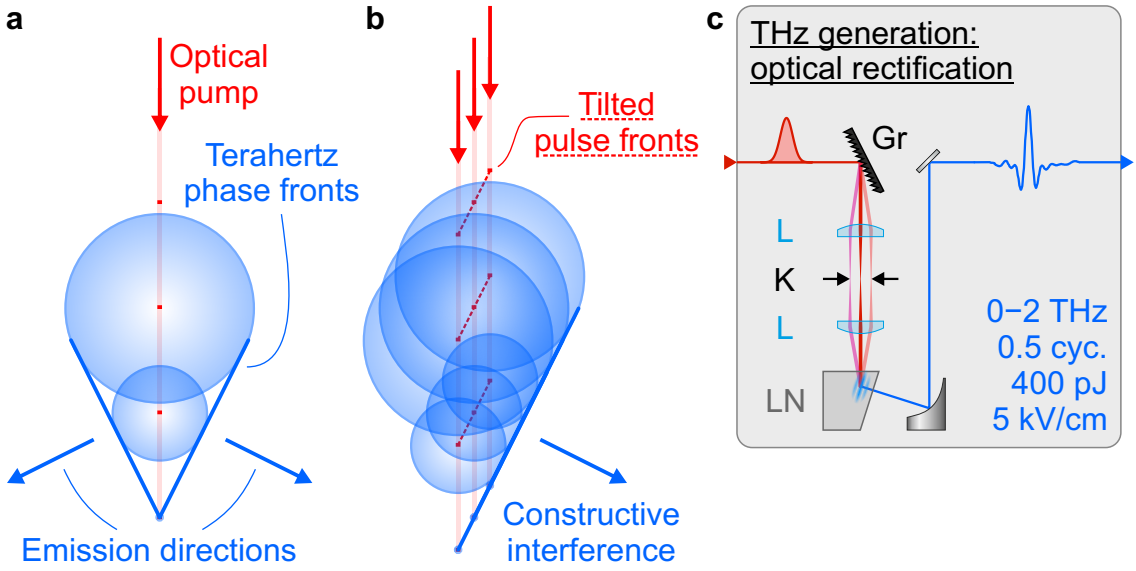

Figure 2.10 | Non-collinear phase matching. a, When an optical pump pulse propagates during a lithium niobate crystal along a single optical ray (light red), terahertz radiation is generated at different positions (e.g. red dots). Due to the different velocities of propagation, interference of the terahertz Huygens elementary waves (blue circles) causes terahertz emission under an angle, similar to Cherenkov radiation. **b**, When a pump beam with a finite lateral profile exhibits suitably tilted pulse fronts, the terahertz Huygens elementary waves generated at all positions of the crystal interfere constructively in a certain emission direction. **c**, In the present setup, this pulse front tilt is achieved by diffraction off a blazed grating (Gr). A tailored telescope geometry (L, lenses) images the different spectral components that are dispersed by the grating into the lithium niobate crystal (LN). Knife edges (K) placed in the Fourier plane of the telescope precondition the pump spectrum.

Pulse pair shaping. Subsequently, the pulses are split into pairs separated by an adjustable delay time, τ, via a Michelson interferometer (Fig. 2.11). Such pairs can be employed to time-resolve ultrafast dynamics in a stroboscopic fashion, by so-called pump-probe experiments. In such experiments, an initial pump pulse excites dynamics, followed by a delayed probe pulse that senses a snapshot of the response. Varying τ allows the observer to trace the temporal evolution of the object under study, step by step, directly in the time domain. As shown later, we will use different configurations of these pulse pairs where the individual amplitude and field direction of each pulse needs to be chosen freely. For this purpose, we tailor the pulses separately through a number of externally controllable components, summarized by the

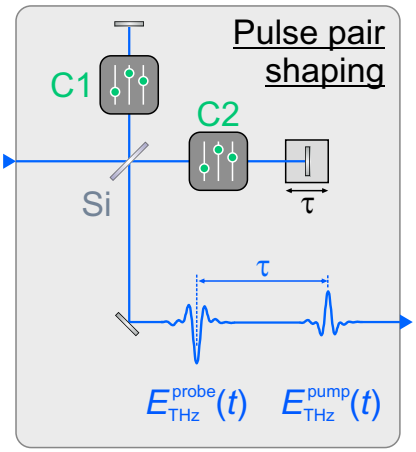

Figure 2.11 | Tailoring of pulse pairs. We employ a Michelson interferometer to split the generated terahertz pulses into pairs (Si, silicon beam splitter). Motor-controlled positioning of one end mirror allows us to tune the delay time τ. The polarization and amplitude of both pulses in a pair is separately controlled (C1, C2) via optomechanical elements. Hence we obtain tailored sequences of pump and probe electric-field transients, $E_{\mathrm{THz}}^{\mathrm{pump}}(t)$ and $E_{\mathrm{THz}}^{\mathrm{probe}}(t)$.

placeholders "C1" and "C2" in Fig. 2.11. In detail, to adjust the field strengths at will, pairs of crossed polarizers are used. The field directions are chosen in a geometry with flexible beam paths, making use of the phase shift of π that a waveform acquires upon reflection off one mirror or transmission through a focus.

Electro-optic waveform detection. We monitor the terahertz waveforms via electro-optic detection[90–92]. To this end, a broadband white light continuum is generated in an yttrium aluminum garnet (YAG, $Y_3Al_5O_{12}$) crystal (Fig. 2.12). In this process, a self-focusing filament produces a coherent spectrum that contains wavelengths ranging from approximately 600 nm up to the laser fundamental at 1030 nm. A prism compressor serves to compensate the pulses' chirp and filter their spectral components (Fig. 2.12a). In this way, we condition gate pulses that cover wavelengths from 700 nm to 900 nm and are as short as 10 fs (Fig. 2.12b).

These pulses are much shorter than the oscillatory period of the terahertz transients, hence they can be used to sample our waveforms electro-optically. To do so, terahertz and gate pulses are spatially overlapped and focused into a zinc telluride (ZnTe) crystal. Due to the Pockels effect, the instantaneous terahertz field strength is imprinted on the polarization state of the gate pulses, which we can read out with polarization optics and photodiodes. We vary the delay time, t_{EOS}, between terahertz and gate pulse, and detect the gate polarization for every sub-cycle temporal overlap. This procedure directly yields the terahertz waveform, $E(t_{\mathrm{EOS}})$, like the one shown above in Fig. 2.7.

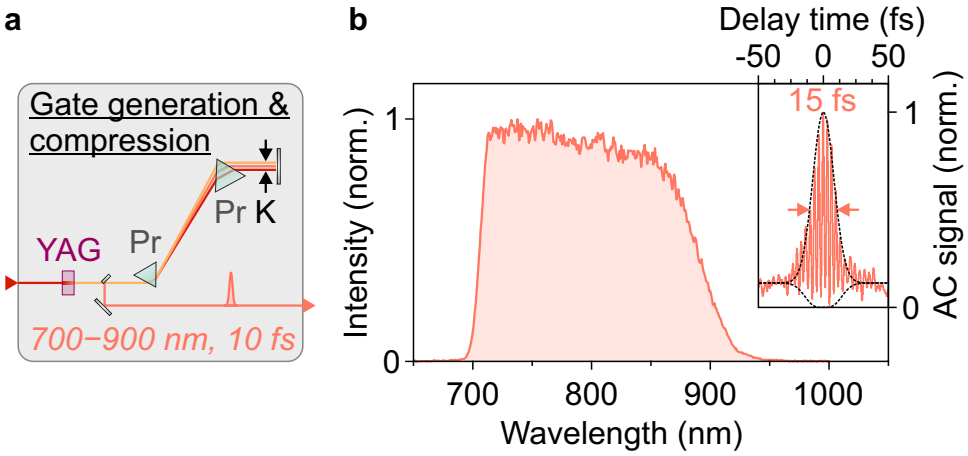

Figure 2.12 | Gate pulse generation and compression. a, A broadband white-light continuum is generated in a YAG crystal and conditioned through a prism compressor (Pr, prisms). **b** After spectral filtering (K, knife edge in Fourier plane) and compression, the pulses feature a flat spectrum ranging from 700 nm to 900 nm. An interferometric autocorrelation of the pulses (inset) exhibits a width of 15 fs (dashed lines, simulated envelope), indicating a pulse length of around 10 fs.

Setup periphery. All optics and the laser source are mounted onto a portable high-stability optical table in a geometry as compact as possible. The whole optical setup is housed and purged with nitrogen gas such that ambient absorption does not corrupt the generated sub-cycle terahertz waveforms. Several beam branches are guided across parallel planes on different heights, and optomechanics including motors and air-pressure control serve to steer and condition the beams remotely. The optics are placed on the same frame as the entire STM system. Thereby all optical and terahertz beams can be coupled to the STM in a precise and stable manner, with lowest possible mechanical noise. All beams enter the STM chamber in a collimated geometry through a sapphire window, which exhibits almost now dispersion at low terahertz frequencies.

STM design. The microscope operates under ultra-high vacuum conditions. The scanhead is mounted to a liquid-helium bath cryostat where it is kept at low temperatures down to 7 K at a pressure of $\sim 10^{-10}$ mbar. This clean environment allows us to keep atomically defined surfaces uncontaminated for weeks. Moreover, cooling a sample down to cryogenic temperature ensures a low mobility of surface adsorbates.

In this way individual atoms and molecules can be localized at atomic adsorption sites, and remain stable and in place to be examined for extended periods of time. Also, thermal drift is minimized in a low-temperature scanning probe microscope, such that the tip can be kept at a certain position relative to the sample, defined with picometer precision, for as long as half an hour approximately. In this way, we can conduct experiments with atom-scale spatial stability, on samples where every atom and molecule is well-defined.

In addition to the STM electronics and tools, optical elements for focussing and alignment of the terahertz beam are mounted on the scanhead. A parabolic mirror (effective focal length, $f_{\mathrm{eff}} = 75\,\mathrm{mm}$) conditions a far field focus with a diameter of $d = 5.4\,\mathrm{mm}$ ($1/e$-decrease of the electric field). The convergent beam is directed onto the tip apex via a flat movable mirror mounted onto a piezo motor that we control externally. In this way, the terahertz radiation is aligned in-situ and directly coupled to the tunnel junction.

Control logics. All of the setup is computer-controlled such that fully automated measurements can be performed. The pulse generation is steered via software control of the laser. Waveforms are tailored by motor-driven optomechanics. The STM electronics are controlled and read out through a real-time processing unit, which communicates with a desktop computer. Hence optics and STM are operated and signals are read out within one central computing unit, allowing complex experimental logics to be carried out. In particular, measurement algorithms can be implemented where the protocol adapts autonomously, depending on the acquired data and experimental circumstances. Ideal measurement parameters can be chosen on the fly, which allows us to record complete and self-consistent datasets. In particular, we implement a feedback control that compensates thermal drift of the tip position, such that we can acquire data at one well-defined position of the sample for arbitrarily long periods of time, in principle. These aspects have proven vital in particular for the high-precision statistical experiments presented in chapter 3.

In the remainder of this chapter, terahertz pulses will be used to drive ultrafast electron tunneling in STM. Individual molecules adsorbed on atomically flat surfaces serve as an ideal testbed for lightwave tunnel control, as they provide sharp orbital

resonances with a unique spatial structure at atomic scales. When the terahertz waveforms are tuned to access such a resonance, they can controllably inject or eject a single electron into or out of a select orbital of one molecule. This process allows us to record the first femtosecond snapshot image of an individual molecule. Moreover, a detailed analysis of the spatial and temporal properties of the tunnel process itself serves as a benchmark: I will show that via lightwave control, single-electron tunneling in an STM can be steered with combined 0.6 Å spatial and ~100 fs temporal accuracy. Most surprisingly, we find that the injection of a single charge into a molecule does already trigger structural picosecond dynamics. Single-molecule vibrations are directly observed in the time domain, providing a first impression of what the nanoworld in motion looks like, observed through a femtosecond atom-scale camera.

The results discussed in the remainder of this chapter follow the presentation in reference 20. Parts of these experiments have already been depicted in reference 93, but are repeated here for completeness.

2.2 Femtosecond snapshots of individual molecules' orbitals

The fascination of studying single molecules in STM stems from the intimate connection with chemistry, where the way a molecule "works" derives from its coupled electronic and structural degrees of freedom[1]. In particular, the multifaceted orbital structures of organic molecules – the origin of biological function and a versatile platform for optoelectronics – prompts curiosity across scientific disciplines.

At the heart of molecular reactions and function, however, lie ultrafast dynamics, which cannot be resolved by steady-state STM. In this section, I will introduce lightwave-steered orbital tunneling of a single electron. This novel process allows us to capture the first femtosecond snapshot of an orbital of one single molecule. Moreover, it will later serve as our key tool to directly track a single-molecule femtosecond vibration, for the first time.

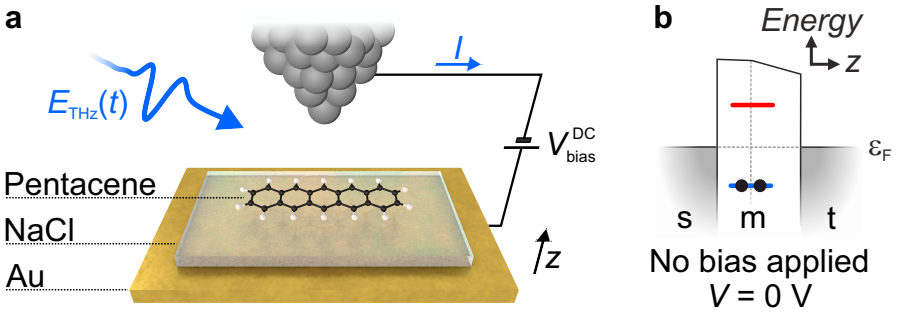

Figure 2.13 | Single-molecule STM tunneling barrier. a, Schematic illustration of a single pentacene molecule (ball-and-stick model) studied in lightwave STM. The molecule is adsorbed on a decoupling layer of sodium chloride (NaCl) on a gold (Au) substrate. When a constant external bias voltage, $V_{\mathrm{bias}}^{\mathrm{DC}}$, is applied between substrate and tip (front-most atoms shown), a continuous tunneling current, I, can be driven. Conversely, we intend to steer electron tunneling with ultrafast temporal definition via terahertz electric-field waveforms (blue), $E_{\mathrm{THz}}(t)$. **b**, A one-dimensional scheme of the energetic landscape across the tunnel junction visualizes that the vacuum gap between tip (t) and substrate (s) constitutes a potential-energy barrier. When no bias voltage is applied, electronic states in both tip and substrate are occupied (gray shaded areas) up to the Fermi energy, ϵ_{F}. Orbital resonances (red and blue line) of the molecule (m) are localized within the tunneling barrier.

Single-molecule tunneling microscopy. To study single molecules in STM, we adsorb them on a substrate in such a way that they are electronically decoupled from the surroundings. When working on a metallic substrate, this decoupling is achieved by first growing one or a few atomic layers of an insulating material on the surface[61]. When we then deposit molecules on top, their orbitals do not strongly hybridize with the underlying metal. Hence the molecules' electronic structure remains similar to that of free species in vacuum.

In the present experiment, we grew monolayer islands of sodium chloride (NaCl) on a (110) surface of a gold substrate and adsorbed pentacene molecules on top (Fig. 2.13a). This sample was then inserted into the STM, the electronic circuitry was applied and the tip was brought in tunnel contact.

To see how orbital resonances of a molecule can be probed via electron tunneling, it is instructive to visualize the energy landscape across the junction. Figure 2.13b illustrates the relevant electronic states of tip (t), substrate (s) and molecule (m) in

a one-dimensional picture. Following a line in z-direction, i. e. parallel to the tip axis, one finds a continuum of occupied states (gray) below and unoccupied states (blank) above the Fermi energy, ϵ_F, in the metallic tip and substrate. At a temperature of 7 K, the edge of the Fermi distribution is as sharp as 1 meV. The molecular orbitals are spatially located within the barrier between tip and substrate. This tunnel barrier consists of the NaCl layer below the molecule and a vacuum gap above. Its energetic height is derived from the work functions of tip and sample. In a real experiment, however, the barrier shape is slightly different due to the image charge effect, among others[94].

When no external bias voltage is applied to the junction, the Fermi energies of tip and substrate align (Fig. 2.13b). In this equilibrium scenario, orbitals below the Fermi energy will be occupied and those above the Fermi energy end up unoccupied. The highest occupied molecular orbital (HOMO) is drawn as a blue line and the lowest unoccupied molecular orbital (LUMO) as a red one. Two electrons (black dots) with opposite spin occupy the HOMO.

Non-resonant cotunneling. If the junction is electrically biased, the energy level alignment can be modified: An applied voltage, V, manifests as a potential-energy drop eV between tip and substrate. The potential barrier is tilted and the Fermi edges of tip and substrate differ by eV. Figure 2.14a shows the potential landscape when a negative bias voltage smaller than any orbital resonance, V_{orbital}, is applied to the substrate. Then an energetic window opens up where one finds occupied states in the substrate and unoccupied tip states that share a mutual energy. In this so-called "bias voltage window", electrons can tunnel directly from the substrate into the tip, a process also denoted "cotunneling".

Resonant sequential orbital tunneling. By contrast, when a particular voltage is applied, a different tunnel phenomenon sets in that involves charging of the molecule[61]. In the presented picture where external biasing tilts the energy landscape of the tunnel barrier, the molecular orbitals remain mostly aligned with respect to the substrate states[94]. The reason for this is that, due to the geometry and dielectric properties of the insulating salt layer, only approximately 1/10 of the applied voltage drops between molecule and substrate.

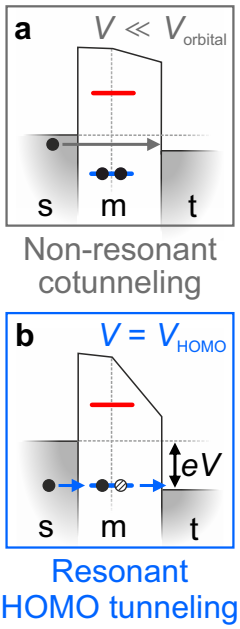

Figure 2.14 | Non-resonant versus orbital-resonant tunneling through a single molecule. One-dimensional energy landscape of the tunnel junction as described in Fig. 2.13. **a**, When a small tip-substrate voltage V (defined in **b**) is applied, the potential landscape is slightly tilted. Then, electrons (black dots) can only tunnel directly between tip and substrate (gray arrow). **b**, Certain voltages, though, induce an energy level alignment such that a molecular orbital resonance enters the energetic window where tunneling is allowed. In this case, electrons can additionally tunnel via two-step sequential tunneling. After an electron tunnels from the highest occupied molecular orbital into the tip (right blue arrow), the remaining hole (striped circle) is filled up by an electron tunneling from the substrate (left blue arrow). We aim to steer such level alignment transiently, at terahertz clock rates, by using lightwaves to bias the junction.

When the applied bias is increased such that an orbital resonance enters the bias voltage window, two-step orbital tunneling sets in (Fig. 2.14b). An electron can tunnel from the HOMO into the tip, leaving a hole in the orbital occupation behind (circle with striped texture). This void can be refilled by electron tunneling from the substrate, yielding a contribution to the overall current through the STM circuitry that we detect externally. Whenever allowed by the energy level alignment, sequential tunneling quantitatively dominates over cotunneling as a result of the smaller barrier widths.

dI/dV conductance spectroscopy. This remarkable quality of sequential tunneling being energy-selective via the applied voltage can be visualized in a scanning tunneling spectroscopy experiment. We position the tip in tunneling distance on top of a molecule, sweep the applied voltage V and record the resulting tunnel current I. In this way, the bias voltage window is gradually enlarged, allowing more and more tip, substrate and – eventually – molecular states to be involved in tunnel processes. The differential conductance, dI/dV, then indicates, in a simplified view, how many new tunneling channels contribute to an additional current increment dI when the bias is increased by dV.

In the Bardeen model[94], the tunneling current

$$I(V) \propto \int_0^{eV} \rho_\mathrm{s}(\epsilon_\mathrm{F} - eV + \epsilon)\rho_\mathrm{t}(\epsilon_\mathrm{F} + \epsilon)|M|^2 \mathrm{d}\epsilon \tag{2.3}$$

is determined by the electronic densities of states of the tip, ρ_t, and the sample, ρ_s, within the bias voltage window $[0, eV]$. In this shorthand notation, the matrix elements $|M|$ account for the spatial overlap of each pair of tip and sample states. Due to their proximity to the tip, the molecular orbitals exhibit significantly larger matrix elements $|M|$ than all other substrate states. Hence, the current $I(V)$ is dominated by sequential tunneling through molecular orbitals. Equation 2.3 shows that when ρ_t and $|M|$ are approximately flat, the differential conductance $\mathrm{d}I/\mathrm{d}V$ directly reveals the molecular density of states at a given tip coordinate.

Figure 2.15a shows the result of a tunnel spectroscopy experiment where the tip was positioned above a pentacene molecule. For voltages between $-1.5\,\mathrm{V}$ and $+1.5\,\mathrm{V}$, the differential conductance is comparatively small and flat. Only weak cotunneling channels are probed in this bias window. At voltages of $-1.9\,\mathrm{V}$ and $+2.1\,\mathrm{V}$, however, strong peaks show up in $\mathrm{d}I/\mathrm{d}V$. These resonances correspond to the HOMO and LUMO transport levels (Fig. 2.15b). They indicate a large number of sequential tunneling events once energetically allowed by the external bias. The resonance linewidths of 0.6 eV stem from phonon broadening due to coupling of sequential tunneling channels with a phonon of the NaCl layer.

Lightwave-driven orbital tunneling. The central objective of this chapter is to steer the dynamic analogue of sequential tunneling, where a lightwave replaces the steady-state bias (waveform in Fig. 2.13). Light-matter interaction with intense terahertz fields often drives dynamics that include different competing quantum effects[33,70,73]. The results presented below, however, will justify a semi-classical picture in which the terahertz waveform acts as an ultrafast bias voltage, inducing a transient modification to the level alignment of the system. Even though this picture cannot be assumed a priori, to facilitate the discussion, it will be introduced right away and justified later on through the experimental results.

Our idea is to tune the field strength of the terahertz waveforms such that only the field crest of the most intense half-cycle accesses an orbital tunnel resonance

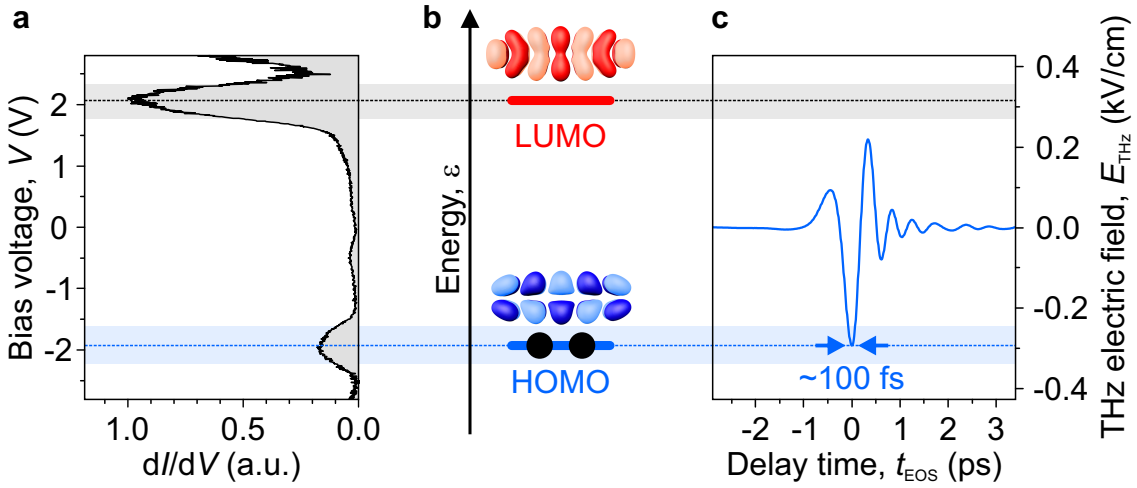

Figure 2.15 | Lightwave-driven femtosecond orbital tunneling. **a**, Steady-state tunnel spectroscopy measurement of a single pentacene molecule. Orbital resonances show up as peaks in the differential conductance, $\mathrm{d}I/\mathrm{d}V$, which indicate additional sequential tunneling channels on top of the omnipresent, comparatively weak cotunneling background. **b**, The resonances adjacent to $V = 0\,\mathrm{V}$ correspond to the highest occupied and lowest unoccupied molecular orbital (HOMO and LUMO). The voltage parameter directly accesses the energy scale of molecular states. **c**, When terahertz lightwaves are used to transiently bias the junction, their electric-field waveform (vertical axis, far field) translates into a voltage pulse across the junction (dashed line connecting the panels). If the terahertz amplitude is tuned such that only the peak of the waveform accesses an orbital resonance, the duration of the field crest may confine electron tunneling to a time window of ~100 fs.

(Fig. 2.15c). In other words, only at the instant where this field crest acts as an instantaneous resonant bias across the tunnel junction, sequential tunneling is allowed via transient level alignment. We thereby controllably define an extremely sub-cycle time window during which an electron can be extracted from the HOMO, for example. The asymmetry of the terahertz waveform should allow us to selectively drive tunneling out of the HOMO without accessing the LUMO. In this scenario, we expect the lightwaves to prompt unipolar current bursts with a duration defined by the width of the waveform crest.

Spectroscopic onset of lightwave-driven tunneling. Our picture is put to the test in a first experiment where we position the tip above a pentacene molecule, fix the

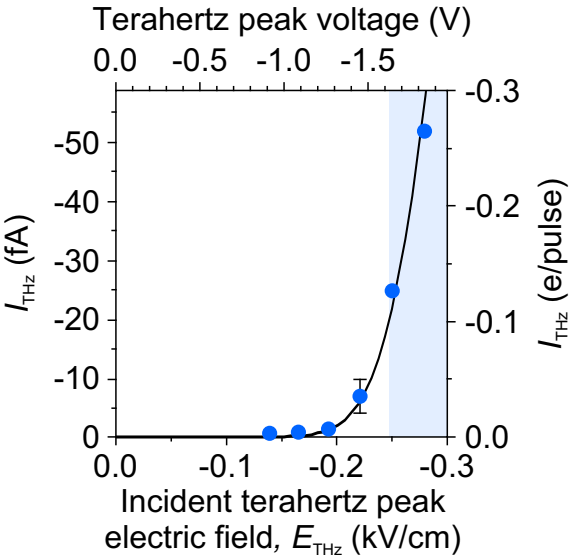

Figure 2.16 | Onset of lightwave-driven pentacene HOMO tunneling. Lightwave-driven orbital tunneling (data points) sets in once the incident terahertz peak field (bottom axis) exceeds a certain threshold. Currents of tens of femtoamperes (left axis) describe an average tunnel rate around 0.1 electrons per pulse (right axis). A simple model (black line) calibrates the terahertz-induced peak voltage across the junction in units of volts (top axis). Blue shaded area, HOMO resonance width.

tip at a constant height and turn off the steady-state bias voltage. Now the tip hovers over the molecule and we measure zero tunnel current. Then we couple terahertz pulses to the tunnel junction. If we now detect any average current with the STM circuitry, it must stem from lightwave-steered electron tunneling. Figure 2.16 shows the result. When we increase the field strength, we indeed observe a strong onset of lightwave-driven tunneling at an external peak field of approximately 0.3 kV/cm.

Two quantitative details of these data strike the eye: First, the number of electrons tunneled per pulse on average is below one. Second, we discover that lightwave-steered tunneling already sets in at seemingly moderate field strengths. In fact, the physical relation between the field strength coupled into the microscope and the resulting voltage transiently applied across the junction lies at the heart of lightwave control in STM. As indicated above, owing to the large field-enhancement of the tip ($\approx 10^5$), moderate external fields ($\approx 10^5$ V/m) can already induce atomic field strengths ($\approx 10^{10}$ V/m = 1 V/Å) across the tunnel junction. The data in Fig. 2.16 supports this approximate picture. Chapter 4 will elaborate on the physical background, and present a more detailed analysis of the relation between the incident far field and the near field that it induces.

For now, we will analyze the lightwave-driven current in more detail. In particular, we want to confirm whether the presented scheme indeed allows us to control femtosecond tunneling out of an individual orbital. The absolute tunnel currents

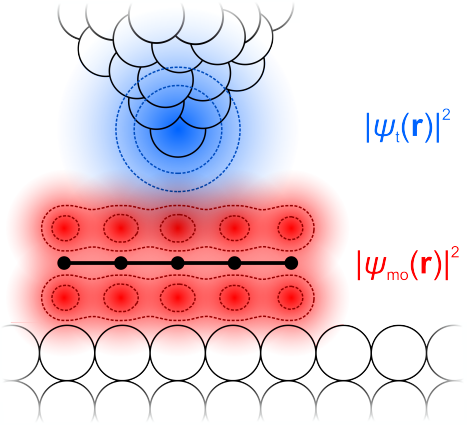

Figure 2.17 | Orbital overlap. Schematic illustration of the wavefunctions that govern tunneling in a single-molecule STM junction. The tip and substrate atoms are drawn as white spheres and the molecular frame is shown as a ball-and-stick model in side view. The density of a molecular orbital, $|\psi_{mo}(\mathbf{r})|^2$, is drawn in red, where red dashed lines indicate several isosurfaces. Density and isosurfaces of a spherical wavefunction located at the tip apex, $|\psi_t(\mathbf{r})|^2$, are shown in blue, respectively. The overlap region of both orbitals that determines the tunnel integral is localized in space.

shown in Fig. 2.16 give a first indication. Remarkably, only tunnel currents below one electron per pulse are observed, which is reasonable if the lightwaves trigger sequential tunneling as intended: After extraction of one electron out of a molecular orbital, the energy landscape should change due to Coulomb interaction, which would prevent subsequent tunneling of a second electron.

Spatial distribution of the tunnel current. The ultimate test of whether this measured current is really due to lightwave-driven orbital tunneling is the spatial distribution of the current. As known from steady-state STM, sequential tunneling can be exploited to record real-space images of the quantum mechanical wavefunctions of individual molecular orbitals[61]. The reason for this is that a tunnel event between an orbital and the tip can only occur when the tip is in tunnel distance, i. e. the wavefunctions of tip, $\psi_t(\mathbf{r})$, and molecular orbital, $\psi_{mo}(\mathbf{r})$, spatially overlap significantly (Fig. 2.17).

Throughout this thesis, real space is described in a cartesian coordinate system $\mathbf{r} = (x, y, z)$ where the substrate defines the (x, y)-plane (lateral direction). The tip axis points in z-direction (vertical) perpendicular to this plane.

When the tip is moved laterally across a molecule, the spatial overlap of the wavefunctions will vary within Å-scale distances. This variation directly derives from the spatial shape of the orbitals, and is encoded in the tunneling probability. The

commonly used Bardeen model[94] describes that the tunnel current I at tip position $\mathbf{r}_0$ is proportional to the overlap integral squared

$$I(\mathbf{r}_0) \propto |M|^2 = \left| \int \mathrm{d}\mathbf{r}\, \psi_\mathrm{t}(\mathbf{r}-\mathbf{r}_0)\psi_\mathrm{mo}(\mathbf{r}) \right|^2 \approx |\psi_\mathrm{mo}(\mathbf{r}_0)|^2 . \tag{2.4}$$

When the tip wavefunction is very sharp, ideally a point in space, or approximately a spherical s-like wave as discussed in the Tersoff-Hamann theory[94], this integral directly maps the molecular orbital density $|\psi_\mathrm{mo}|^2$. In other words, the tunnel current follows the matrix element between tip and orbital states, and this matrix element approximates the electron density of the molecular orbital. Hence we can directly sense molecular orbitals in real space by scanning the tip across the molecule while recording the tunnel rate as a function of lateral position.

Figure 2.18a shows a steady-state STM image of a pentacene molecule recorded with a bias voltage close to the HOMO resonance, $V_\mathrm{bias} = -1.7\,\mathrm{V}$. Ten lobes of electron density are clearly visible, structured by one nodal plane along the long axis of the molecule. A comparison with simulated electron distributions of HOMO and LUMO (Fig. 2.15b) supports that this tunnel process indeed selectively images the HOMO density.

This orbital image is in fact a topographic map. It has been acquired in a constant-current measurement procedure. To be able to clearly interpret these and future STM images, I will now briefly introduce two different technical measurement protocols in STM, namely constant-current and constant-height data acquisition.

Constant-height and constant-current measurements. Imaging in STM is often performed with the tip scanned across a certain (x, y)-plane at a fixed tip height $z = z_0$. In such constant-height measurements, one can measure a certain property, $f(x, y, z_0)$, like the tunnel current, $I(x, y, z_0)$, or spectroscopic data, across pre-defined coordinates. In other circumstances, however, it can be more practical to vary the tip coordinates dynamically during imaging. For example, it may be useful to scan across a lateral window of (x, y) coordinates while keeping a different aspect than the tip height constant. To this end, the STM electronics are equipped with a real-time processor that can implement feedback loops. During acquisition of the steady-state map of the HOMO density (Fig. 2.18a), for instance, the tunnel current

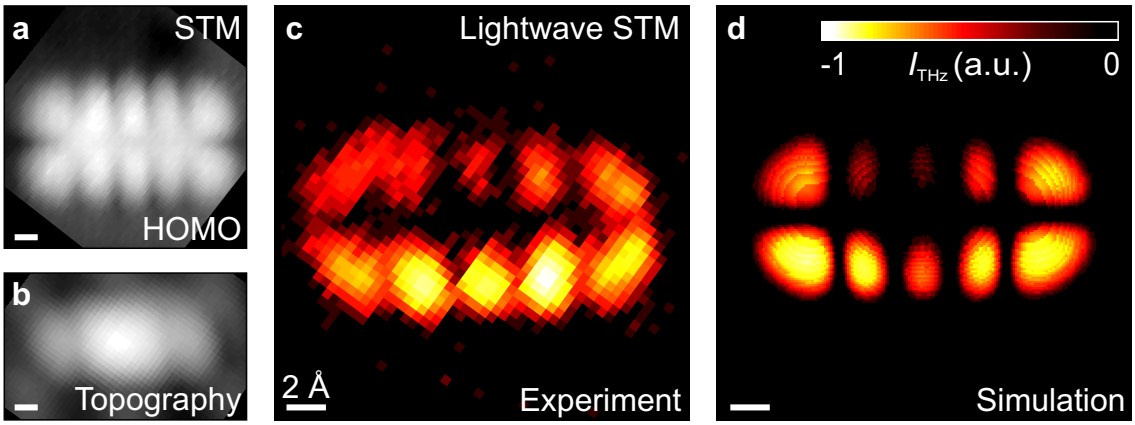

Figure 2.18 | First femtosecond snapshot of a molecular orbital of one single pentacene molecule. a, Steady-state, constant-current STM image of the HOMO density, recorded at $V_{DC} = -1.7\,V$ and $I = 0.83\,pA$. Linear grayscale range of 2.3 Å. The ten tip-sided lobes of the wavefunction are structured in a clearly visible two-by-five pattern. **b**, Non-resonant topographic imaging of an identical molecule at $V_{DC} = 6\,mV$ and $I = 2.2\,pA$. The Au(110) missing-row reconstruction beneath the NaCl film gives rise to an overall stripe pattern that affects the low-voltage appearance of pentacene, which is otherwise featureless. Linear grayscale range of 2.0 Å. **c**, Lightwave STM image recorded simultaneously with **b**, where the terahertz peak voltage was set as $-2.05\,V$ to access the HOMO resonance. While the applied DC voltage generated a non-resonant cotunneling current from the tip to the substrate, terahertz pulses simultaneously steered electron tunneling in the other direction, ejecting electrons out of the HOMO into the tip. In contrast to **b**, the spatial distribution of the lightwave-driven current shows sharp sub-molecular features. The two-by-five shape of the orbital density can be clearly seen, confirming that the lightwaves drive sequential HOMO tunneling and thereby resolve this first femtosecond orbital snapshot. The asymmetry of the snapshot image stems from the topography that the tip followed (**b**), which is confirmed by a simulation based on Tersoff-Hamann theory (**d**). All scale bars gauge a length of 2 Å. In all panels, spots where no data has been acquired are drawn in black.

was kept constant across the entire image. In this constant-current measurement, the tip was scanned across the molecule in the (x, y)-direction while the tip height z was constantly adjusted to maintain a tunnel current of $I = I_0 = -0.83\,\mathrm{pA}$. As a result, we obtain a topographic map, $z(x, y, I_0)$, that can be interpreted as an isosurface of the orbital density[94].

When we turn the bias voltage down such that no orbital resonance can be accessed, only a non-resonant cotunneling current remains. Then we acquire a very different image (Fig. 2.18b). At $V_{\mathrm{bias}} = +6\,\mathrm{mV}$ the topography of the molecule does not resemble the HOMO or LUMO density anymore. Apart from a stripe pattern induced by the underlying Au(110) missing-row reconstruction, the molecule appears featureless. This typical in-gap topography of a molecule can be interpreted as a local aggregation of charges. They act like a dielectric that locally modifies the tunnel barrier for direct cotunneling between tip and substrate.

Detection of lightwave-driven tunneling. In the following, we aim to compare the behavior of steady-state and ultrafast tunneling in a single measurement. To this end, we implement a differential detection strategy that allows us to track lightwave-induced tunneling, separate from any background like steady-state tunneling. We periodically turn the terahertz pulse train on and off via a mechanical chopper that blocks and unblocks the terahertz beam at a frequency ω_{chop}. If the terahertz pulses steer any electron tunneling events, these electrons will add up to an additional component to the tunnel current, periodically modulated at ω_{chop}. When the chopping frequency is lower than the bandwidth of the STM electronics, this component can be detected through the STM current amplifier. We demodulate the tunnel current at ω_{chop} to isolate the lightwave-driven component from the entire tunnel current.

First femtosecond orbital snapshot of a single molecule. In fact, this procedure was carried out when measuring the in-gap topography of the molecule shown in Fig. 2.18b. While the steady-state measurement was performed, terahertz pulses tuned to the HOMO resonance were coupled into the STM simultaneously. The lightwave-induced tunnel current was detected separately. A spatial map of the acquired lightwave-induced tunnel rate is shown in Fig. 2.18c.

The lightwave STM image (Fig. 2.18c) differs dramatically from the in-gap topog-

raphy (Fig. 2.18b). Ten lobes are clearly visible in the spatial distribution of the lightwave-driven current, strikingly similar to the HOMO density. Contrast and spatial definition of the lobes are even sharper than in the steady-state map (Fig. 2.18a). This unique spatial pattern proves that the terahertz waveforms indeed drove sequential HOMO tunneling.

As will be detailed below, every single tunnel event contributing to this map was confined to a femtosecond time window by the field crest of a terahertz waveform. For CEP-stable terahertz pulses, this time window is locked to a fixed point within the pulse envelope, identical at every pixel. In this way, we recorded a snapshot image of the orbital in a stroboscopic way, pixel by pixel.

This lightwave STM map presents the first *femtosecond snapshot* of a select orbital of one molecule, directly recorded in real space. Here the molecule has been captured in equilibrium. Experiments presented later, though, will capture molecules that undergo ultrafast motion.

Some details of the snapshot appear to deviate from the HOMO density, for example the prominent dark region in the center of the map. The reason for this is the particular topography that the tip followed during the scan (Fig. 2.18b). In this measurement, the tip height was increased in the center of the molecule, which reduced the orbital tunneling rate and caused the central dark region of the snapshot. This can be seen in a simulation of the lightwave-driven tunnel current that explicitly takes the tip topography into account. We evaluate the tunnel integral in equation (2.4) for tip positions $\mathbf{r}_0$ along the actual topography that was traced by the tip in the experiment (Fig. 2.18b). The orbital wavefunction ψ_{mo} is obtained from a density functional theory calculation. For the tip wavefunction ψ_{t} we assume a spherical s-wave as suggested by Tersoff and Hamann[94].

The resulting simulation of the lightwave-driven current is shown in Fig. 2.18d. It reproduces the salient features of the acquired snapshot very well, including the asymmetry of the map which stems from a slight shift of the in-gap topography, probably due to an asymmetric tip shape.

The best agreement between the experimental and simulated images is found for a tip s-wave with a decay length of 0.5 Å, which is consistent with an examination of the spatial resolution presented in the following paragraph.

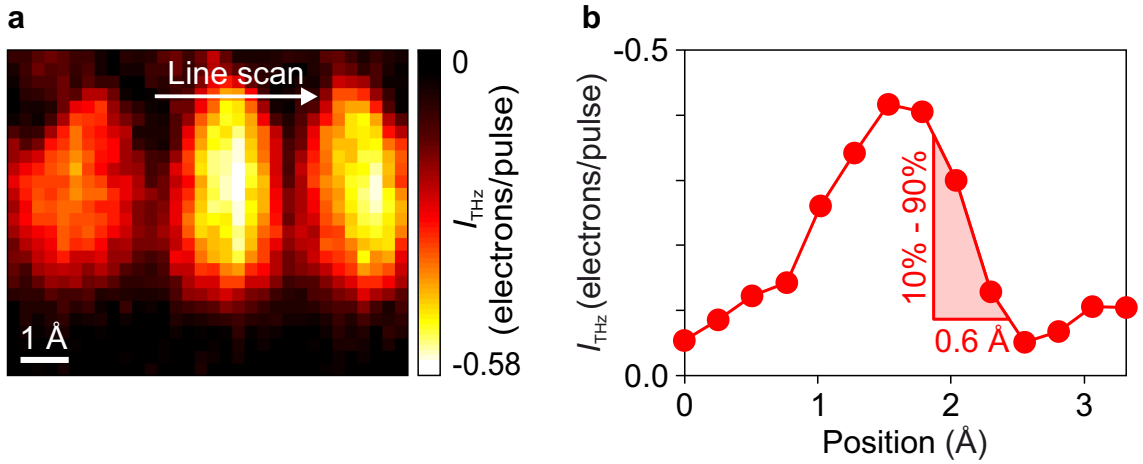

Figure 2.19 | Spatial resolution of lightwave STM. a, Constant-height, zero-bias lightwave STM snapshot of three central lobes of the pentacene HOMO. The image has a pixel size of 0.25 Å × 0.25 Å and contains edges where the signal increases from the background level to a maximum within 0.75 Å. **b**, A line scan (white arrow in **a**) illustrates that the signal rises from 10% to 90% over a range of approximately 0.6 Å at the steepest edge, which provides an upper bound for the spatial resolution.

Spatial resolution of lightwave STM. Ultrafast imaging can also be performed in constant-height mode, with the STM feedback loop and even the bias voltage completely turned off. In this way, the only tunnel current between tip and sample is the lightwave-driven component. Moreover, recording an image at constant height avoids any artifacts from the in-gap topography.

Figure 2.19a shows a zoomed-in snapshot image of the pentacene HOMO pattern obtained in this way. Three of the central lobes of the orbital wavefunction are imaged in more detail here. To obtain this image, terahertz pulses applied the only voltage to the junction. We directly measured the lightwave-driven tunnel current calibrated in electrons rectified per terahertz pulse on average. Tunnel rates with absolute values up to 0.58 electrons per pulse were detected, in agreement with the conjecture that every lightwave induces tunneling of one electron at most.

This snapshot exhibits precise sub-orbital features. In some regions, the lightwave-driven current is sharply defined by individual pixels (0.25 Å × 0.25 Å pixel size). We examine a horizontal line scan across one of the lobes in more detail. Figure 2.19b shows the lightwave-driven current measured pixel by pixel. On the right hand side of the lobe, the tunnel probability rises from the baseline value to the local peak

within a sub-Å distance. A 10% to 90% increase of the signal is observed across a spatial separation of only 0.6 Å.

This impressive spatial definition is indeed sharper than what is obtained in usual steady-state STM imaging with metallic tips. The tunnel integral picture presented above can explain this finding. In lightwave STM imaging where terahertz pulses apply the only bias voltage, the repetition rate of the laser limits the tunnel current. Consequently the tip can be approached more closely to the sample than in steady-state STM where strong tunnel currents at small tip heights cause mechanical instability. For lightwave-STM imaging, however, comparatively small tip-sample distances are actually required such that the tunnel barrier is narrow enough for electrons to tunnel within a sub-cycle time window. In addition, the tip and sample wavefunctions then produce a laterally sharper overlap, resulting in a better spatial definition of the tunnel current.

We note that, according to the tunnel integral (2.4), this spatial definition is generally limited by the sample wavefunction. Hence, the observed feature of 0.6 Å presents an upper bound for the spatial resolution of lightwave-STM imaging. Other samples with sharper electronic features might be observed with even higher spatial accuracy.

Temporal resolution of lightwave STM. The temporal confinement of the tunnel process can be extracted from an autocorrelation measurement on a pentacene molecule. To this end, we generate pairs of identical copies of the terahertz waveform, separated by a variable delay time, τ (Fig. 2.20a, inset). We tune the field strength of the individual pulses to approximately half of that needed to access the HOMO. As a result, when they are temporally separated, neither of the pulses can drive any orbital-resonant tunneling. If the delay time is chosen such that the waveforms overlap around $\tau = 0$ fs, however, constructive interference induces fields that are strong enough to facilitate HOMO tunneling. Indeed we detect lightwave-driven tunneling for delay times close to $\tau = 0$ fs (data points in Fig. 2.20a). When one of the pulses is delayed by more than ± 250 fs, however, the waveforms drive almost no measurable current.

The profile of this autocorrelation curve contains information about the temporal definition of lightwave-induced tunnel control. To extract this information, we

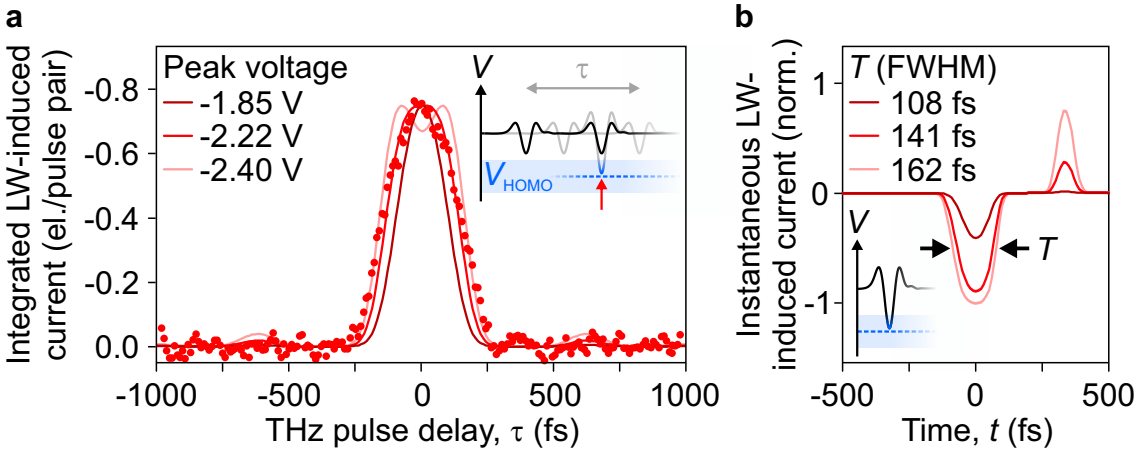

Figure 2.20 | Temporal resolution of lightwave STM. a, Autocorrelation measurement of HOMO tunneling induced by pairs of identical terahertz pulses. Whereas each individual pulse is set too weak to drive sequential tunneling (far-field amplitude 0.12 kV/cm), constructive interference at a delay time close to $\tau = 0$ fs (red arrow) should provide access to the HOMO resonance, V_{HOMO} (inset). The measurement indeed demonstrates that tunneling occurs only within an interference time window around $\tau = 0$ fs (red data points). A simulation of the sub-cycle tunnel rate provides fit curves to the autocorrelation (red lines). Best agreement is found when we assume a combined peak voltage of -2.22 V upon constructive interference of both pulses at $\tau = 0$ fs. **b**, Simulated instantaneous tunnel rates for single HOMO-resonant THz pulses (inset) that exhibit the peak voltages indicated in **a**. For small voltages, the main burst of tunnel current becomes as short as approximately 100 fs (T, arrows, FWHM).

simulate the sub-cycle tunnel confinement and fit our model to the measured autocorrelation curve.

In this model calculation, for simplicity we assume that the lightwave-induced voltage waveform across the tunnel junction, $V_{\mathrm{THz}}(t)$, is similar to the far-field waveform coupled into the STM. As mentioned before, this issue will be addressed in detail in chapter 4. In the present context, we approximate the near-field transient by the waveform, $E_{\mathrm{EOS}}(t)$, detected electro-optically in the far field (Fig. 2.15c). The only fit parameter in our model is a proportionality scaling factor, calibrating the field waveform in terms of the voltage $V_{\mathrm{THz}}(t)$ that it transiently applies between tip and molecule. For every delay time τ, we calculate the temporal interference pattern of both voltage waveforms, $V^{\tau}_{\mathrm{THz}}(t)$, emulating the incident waveforms in

the autocorrelation experiment. Now we aim to simulate the instantaneous tunnel current that these interference patterns induce.

To this end, we measure the steady-state tunnel rate as a function of the applied bias voltage, $I(V_{\mathrm{bias}})$. When we assume that this relation also holds true for transient voltages varied at terahertz rates, we can calculate the instantaneous tunneling current driven by the interfering pairs of waveforms

$$I^{\tau}(t) = I(V^{\tau}_{\mathrm{THz}}(t)). \tag{2.5}$$

The integral of this current burst corresponds to the net charge that we expect a pair of waveforms, separated by a delay time τ, to tunnel on average. This is exactly what we measure in the autocorrelation experiment. Solid lines in Fig. 2.20a show this integrated current that we calculate.

We now vary our only fit parameter, which effectively scales the terahertz field strength. The three lines in Fig. 2.20a depict the results for different peak fields. Smaller fields yield a narrower autocorrelation curve, whereas larger peak fields lead to a split autocorrelation crest and emerging side peaks from neighboring waveform cycles. The simulation with a combined peak voltage of $-2.22\,\mathrm{V}$ upon constructive interference at $\tau = 0\,\mathrm{fs}$ agrees best with the measured autocorrelation curve.

Having gauged[b] the peak field in our simulation, we can examine the instantaneous current burst driven by a single pulse, which describes for example the recording of an orbital snapshot. When a single terahertz waveform is tuned such that its peak field accesses the HOMO resonance, we expect ultrafast current bursts as shown in Fig. 2.20b. These curves visualize the ultrafast opening and closing of sequential tunneling channels, allowing us to assess the temporal resolution of lightwave-driven tunneling.

Three current pulses are shown for the same peak voltages as indicated in panel a. Whereas so far, we labeled the maximum peak voltage of the interference waveform, here, the single-pulse peak is described. In this calculation, for simplicity, we do not consider resonance shifts upon charging. What we observe is that strong pulses induce a main current burst out of the HOMO ($I < 0$), followed by a short window

[b] This calibration procedure also allowed us to specify the lightwave-induced peak field in Fig. 2.16 in units of volts.

of LUMO tunneling in the opposite direction ($I > 0$). Weaker pulses that only just access the HOMO resonance, however, drive solely uni-directional electron tunneling from the HOMO. In addition, the time window of this current burst becomes smaller the more scarcely the waveform accesses the nonlinear HOMO tunnel resonance.

For all shown peak voltages, the full width at half maximum of this time window is just above 100 fs. The corresponding 10% to 90% rise times of the average rectified charge are even shorter. In subsequent experiments, the fields steering lightwave-driven tunneling are chosen as low as possible for an optimal temporal resolution. The field strength that was applied to record the HOMO snapshot in Fig. 2.18c, for instance, confined tunneling to a time window of only 115 fs.

Integrating any of these current waveforms yields the average number of electrons that are tunneled by one terahertz pulse. We did so for a range of assumed terahertz peak voltages, and thereby obtained a simulation of the onset curve shown in Fig. 2.16 (black line), which agrees well with the data.

Altogether, these results suggest that the initially presented semi-classical picture of ultrafast lightwave-driven sequential tunneling is valid. Transient, waveform-controlled energy level alignment can indeed steer tunneling of a single electron with a combined spatial precision better than 0.6 Å and temporal accuracy on the order of 100 fs. Moreover, this process is state-selective, opening the door to ultrafast atom-scale microscopy and spectroscopy of the electronic structure of atoms, molecules, surfaces, photocatalysts, biomachines, nanocircuitry, and many more.

2.3 Single-electron injection triggers ultrafast structural dynamics

Ultrafast electron tunneling might not only serve to probe nanosystems, but could already trigger atomic-scale dynamics indirectly, via local electronic excitation. This section will demonstrate that, indeed, single-electron tunneling through a molecular orbital entails a prominent structural vibration of the molecule. We will directly trace the molecular motion subsequent to a charging event in the time domain and compare the oscillatory behavior of different species.

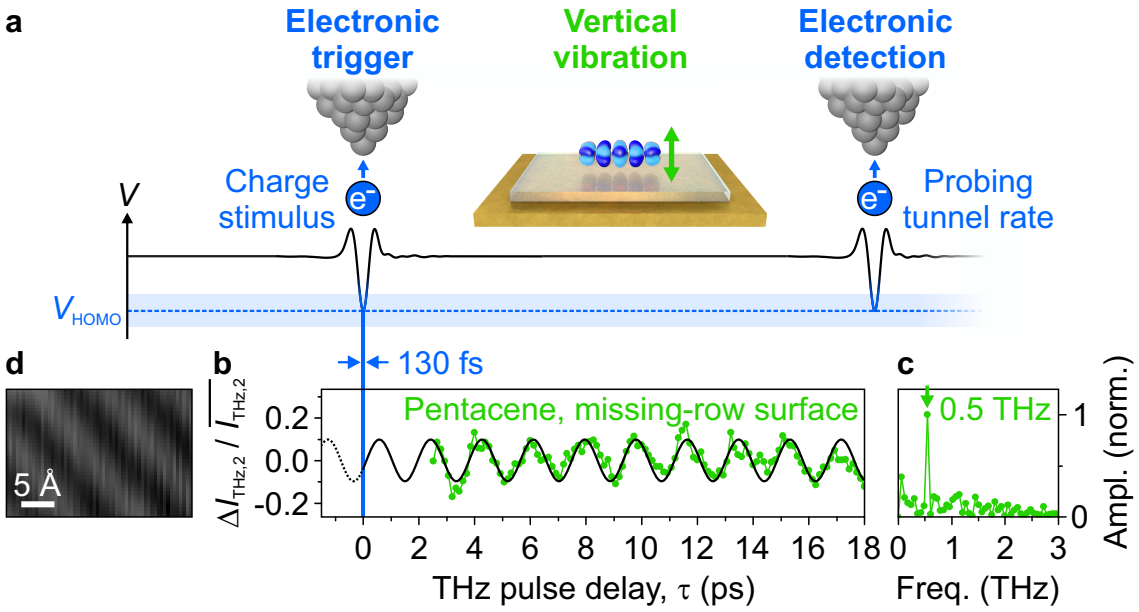

Figure 2.21 | Charge-triggered femtosecond dynamics of a single molecule. **a**, In a pump-probe experiment, dynamics of a single pentacene molecule are excited and time-resolved by single-electron tunneling. Pairs of lightwaves are generated where both transients are tuned in resonance with the HOMO voltage, V_{HOMO}. The first pulse (pump) removes an electron from the HOMO and thereby excites a vertical vibration of the molecular frame. The second pulse (probe) detects the instantaneous height of the oscillating molecule encoded in the transient tunnel rate. **b**, The relative change of the probe-induced tunnel current, $\Delta I_{\mathrm{THz},2}(\tau)/\overline{I_{\mathrm{THz},2}}$, exhibits a coherent oscillation as a function of the pump-probe delay time, τ (sinusoidal fit shown as black curve). The corresponding Fourier spectrum (**c**) reveals a sharp peak at a frequency of 0.5 THz. Electron injection by the pump pulse is confined to a time window of 130 fs, which allows detection of the 0.5 THz molecular vibration with a well-defined phase. **d**, Constant-current DC-STM image of the NaCl/Au(110) substrate used in this measurement. The missing-row Au(110) reconstruction beneath the monolayer NaCl film appears as a stripe pattern. Linear grayscale range of 2.0 Å.

Ultrafast pump-probe scheme: charge stimulus. To this end, we set up a pump-probe experiment where we employ pairs of terahertz pulses, both of which access the HOMO resonance of a pentacene molecule (Fig. 2.21a). If electron extraction driven by the first pulse (pump) excites any dynamics of the molecule, the second pulse (probe) will encounter the molecule "in motion". Varying the delay time between both pulses should allow the second pulse to stroboscopically probe different phases of the dynamics, directly in the time domain. Such an excitation could in principle entail translational motion, internal vibrations and electron dynamics. If they affect the tunneling probability, these dynamics should be encoded in the tunnel events that the probe pulses drive.

We record[c] the probe-induced component of the current, $I_{\mathrm{THz},2}$, and vary the delay time τ between both pulses. Figure 2.21b shows the stroboscopic change of this current, $\Delta I_{\mathrm{THz},2}(\tau) = I_{\mathrm{THz},2}(\tau) - \overline{I_{\mathrm{THz},2}}$, normalized to the running mean of the signal, $\overline{I_{\mathrm{THz},2}}$.

The time-resolved probe current indeed shows a marked oscillation at a frequency of 0.5 THz, confirmed by a sharp peak in the corresponding spectrum (Fig. 2.21c). Eight periods of this clear harmonic signal can be observed in the time window between 2.5 ps and 18 ps after pump excitation. Throughout this range, the modulation of the probe current amounts to approximately ±10% without any appreciable decay.

Single-molecule structural vibration. We interpret this behavior as a single-molecule manifestation of the Franck-Condon principle. The adsorption geometry of the molecule is determined by its van der Waals interaction with the substrate. Charging the molecule with a pump pulse abruptly changes Coulomb and van der Waals forces, and thereby modifies the potential landscape. We expect this impulse to trigger a predominantly vertical vibration of the molecule due to Coulomb interaction with image charges[95].

As a consequence of the high tunneling rate through the underlying NaCl monolayer, the molecule is neutralized[96] again within roughly 100 fs and ends up in a vertical oscillatory mode about the neutral equilibrium height. When we apply a sub-

[c] To record the tunnel current driven solely by the probe pulses, they are modulated separately by a mechanical chopper, and the overall tunnel current is demodulated at this respective modulation frequency.

sequent probe pulse while the molecule is in motion, its transient position determines the tunnel barriers between tip, molecule and substrate.

We have observed similar pump-probe signals with identical phase across the entire molecule, reproducible for different molecules. So the dynamics resolved here appear uniform and do not exhibit any in-plane variation. This observation strongly supports the conjecture that the tunnel-induced motion is a vertical vibration. Hence, the tunnel current driven by the probe pulses $I_{\mathrm{THz},2}$ directly samples the molecule's vertical position as a function of delay time τ.

While such a comparatively simple mode appears ideally suited for an initial study, also much more complex patterns of motion can be driven in other molecular systems. Later in chapter 3, for example, we will steer rotational and even unidirectional dynamics that involve internal degrees of freedom of a single molecule.

Average values of statistical events. To interpret this and subsequent experiments, it is essential to conceive the statistical nature of tunnel processes. As demonstrated above, our scheme of lightwave control steers tunnel events with a probability below one electron per pulse on average. This is not a technical limitation, but rather illustrates the intrinsic quantum-probabilistic nature of single-electron femtosecond tunneling, which lightwave STM has just provided access to for the first time.

The picture of the pump-probe scenario drawn above describes precisely those cases where, by quantum chance, both the pump and the probe pulse successfully tunnel an electron out of the HOMO. When the experiment is repeated many times, these instances make up only a fraction of all pulse pairs. In some cases, only one of the pulses, or neither of them, may induce electron tunneling. At an approximate tunnel probability of 50%, for example, only one fourth of all pulse pairs would both excite and probe molecular motion.

Altogether, we observe a clear average time-dependent signature in the probe-induced current, which stems from exactly these instances. Here in our first study on molecular dynamics, we describe such average quantities to begin with. For experiments discussed later, however, it will become vital to precisely distinguish different scenarios of quantum processes that can occur statistically. To this end, in chapter 3 I will introduce a novel detection strategy that analyzes individual events with single-shot accuracy.

Oscillatory amplitude. Assuming that the ±10% modulation of the average probe current stems from a modification of the barrier width as a result of the molecule's motion, the average oscillation amplitude can be roughly estimated. Often tunnel rates in STM decay exponentially by approximately one order of magnitude per 1 Å distance increase. This is evident from many experiments and can be calculated in a WKB picture where typical metal work functions[97] yield barrier heights of approximately 5 eV. If a similar decay rate describes sequential tunneling driven by the probe pulses, we obtain an average oscillatory amplitude of the molecule of 4 pm. This is on the order of the quantum of excitation of such a single-molecule harmonic oscillator. We expect that future experiments might capture ultrafast nanodynamics purely governed by quantized states directly in space and time.

Influence of molecule-substrate interaction. The vibrational pattern we observe here, including its amplitude and frequency, is characteristic of the molecule-substrate interaction. The corresponding energy landscape should depend critically on the structure of the molecule and the underlying surface. To demonstrate this, first, we modify the substrate surface and analyze how the vibrational mode changes.

The substrate used in these experiments is a Au(110) surface covered with a monolayer of NaCl. When a gold crystal is cut in (110) direction, its surface typically reconstructs such that every other row of atoms of the surface layer is left out[98]. In the experiments demonstrated so far, this so-called "missing-row" reconstruction was present underneath the NaCl monolayer islands. Steady-state images of the bare NaCl surface show this unique pattern (Fig. 2.21d). The residual half of atomic rows of the surface layer appears as prominent stripes with a distance of 8.2 Å.

Growing NaCl layers at a higher temperature allows us to remove the reconstruction. A substrate prepared in this way possesses a different surface structure, as shown in Fig. 2.22a. The absence of the missing-row reconstruction is evident from the fact that the stripe pattern that we see in Fig. 2.21d is missing in Fig. 2.22a. Here, instead, the surface features a Moiré pattern emerging from the different lattice constants of the NaCl layer and the Au crystal.

When we repeat the above pump-probe experiment with this new substrate, we find that pentacene molecules adsorbed on this surface indeed vibrate at a different frequency: The time-resolved probe current reveals a softer mode (Fig. 2.22b), oscil-

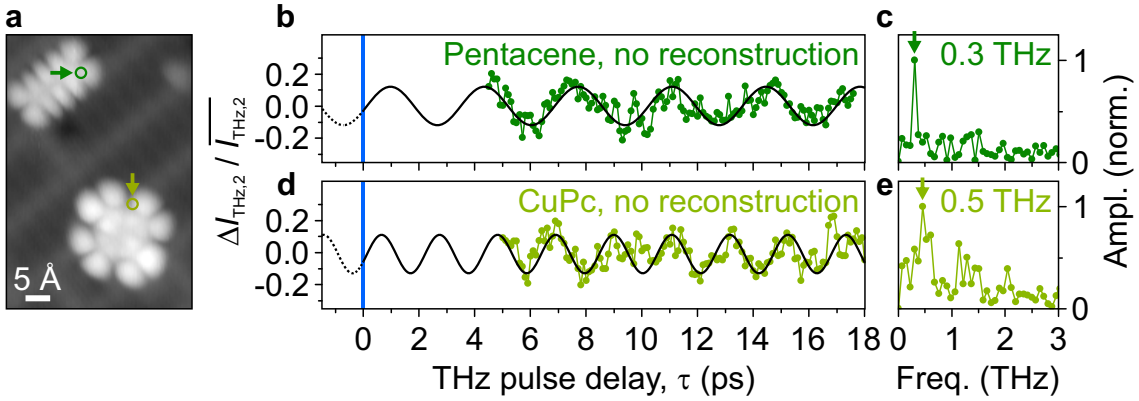

Figure 2.22 | Influence of substrate surface and molecular species on ultrafast single-molecule dynamics. a, Constant-current DC-STM image of the highest occupied molecular orbitals of a pentacene molecule (top left) and a copper phthalocyanine molecule (bottom right), which are adsorbed next to one another on a NaCl monolayer island ($V_{DC} = -1.75\,V$, $I = 0.83\,pA$, grayscale range = 3.0 Å). On this surface, the missing-row reconstruction had been removed. **b**, Time-resolving the ultrafast dynamics of this pentacene molecule in a similar experiment as shown in Fig. 2.21, we observe a coherent oscillation, but at a different frequency of 0.3 THz (tip position indicated by a dark green circle in **a**, spectrum shown in **c**). **d**, A pump-probe measurement recorded over the copper phthalocyanine molecule with identical experimental conditions exhibits a coherent modulation at a frequency of 0.5 THz (tip position indicated by an olive green circle in **a**, spectrum shown in **e**). Tracing each sinusoidal fit (black curves) back to $\tau = 0\,fs$ reveals a consistent absolute phase with a temporal offset of less than 130 fs (vertical blue belt). The sinusoidal fit to the oscillation in Fig. 2.21b yields the same phase.

lating at a frequency of 0.3 THz (Fig. 2.22c). Because this surface is less corrugated than the missing-row reconstruction, one may consider it more inert from a geometrical point of view. The molecule-substrate interaction should be weaker in this case, which agrees with the observed softer mode.

Moreover, when we probe another molecular species, we observe different interaction energetics as well: Copper phthalocyanine (CuPc) molecules adsorbed on the very same substrate without reconstruction vibrate at a predominant frequency of 0.5 THz (Fig. 2.22d,e), which is higher than that of pentacene. This is consistent with the slightly polar character of the bonds inside CuPc that should cause CuPc to interact more strongly with the ionic NaCl layer, and thereby stiffen the binding to the substrate.

In different experiments, similar frequencies of vertical molecular vibrations around $1.5 - 2\,\mathrm{THz}$ have been reported for hydrocarbons adsorbed on Cu(110)[99] as well as Ru(0001)[100]. One can expect that introducing an insulating film between molecule and metal support substantially weakens the adsorption interaction. Hence the oscillatory frequencies of $0.3 - 0.5\,\mathrm{THz}$ that we observe lie precisely in the range where they are expected.

Most importantly, our dataset rules out a number of potential artifactual origins of the pump-probe signal. In principle, if there were trailing oscillations of the near-field waveform, this might also cause pump-probe signals via interference. Plasmonic and antenna resonances of the tip or the entire junction could induce such oscillatory signals through standing waves. Also other surface modes could be coherently excited and influence the tunnel rate as a function of τ. However, we observe different oscillation frequencies on two different molecules adsorbed only a few Å apart with otherwise identical experimental conditions, which rules out any of these artifacts. Moreover, we found that a slight modification of the substrate surface alone can drastically influence the oscillation frequency that we observe. This corroborates our picture that the molecule vibrates in its van der Waals adsorption potential.

Delay times earlier than 2 ps have not been accessed to avoid interference between pump and probe waveforms. Tracing the harmonic patterns back to the trigger event at $\tau = 0\,\mathrm{ps}$, however, shows that the oscillatory phase is the same in all observed vibration patterns, regardless of their frequency (Fig. 2.21b, 2.22b, 2.22d). The signal follows a sine function with zero phase, consistent with an impulsive excitation in the 130-fs-long time window of the pump charge stimulus. We note that this phase is well-defined only because the pump-induced tunnel trigger is confined to a time window much shorter than the oscillatory period of 2 ps. Also we find that, in contrast to frequency-based spectroscopy, our coherent pump-probe-scheme reveals surface modes that are usually obscured by incoherent broadening.

○

These experiments demonstrate that tip-confined terahertz waveforms allow us to trigger single-electron tunneling through a select orbital of one individual molecule. With a combined 0.6 Å and ~100 fs spatio-temporal precision, this novel energy-selective process allows us to record femtosecond snapshot images of a single-molecule

orbital. Also, electron injection indirectly triggers a dominantly vertical picometer vibration of the molecular frame, which we directly resolve in pump-probe experiments. Varying the surface of the substrate and the molecular species, we find that the observed dynamics encode the molecule-substrate interaction.

We expect that these experiments pave the way for a broad range of future studies that capture electronic and structural dynamics of a variety of excitations in ultrafast atom-scale movies.

3 Femtosecond atomic forces choreograph reactions of a molecular switch

Atomic forces have shaped matter atom by atom[51,62,101,102]. Novel artificial structures have been assembled[50,63] and (bio)chemical processes can be influenced via atomic forces[103–105]. Exploiting local, ultrafast dynamics[40,106–109], however, could introduce a new era in nanotechnology where we coherently control matter at the single-atom level. Femtosecond atomic forces could directly arrange matter in exotic and "hidden" states, push quantum information processing to ultimately small scales or tailor chemical reactions of single molecules at will. So far, an ultrafast and at the same time atomically localized force stimulus has remained a theoretical concept, however.

In this chapter, I will show that the tip-confined near field of a terahertz waveform can act as an *atomic-scale femtosecond force* on key atoms of a molecular switch. This local manipulation prepares a select rotation of the molecule, which strongly influences its reactivity during the controlled motion. To visualize the impact of the force on the molecule's switching behavior, we develop a novel single-shot detection scheme appropriate for the statistical nature of atom-scale (quantum) dynamics. In this way, we directly monitor every reaction event of the switch and resolve the entire statistics of different reaction paths (section 3.1). We find that the force-controlled dynamics of the molecule transiently modify its reaction rates by up to 39% on the femtosecond scale (section 3.2). An ultrafast movie of the switching statistics confirms the atomic definition of the ultrafast force stimulus (section 3.3).

This chapter follows the presentation in reference 21.

Demand for a novel control stimulus. To illustrate why local femtosecond forces can be expected to be an ideal stimulus for immediate structural control at the atomic scale, it is instructive to detail how, in contrast, electronic excitation triggers structural motion indirectly. The experiments discussed so far show that lightwave-driven femtosecond tunneling allows us to induce and track a vertical single-molecule vibration. But as a matter of fact, electron tunneling entails this motion rather as an inevitable effect than in a precisely controlled way. This electronic stimulus cannot selectively address a particular degree of freedom, or even steer motion coherently and in a particular direction on purpose.

At the nanoscale, dynamics of several degrees of freedom that occur on different time scales are often intertwined. This holds true for single molecules which may undergo structural reactions in response to photoexcitation or ionization[110–112]. Similarly, the experiments presented above demonstrate how electronic excitation of a single adsorbed molecule can induce structural wavepacket motion. And also in solids – in particular in strongly correlated materials[113,114] as well as nanostructures[115] – the charge, spin and lattice degrees of freedom can be massively interdependent, giving rise to phase transitions and rich electromagnetic features. In strongly correlated solids, for example, (meta)stable configurations with intriguing properties may exist in regions of phase space that are not accessible thermodynamically. Transitions to such a "hidden phase" can sometimes be induced indirectly, for example as a collateral effect after drastic photoexcitation[116–118]. Similarly, in the experiments presented above, electronic excitation of a single molecule entailed a structural vibration, but without providing explicit control over the induced motion pattern.

In all these settings, one can indeed impulsively drive a nanosystem out of equilibrium. But as the available indirect stimuli are generally rather unspecific, it is not possible to steer any degree of freedom at will and independently, restricting our access to a very limited range of all possible configurations in phase space. To manipulate the state of matter ad lib., one would need an ultrafast atomic-scale stimulus that allows one to steer *select* degrees of freedom and coherently compose motion through phase space.

Specifically in chemistry, a major dream has been to choreograph a reaction of an individual molecule by steering key atoms in slow motion. However, such a degree of control has been completely out of reach so far for the lack of a selective, local and

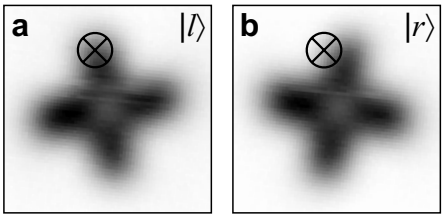

Figure 3.1 | Ground states of a single-molecule bistable switch. Steady-state images of the two ground states $|l\rangle$ (**a**) and $|r\rangle$ (**b**) of a MgPc molecular switch. Constant height measurements, $V_{\mathrm{bias}} = 6\,\mathrm{mV}$, image size $= 20\,\text{Å} \times 20\,\text{Å}$, grayscale range $= 0 - 2\,\mathrm{pA}$. Lattice axes of the underlying NaCl substrate align with the frames.

ultrafast stimulus. The present chapter will introduce femtosecond atomic forces to tackle precisely this challenge.

Molecular reactions govern (bio)chemical function. When molecules react chemically[111,112], change their conformation[41,110] or desorb catalytically[119], they switch between two stable states that are separated by an energy barrier. The question how external stimuli influence such transitions lies at the heart of biological function[110] and photochemistry[120]. As an example from this class of dynamics, we pick a single-molecule switch to explore molecular reactions.

Bistable molecule as prototype switch. We choose a molecular switch that has already been characterized through time-integrated experiments[121,122]. The switch consists of a bistable magnesium phthalocyanine (MgPc) molecule adsorbed on a NaCl surface. In STM, we implement the support surface using a copper (111) crystal as a substrate and growing multilayer islands of NaCl on top to host the switch. When we record steady-state STM images, we find that one and the same molecule can appear different in subsequent measurements. Figure 3.1 shows maps of non-resonant tunnel current at constant tip height. Scanning across the molecule yields a cross-shaped in-gap pattern that is slightly rotated with respect to the NaCl lattice axes (Fig. 3.1a). The very same molecule can also appear different in a second, identical measurement (Fig. 3.1b). Here the cross shape is rotated reversely with respect to the underlying substrate.

These are images of the two equivalent ground state configurations of the switch. As will be described in the following, a delicate balance of local atom-scale interactions between molecule and sample gives rise to a multifaceted potential landscape[121,122]. When the molecule is adsorbed centered on a chlorine site of the NaCl lattice, it can

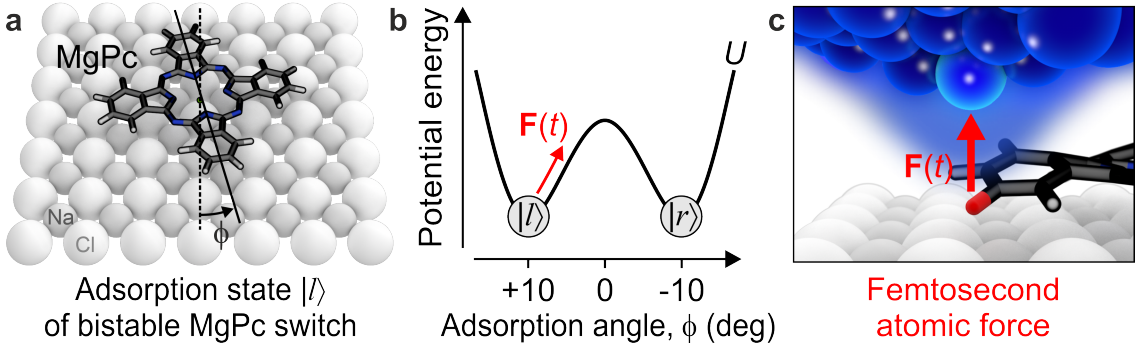

Figure 3.2 | Structural motion steered by femtosecond atomic forces. a, Adsorption geometry of MgPc (stick model) on a NaCl layer (spherical ions). In ground state $|l\rangle$, the molecular axes are rotated by an azimuthal angle $\phi \approx +10\,\text{deg}$ with respect to the underlying NaCl lattice. State $|r\rangle$ is mirror-symmetric. **b**, The adsorption energy as a function of azimuthal angle describes a double-well potential, $U(\phi)$, with two degenerate minima ($|l\rangle$ and $|r\rangle$ at $\phi \approx \pm 10\,\text{deg}$), separated by a barrier. Femtosecond atomic forces, $\mathbf{F}(t)$, might allow us to dynamically navigate on this potential energy surface. **c**, To steer a select degree of freedom of the switch, ultrafast atomic forces (red arrow) confined to the tip apex (blue spheres) act on a key atom (red stick) of the molecule.

align in either of two symmetric ground state geometries. Figure 3.2a schematically illustrates one of the two states. The ions of the top-most NaCl layer are shown as spheres across a plane, and the molecule is depicted in a stick model of covalent bonds. The geometry of the molecule has been calculated based on density functional theory. Details about all calculations presented in this chapter are provided in reference 21.

Ground state geometry. What strikes the eye about this ground-state configuration is the fact that the molecule does not align with its four isoindole units along the NaCl lattice directions. In contrast, the molecule breaks the symmetry: It appears slightly rotated by an azimuthal angle, ϕ, of approximately $+10\,\text{deg}$. We denote this adsorption state $|l\rangle$ and call the mirror symmetric geometry where the molecule is rotated by $\phi \approx -10\,\text{deg}$ state $|r\rangle$, respectively. Because these two stable configurations are the ground states of the geometry, they must be separated by an energy barrier. So the adsorption energy, $U(\phi)$, as a function of azimuthal angle describes a double-well potential[121,122] with degenerate minima at $\phi_l \approx +10\,\text{deg}$ and $\phi_r \approx -10\,\text{deg}$ (Fig. 3.2b).

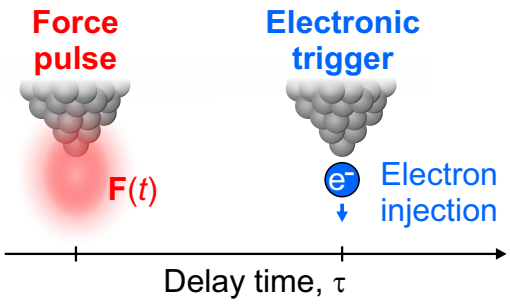

Figure 3.3 | Force-pump charge-probe experiment. We apply a tip-confined force pulse $\mathbf{F}(t)$ to steer molecular dynamics, and time-resolve the impact on the molecule's transient switchability with a delayed electron injection.

Steering structural motion. To trigger structural motion in this potential, one could envisage indirect mechanisms of exciting the molecule. Subsequent to electronic or optical excitation, for example, the molecule might move in azimuthal direction – in a manner hard to predict or even control. The most direct way to navigate on this potential energy surface, in contrast, is to exert local forces on the molecular frame that leave the electronic system in its ground state (arrow in Fig. 3.2b). While static forces, which have been available with scanning probe microscopy[50,51,63,101,102], could in principle induce a constant excursion of the switch, a time-dependent force pulse, $\mathbf{F}(t)$, may dynamically steer the system through its configuration space. If the force pulse is fast enough, one could even exploit ultrafast resonances about a potential minimum and steer the evolution of the switch fully coherently. An atomically sharp femtosecond force could selectively steer the key interacting atoms of the system (Fig. 3.2c) to prepare a coherent structural motion along a select degree of freedom.

This chapter will demonstrate that a tip-confined terahertz waveform can provide such an atomically sharp femtosecond force $\mathbf{F}(t)$. Our idea is to expose the switch to such a local force pulse and interrogate its response with a delayed injection of an electron into a molecular orbital. This stroboscopic pump-probe scheme is visualized in Fig. 3.3.

Force-pump electronic-probe sequence. As will be detailed in the following, the effect of a local force pulse and an electron injection on the switch are entirely different. Therefore we systematically analyzed the effects that both stimuli have on the molecule separately. To facilitate the discussion, first, I will summarize the behavior of the switch during a full force-pump electronic-probe sequence, which is presented in the next paragraph. After this overview, I will systematically discuss the individual stimuli separately.

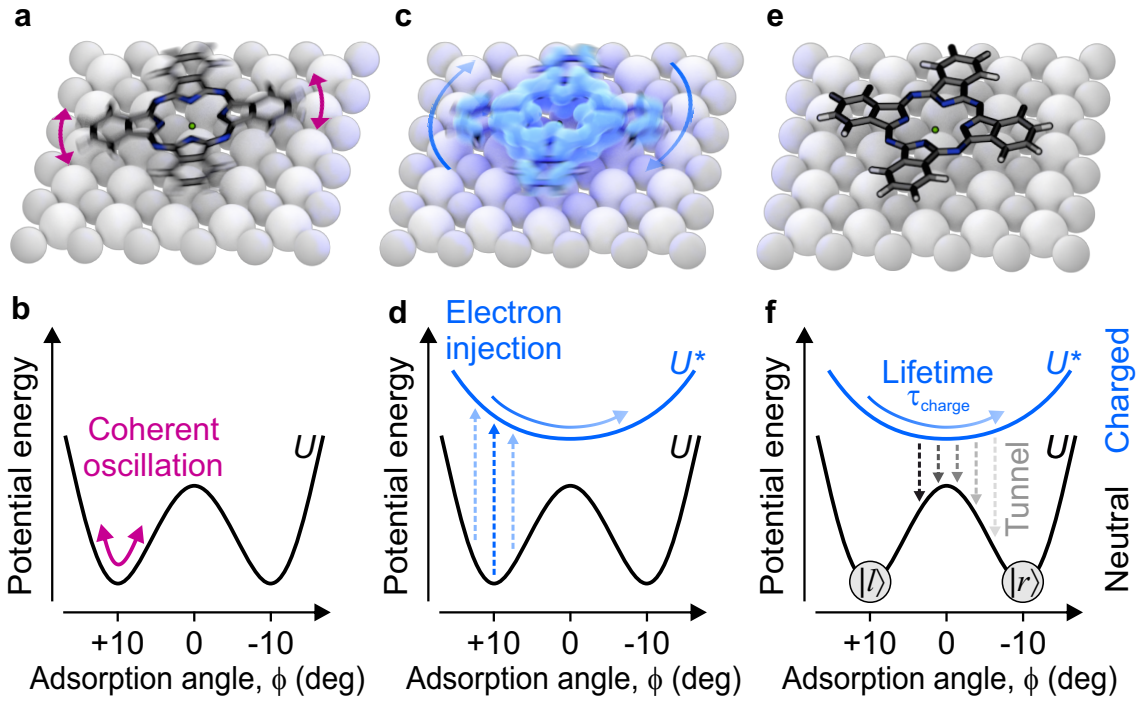

Figure 3.4 | Transient switchability probed via electron injection. **a**, When suitably steered, a MgPc switch in its neutral ground state $|l\rangle$ may be prepared to perform a coherent in-plane rotational motion about $\phi \approx +10\,\mathrm{deg}$. **b**, Such a frustrated rotation could be exploited to control transient switching dynamics, where the molecule has to overcome an energy barrier to arrive in state $|r\rangle$. Since the charged molecule energetically prefers aligning with the lattice directions (**c**), electron injection into the LUMO (**d**, vertical transitions) establishes a new energy landscape (**d**, cyan curve). This sudden change prompts an in-plane rotation of the molecule towards $\phi = 0\,\mathrm{deg}$, strongly influenced by the previous rotational dynamics (multiple vertical transitions in **d**). Tunnel neutralization restores the original bistable potential, such that the molecule can relax to either state $|l\rangle$ or $|r\rangle$ (state $|r\rangle$ shown in **e**). **f**, The neutralization event can stochastically occur at different instants in time (decay lifetime τ_{charge}, multiple downward arrows), such that the outcome of every individual switching process is governed by quantum probability.

It will be shown below that our ultrafast tip-confined force can steer a coherent frustrated rotation of the molecule about one of the potential minima. In real space, this motion corresponds to an azimuthal vibration of the entire molecular frame. Figures 3.4a and b illustrate the molecule oscillating about its ground state $|l\rangle$. Such force-induced structural dynamics can be even strong enough to influence the probability of switching between the molecule's adsorption states $|l\rangle$ and $|r\rangle$.

To demonstrate this, we interrogate the switching probability with a delayed electron injection. We exploit lightwave-driven tunneling into the LUMO to perform a precisely timed charging event, similar to the procedure described in chapter 2. Because the potential of the charged molecule, $U^*(\phi)$, has its minimum around $\phi = 0\,\mathrm{deg}$[121,122], electron injection will cause the molecule to rotate towards geometry $|r\rangle$ (Fig. 3.4c,d). Then after a statistical lifetime, τ_{charge}, the additional electron tunnels into the substrate and the double-well potential is restored. The molecule will relax to either $|l\rangle$ or $|r\rangle$, depending on the quantum probabilistic lifetime of the charged state (Fig. 3.4e,f).

If initially – at the moment where an electron is injected – the molecule is not resting in its ground state, it may follow different trajectories through phase space (vertical blue arrows in Fig. 3.4d). Particularly when the molecule is subject to a force-driven coherent oscillation, its switching probability could be strongly modulated on ultrafast time scales. To understand the impact of the force on the switching statistics, in the following, we will first examine the probing mechanism in detail, i. e. charge-induced switching. In particular, we will explore how single-electron injection can be used to time-resolve the transient reaction statistics of the molecular switch on the femtosecond scale.

Time-integrated observation of switching. The idea that orbital-resonant electron tunneling triggers the switch has been confirmed with time-integrated STM[121,122]. This experiment is briefly reproduced here for illustration. We increase the bias voltage such that LUMO tunneling repeatedly charges the molecule. Now the switch starts to toggle back and forth continuously, which becomes directly evident when we record a map of the LUMO density.

Figure 3.5a illustrates the simulated LUMO wavefunction, which exhibits nodal planes along the isoindole units. In the measured LUMO topography (Fig. 3.5b),

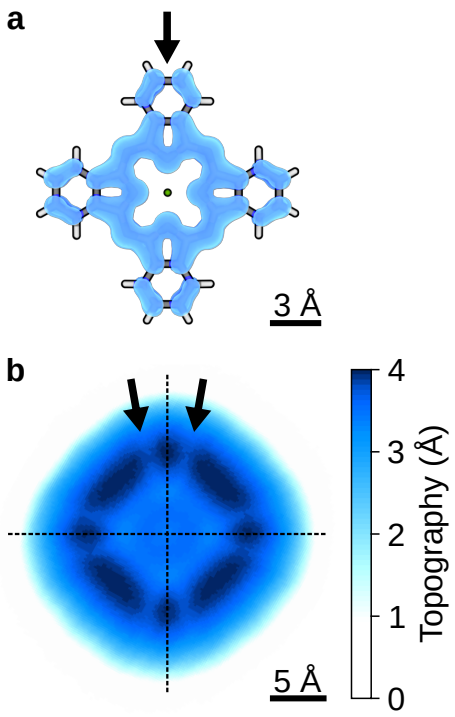

Figure 3.5 | Time-integrated orbital imaging confirms switching. a, Simulated LUMO wavefunction of MgPc. Shown is a stick model of the molecule, together with an isosurface of the LUMO amplitude. Electronic nodal planes are centered on the isoindole units (arrow). **b**, Measured constant-current topographic map of the LUMO density ($V_{\mathrm{DC}} = 1.1\,\mathrm{V}$, $I = 2\,\mathrm{pA}$). Repeated sequential tunneling events trigger the switch back and forth numerous times during acquisition of every single pixel. Hence the map represents a superposition of the electron densities in both orientations $|l\rangle$ and $|r\rangle$. This is illustrated by pairs of local depressions (arrows) around the NaCl lattice directions (dashed lines), which derive from the individual electronic nodal planes in each of the adsorption geometries $|l\rangle$ and $|r\rangle$.

however, the nodal planes appear doubled.

During the acquisition of this map, millions of electrons are tunneled for every pixel to generate a measurable current. Meanwhile, the repeatedly charged molecule switches back and forth numerous times such that the recorded image shows a superposition of the LUMO densities in both geometries $|l\rangle$ and $|r\rangle$. This mixture of adsorption states manifests in the map as pairs of nodal planes (arrows in Fig. 3.5b) rotated by approximately $\pm 10\,\mathrm{deg}$ with respect to the NaCl lattice axes (dashed lines).

No separate observation of the individual adsorption states is possible in this way. In contrast, non-resonant tunneling where electrons must tunnel directly from the tip into the substrate does not charge the molecule. Making use of this process allows us to image the orientation of the two ground states separately (Fig. 3.1). We build on this mechanism to develop a novel single-shot detection scheme based in non-invasive monitoring of the switch.

3.1 Single-shot detection of unidirectional switching events

Having imaged the molecule constantly switching back and forth in steady-state STM (Fig. 3.5), the stage is set for examining the switching process itself. Intriguingly, even very fundamental questions are completely open here. It is unclear, for example, whether the switch toggled only a few times during acquisition of every pixel, or millions of times. Also we cannot tell whether both switching directions perform equally, or if the symmetry between $|l\rangle$ and $|r\rangle$ is somehow broken in the experiment. As long as we lack quantitative data on the reaction statistics, there is no way to rationalize and influence them.

Characterizing such a molecular switch quantitatively to address these issues, however, is a challenge. This is because, in contrast to the dynamics studied in chapter 2, the MgPc switch does not perform the same motion after every tunnel event. Its quantum mechanical charge lifetime imposes non-deterministic, statistical motion in response to every single electron injection. The steady-state map of the LUMO densities (Fig. 3.5b) drastically illustrates this uncontrollable intermixture of states in recurrent scenarios.

As a consequence, traditional repetitive pump-probe experiments cannot be applied here as they require well-defined, repeatable dynamics. The MgPc statistical switch, however, will not even relax into the same initial state after every light pulse. On the contrary, the outcome of every laser shot has to be evaluated, one by one.

Single-shot action spectroscopy. We tune the terahertz field to trigger LUMO tunneling (Fig. 3.6a) and operate the optical source in single-shot mode. At the same time, we apply a small bias voltage that constantly drives a non-resonant tunnel current to observe the molecule without switching it. If we position the tip at a coordinate where this non-resonant detection current, I_{det}, is different for $|l\rangle$ and $|r\rangle$ (e.g. cross hairs in Fig. 3.1), we can monitor the adsorption geometry even without taking images.

Figure 3.6b shows a typical time trace acquired while individual terahertz pulses were repeatedly injecting single electrons into the LUMO. The arrival of the laser

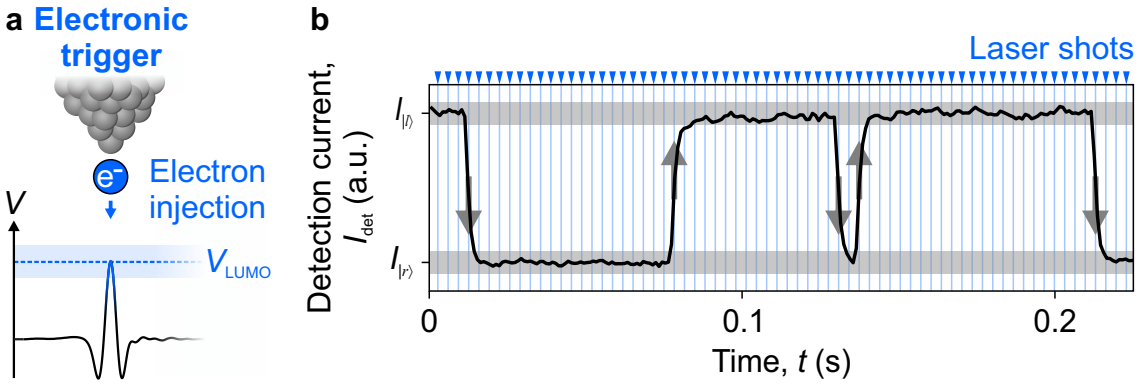

Figure 3.6 | Single-shot switching detection. **a**, Tip-confined lightwaves are tuned to access the LUMO orbital resonance, V_{LUMO}, and thereby drive single-electron injection as described in chapter 2. **b**, Keeping the tip at a fixed position above the molecule (e.g. crosshairs in Fig. 3.1), the orientation of the molecule can be monitored by a non-resonant detection current, I_{det} (black curve). Subsequent laser shots (blue vertical lines) repeatedly inject single electrons into the LUMO, statistically triggering switching back and forth between the adsorption geometries. Every switching event manifests as an abrupt change of the detection current, which is registered for each laser shot, separately for both directions (arrows).

shots is indicated by blue markers on top of the panel. When an injected electron prompts the switch to toggle, we observe a sudden jump in I_{det}, allowing us to register every switching event with excellent fidelity. The rise time of the signal stems from the bandwidth of the STM current preamplifier. We adapt the repetition rate of the pulse train to be able to clearly distinguish every switching event.

From the in-gap images, we know which amplitudes $I_{|l\rangle}$ and $I_{|r\rangle}$ of the detection current indicate that the switch is in state $|l\rangle$ or $|r\rangle$, respectively. Hence, we can discriminate in which direction any switching reaction occurs (arrows in Fig. 3.6b). Counting all events in such a time trace allows us to determine the switching probability per terahertz pulse, separately for both directions: $p_{\mathrm{l\text{-}r}}$ from $|l\rangle$ to $|r\rangle$ and $p_{\mathrm{r\text{-}l}}$ from $|r\rangle$ to $|l\rangle$.

This detection scheme is based on so-called action spectroscopy[41], which we extend with well-defined single-electron injection. Since we deliberately confine these tunnel events to time scales faster than a field cycle of light, we denote the new technique as ultrafast action spectroscopy.

In order to resolve the switching statistics with high precision, we repeat all

subsequent experiments numerous times such that we observe a sufficient number of events. The error margin achieved in this way will be discussed quantitatively below based on a time-resolved experiment.

With this statistical detection scheme, we are in principle prepared to observe how femtosecond atomic forces affect the reactivity of the switch. To be able to interpret the forces' impact, however, first of all, we will now characterize the detection mechanism in the absence of force pulses in more detail.

Spatial variation of the switching probability. Interestingly $p_{\text{l-r}}$ and $p_{\text{r-l}}$ depend on the lateral position (x, y) of the tip, i. e. the location where electron injection takes place. We repeatedly apply terahertz pulses tuned to the LUMO resonance as an electronic trigger (c. f. Fig. 3.6a). From thousands of time traces acquired at different tip coordinates, we obtain spatial maps of the local switching probabilities $p_{\text{l-r}}(x, y)$ and $p_{\text{r-l}}(x, y)$ as shown in Fig. 3.7a and b.

The maps unveil rich sub-molecular details and a marked direction dependence. For both directions, we find eight regions with a locally enhanced switching rate, highlighted by dashed circles. Pixels where switching cannot be detected are shown in white. Every other local maximum appears slightly pronounced. Their positions align with the axes of the molecule in the initial state, which are indicated with dashed lines.

Strikingly, this pattern strongly resembles the LUMO density in the respective initial states. Figure 3.8 shows calculated maps of the efficiency of local electron injection into the LUMO in both ground states $|l\rangle$ and $|r\rangle$. According to equation (2.4), we calculated these maps from the overlap integral between an s-wave of the tip and the LUMO density $\psi_{\text{LUMO}}(x, y)$, which we obtained from a DFT calculation. Similar to the experimental data, these maps feature eight local maxima. Also here, every other lobe is more prominent, which stems from an internal torsion of the molecule as the calculation reveals. Orbital nodes structure the maps. They are aligned with the axes of the molecule (dashed lines), reflecting the in-plane orientation upon adsorption in either ground state, $|l\rangle$ and $|r\rangle$.

Altogether, the measured patterns of local switching probability $p_{\text{l-r}}(x, y)$ and $p_{\text{r-l}}(x, y)$ are traced very accurately by the calculated probability of electron injection in the respective initial states $|l\rangle$ and $|r\rangle$. In other words, the spatial variation of

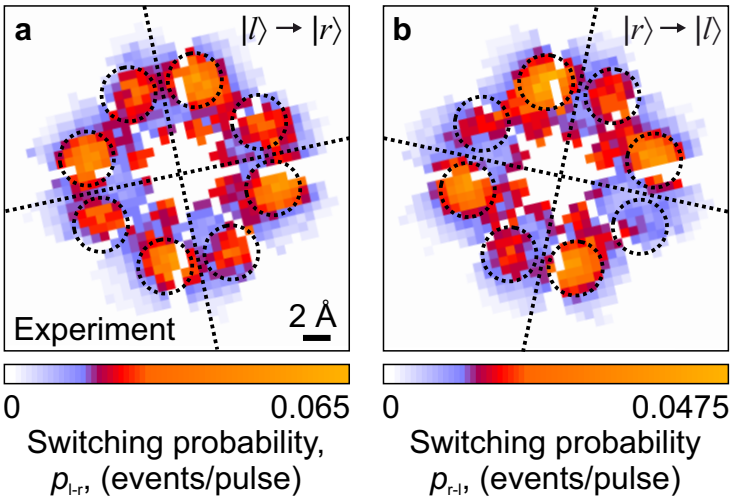

Figure 3.7 | Path-selective maps of locally tunnel-driven switching probability. Spatial maps of the switching probabilities for both directions, $p_{\text{l-r}}$ from $|l\rangle$ to $|r\rangle$ (**a**) and $p_{\text{r-l}}$ from $|r\rangle$ to $|l\rangle$ (**b**) reveal a pronounced sub-molecular structure and a clear direction dependence. Pixels where switching cannot be detected are depicted in white. In both maps, eight areas of enhanced switching probability stand out (dashed circles), four of which are more prominent in each case. The axes of the molecule in its respective initial state are indicated by dashed lines.

$p_{\text{l-r}}(x, y)$ and $p_{\text{r-l}}(x, y)$ is predominantly determined by the local efficiency of electron injection. On the other hand, this linear dependence between local tunnel rate and switching rate per light pulse means the following: Given an electron has tunneled into the LUMO, the probability that the molecule switches is approximately constant, irrespective of the coordinate of electron injection. The following experiment supports this observation even quantitatively.

Quantitative effect induced by one tunneled electron. We position the tip on a fixed lateral spot (x_0, y_0) where switching can be triggered efficiently. Now we vary the tip height z and record two quantities separately. First, we measure the lightwave-driven tunneling current through the LUMO as described in chapter 2. When we calibrate this current, $I_{\text{THz}}(z)$, in units of electrons per pulse, we directly obtain the probability that a single lightwave prompts an electron injection. This tunneling probability $I_{\text{THz}}(z)$ is drawn as blue data points in Fig. 3.9a. The relative height $z = 0\,\text{Å}$ is defined by an arbitrarily chosen current setpoint in time-integrated

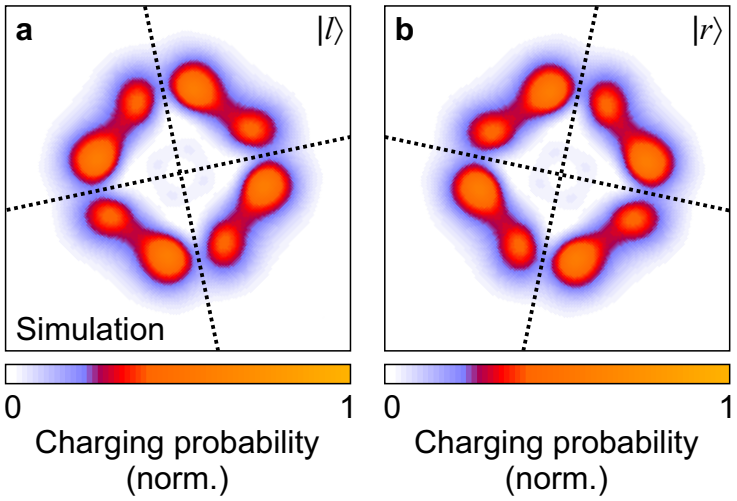

Figure 3.8 | Calculated local charging probability. The local probability of electron injection into a LUMO is simulated as the square of the respective overlap integrals between tip and orbital electronic wave function for both adsorption geometries $|l\rangle$ (**a**) and $|r\rangle$ (**b**). We approximate the tip as an s-wave with a decay length of 0.6 Å and find the best agreement between this simulation and the maps of local switching probability (Fig. 3.7) when the tip wavefunction is centered 9 Å above the top-most NaCl layer.

STM (see caption). Negative values of z describe the tip approaching the molecule.

We find that the tunnel probability decays exponentially with increasing tip-molecule distance. This behavior is typical for STM tunneling and derives from the fact that the quantum mechanical wavefunctions of bound electron states decay exponentially in vacuum. At increasing distance between tip and molecule, the overlap integral in equation (2.4), and therefore also the tunnel rate, trace this exponential decay.

Next we observe a different aspect of the switch. We move the tip along the same z-coordinates again while lightwaves repeatedly prompt LUMO tunneling. This time we monitor the switching behavior of the molecule via numerous time traces similar to the one shown in Fig. 3.6b. From these data we extract the switching probability per light pulse, $p(z)$, as a function of the relative tip height (red data points in Fig. 3.9a).

We find that at all tip heights, the switching probability $p(z)$ is smaller than the tunnel probability $I_{\mathrm{THz}}(z)$. This is reasonable since charging the molecule is a pre-

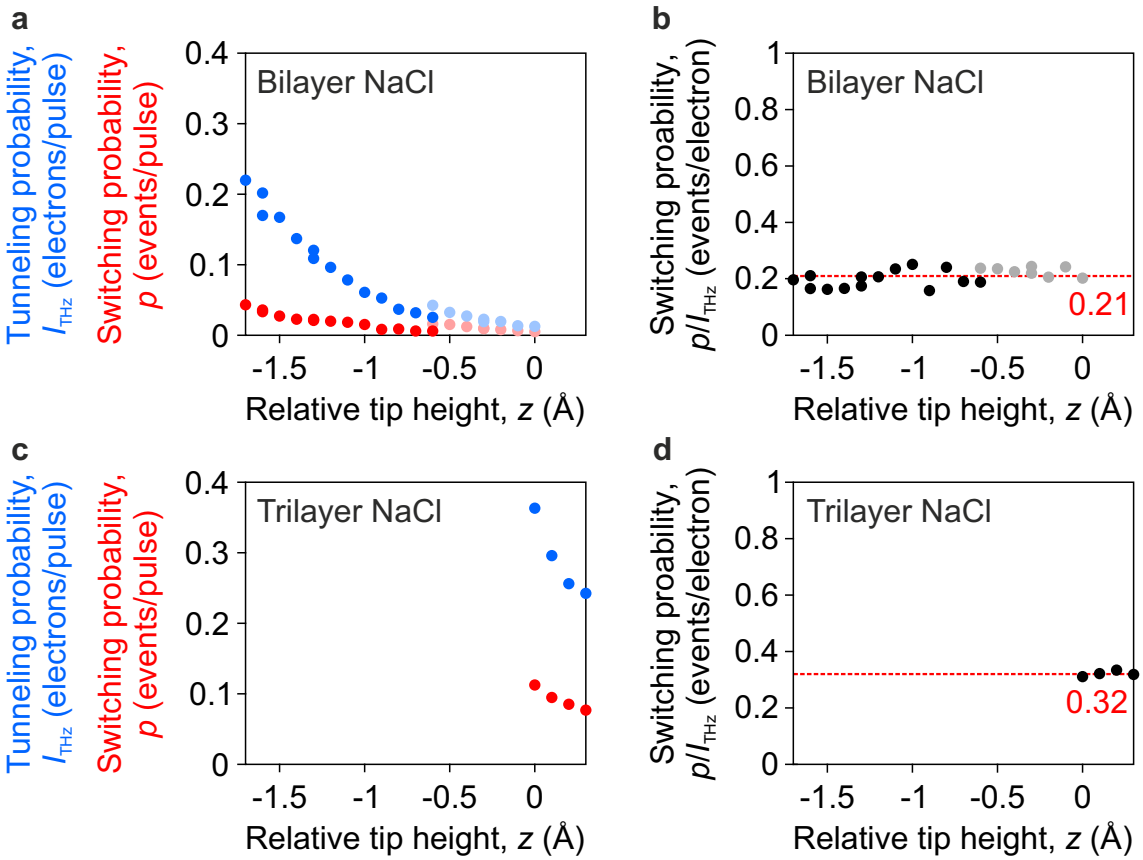

Figure 3.9 | Tunnel-induced switchability depends on charge lifetime. **a**, We position the tip on top of a MgPc molecule adsorbed on bilayer NaCl and inject LUMO-resonant probe pulses. While we keep the lateral position of the tip constant, we vary the tip height, z, and detect both the electron tunnel probability, $I_{\mathrm{THz}}(z)$, (blue data points) and the switching probability, $p(z)$, (red data points) per pulse. Both quantities decay exponentially with z. A second dataset acquired at a slightly different lateral coordinate is shown as light data points. **b**, Dividing both quantities gives the average switching probability per tunneled electron, which is approximately constant at $p/I_{\mathrm{THz}} \approx (21 \pm 3)\%$ irrespective of the tip height (red dashed line). Similar measurements of a MgPc switch adsorbed on trilayer NaCl where the charge lifetime is longer reveal a higher switching probability per injected electron of $p/I_{\mathrm{THz}} \approx (32 \pm 1)\%$ (**c**,**d**). The tip height is given relative to $z = 0$ Å at a setpoint current of 2 pA and a bias voltage of +142 mV on the bare NaCl surface. $z < 0$ describes the tip approaching the substrate. We note that the largest error contribution derives from the calibration of the tunnel current in absolute units, which is accurate up to a few percent.

requisite, but not warranty for switching. Moreover $p(z)$ decays exponentially similar to $I_{\mathrm{THz}}(z)$. We have already discovered an apparently linear connection between the charging and switching probability in the lateral maps examined above. The retraction measurements shown here support this observation, and even quantify it: Dividing the switching probability per light pulse by the tunnel probability per light pulse, we obtain the switching probability per tunneled electron $[p/I_{\mathrm{THz}}](z)$ at each tip height. The result is shown as black data points in Fig. 3.9b.

This interesting quantity provides a first insight into the dynamics of switching. To the best of our knowledge, no other experiment could possibly quantify the statistics subsequent to a single electron injection in such a single-molecule switch. Intriguingly, it appears that the outcome of an electron injection does not depend on the tip height. We find that on average, in $(21 \pm 3)\%$ of the cases where an electron charges the molecule, the subsequent dynamics result in a switching event.

Both measurements have been repeated for larger tip heights (light data points in Fig. 3.9a). These data were recorded at a slightly different lateral position on top of the molecule. In this case, both the tunnel and switching probability increased. Apparently the overlap between tip and molecular orbital wavefunction was even larger at this coordinate. The probability p/I_{THz} for the switch to toggle after electron injection, however, remained constant at approximately 21% (light data points in Fig. 3.9b). This number seems to be an inherent property of the switch, describing its dynamics independently of the position where electron injection occurs.

Influencing the switching yield statically. The value we obtained for p/I_{THz} describes that, in the majority of charging events, the switch ends up in the same state where it started from. Considering the potential landscape illustrated above, a possible way to statically enhance the switching probability after electron injection might be to increase the charge lifetime τ_{charge}. In this way, the charged molecule should have more time on average to transiently rotate towards $\phi = 0\,\mathrm{deg}$ and cross the barrier that separates $|l\rangle$ and $|r\rangle$. So far, we have examined a molecule adsorbed on a bilayer island of NaCl (Fig. 3.9a,b). The charge lifetime should amount to a few hundreds of femtoseconds in this case[96]. Now we repeat the tip retraction study on another molecule adsorbed on a trilayer island, where we expect the thicker NaCl tunnel barrier to increase τ_{charge}.

We note that the relative tip height refers to a steady-state current setpoint on the bare NaCl surface in both scenarios. Since the apparent height in STM and the geometric height of atom-scale samples are not the same, one cannot compare the tip height of bilayer and trilayer measurements in absolute numbers.

Both the tunnel and switching probability per light pulse are comparatively large in the range of tip heights that we studied on trilayer NaCl (Fig. 3.9c). Again a decay with increased tip-molecule distance manifests itself. On this trilayer island, however, the switching probability per injected electron p/I_{THz} is indeed enhanced (Fig. 3.9d). It amounts to approximately $(32 \pm 1)\%$ and appears constant irrespective of the tip height. We presume that this increased switching probability is caused by the larger charge lifetime on trilayer NaCl, which favors phase-space trajectories that switch the molecule in the statistics.

Electron injection serves as well-defined probing mechanism. These observations corroborate the overall picture drawn initially. Electron injection serves as an electronic trigger to switch the molecule. The rotation dynamics of the charged molecule are subject to the quantum probabilistic lifetime of the charge. Neither the lateral nor the vertical position of the tip seem to influence the *inherent* switching statistics. We conclude that the particular coordinate of electron injection as well as the proximity of the tip determine the tunnel probability, but do not affect dynamics and statistics of the switching process. Therefore, we can use this electronic trigger as a well-defined probing mechanism in order to interrogate a molecule that has already been excited previously.

In the next section we will see that the reaction statistics of the switch can not only be influenced statically. With a novel stimulus, we will prepare a coherent wavepacket motion to modulate the switching rates on the femtosecond time scale. This innovation gives us unprecedented control over single-molecule reactions on their intrinsic time scales: We introduce femtosecond atomic forces.

3.2 Tip-confined fields coherently control femtosecond switching dynamics

To implement femtosecond dynamic forces at atomic scales, our key idea is to exploit strong oscillating terahertz near fields at the metallic tip. If we decrease the amplitude of the terahertz pulses such that they do not access any orbital resonance, the molecule is not charged and the switching rate drops to zero. Yet there are still atomically strong local near fields oscillating at the tip apex, which could drastically interact with the molecule in principle. The following will show that these fields can indeed act as an atom-scale femtosecond force, thereby steer molecular motion, and manipulate reaction statistics with unprecedented precision and control.

Force pulses modulate the switching probability. We apply a novel pump-probe experiment (Fig. 3.10a). As will be corroborated below, the pump pulse is set to apply an ultrafast local force, $\mathbf{F}(t)$, that induces a coherent structural wavepacket motion of the molecule. A time-delayed probe pulse injects an electron into the LUMO of the excited molecule to trigger a switching reaction. Analyzing the outcome of every laser shot allows us to time-resolve the transient switching probability of the excited molecule, $p(\tau)$. Importantly, the pump pulse is tuned below any orbital resonance $V_{\mathrm{THz}}^{\mathrm{pump}} \ll V_{\mathrm{LUMO}}$ such that it does not drive electron tunneling by itself.

Fascinatingly, we find that, even so, the pump imprints a marked oscillation on $p(\tau)$ at a frequency of 0.3 THz (red data points in Fig. 3.10b). The data can be accurately described by a negative-cosine function (dashed wavy line), vertically offset by a certain baseline of switching probability. In the time window observed here, no decay of the harmonic signal is visible. A similar measurement performed with a slightly different tip position and field strength on an identical molecule (shown in reference 21) reveals that the coherent modulation can even be as strong as 39% (peak-to-peak amplitude vs. baseline).

High-precision statistics. To resolve modulations of such a percent-scale probabilistic quantity at all, we had to ensure a very high signal-to-noise ratio in the statistical measurement. Every data point in Fig. 3.10 represents statistics extracted

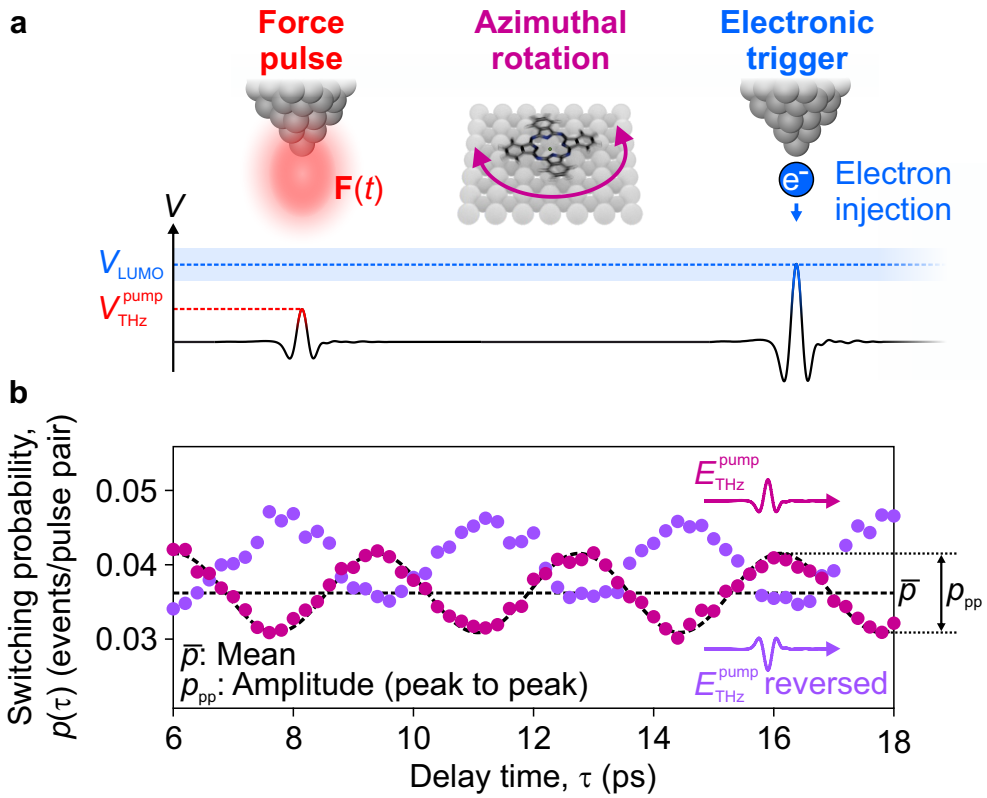

Figure 3.10 | Ultrafast force stimuli coherently control the single-molecule switching probability. a, In a pump-probe scheme, we apply sub-resonant light-waves with a tip-confined peak voltage, $V_{\mathrm{THz}}^{\mathrm{pump}}$, below any orbital resonance. The near fields can directly act as an ultrafast local force stimulus, $\mathbf{F}(t)$, driving structural dynamics, such as an azimuthal rotation of the molecular frame. With a delayed probe pulse that is tuned to the LUMO tunnel resonance, V_{LUMO}, we inject a single electron to trigger a quantum-probabilistic switching event with femtosecond definition. **b**, The switching probability per probe pulse as a function of delay time, $p(\tau)$, exhibits a prominent coherence at a frequency of 0.3 THz (ruby data points, dashed sine wave as guide to the eye). Reversing the polarity of the force pulse flips the phase of the observed coherence (purple data points). In the following, the mean of such coherent oscillations, $\overline{p}$, (dashed straight line) and their peak-to-peak amplitude, p_{pp}, are systematically analyzed.

from a time trace where a total of 249 770 pulse pairs was coupled to the STM. This sequence triggered about $np = 5760$ switching events observed in one direction. Statistically every laser shot represents a Bernoulli trial and the overall sequence follows a binomial distribution. The corresponding shot-noise limited signal-to-noise ratio is $\sqrt{np} = 76$, which describes a relative error of 1.3%. In the experiment, we observe that the oscillatory data points deviate by a relative error of 1.6% from a fitted sine function (standard deviation divided by mean).

Intriguingly, ultrafast action spectroscopy not only allows us to locally detect statistics of atom-scale femtosecond dynamics, but with a remarkable accuracy that reveals relative variations on the order of 10^{-2}. Hence the switching probability can be determined with an absolute error as small as about 10^{-4}. From a technical point of view, this precision opens experimental access to a vast range of atomistic dynamics that leave only most subtle statistical effects as a fingerprint.

Indications of the nature of the dynamics. The observed oscillation that our sub-resonant pump pulses drive exhibits a frequency typical for structural dynamics, yet the motion pattern is unclear so far. In fact, the frequency is comparable with a frustrated azimuthal rotation of the adsorbed molecule as calculated by DFT, which will be detailed further below. Also, the structural trajectory required for switching between $|l\rangle$ and $|r\rangle$ is predominantly an in-plane rotation, thus we assume that the pump pulse excites this azimuthal eigenmode. This conjecture will be supported by many observations presented in the remainder of this chapter.

Purely field-driven coherent dynamics. Moreover, the following experiments will corroborate that the way the pump pulse steers this motion is purely mediated by the ultrafast near fields, coherently acting as a localized force transient. To prove this picture, we vary the force pulse while keeping the electronic probe trigger constant. Then we observe how our modifications affect the transient switching statistics. In particular, we quantify the sinusoidal modulation of the switching probability in terms of its time-averaged mean value, $\overline{p}$, and its peak-to-peak amplitude, p_{pp} (defined in Fig. 3.10b).

In this study, it is instructive to calibrate the strength of the pump pulses in terms of the peak voltage, $V_{\mathrm{THz}}^{\mathrm{pump}}$, that they transiently apply between tip and sample. To

do so, we apply a calibration scheme which will be discussed in detail in chapter 4 of this work.

We systematically tune the amplitude of the force pulse, starting from zero, and time-resolve several pump-probe traces $p(\tau)$. In total, we measure 13 different curves where the pump pulses apply voltages $V_{\mathrm{THz}}^{\mathrm{pump}}$ ranging from 0 V to almost 1 V across the tunnel junction. Five traces out of the whole dataset are shown in Fig. 3.11a (data points). Each measurement covers one period of the 0.3 THz oscillation, from a pump-probe delay time of $\tau = 30.0$ ps to 32.8 ps. With rising amplitude of the force pulse, the pump-induced oscillation becomes more and more prominent. Sine fits to the curves are drawn as solid lines.

These data reveal that the pump has two qualitatively different effects on the switching statistics of the molecule. First, it induces a marked oscillation of the transient switching probability $p(\tau)$. Second, the pump can add a delay-independent, positive offset to $p(\tau)$. Remarkably these two components scale very differently with the pump field. From the individual sine fits to all 13 pump-probe traces, we obtain the scaling behavior including error bars (Fig. 3.11b,c).

When increasing the pump amplitude starting from 0V, the mean of the switching probability remains flat until the pump pulses access the LUMO resonance with their peak voltage (Fig. 3.11b). As soon as the pump voltage exceeds 0.7 V, $\overline{p}$ increases steeply, which we can attribute to additional switching events of the molecule caused by pump-induced LUMO tunneling. For weak pump fields below this onset, only the probe pulse triggers switching events, which leads to a constant mean switching probability of $\overline{p} \approx 0.025$. In stark contrast, the amplitude p_{pp} of the oscillations of $p(\tau)$ scales linearly with the pump field over the entire field range, starting from zero (Fig. 3.11c). Even in the regime where pump pulses are too weak to drive electron tunneling, they can severely modulate the transient switching statistics.

This behavior makes us conclude that it must be the electric field of the pump pulse itself that steers the molecule, causing the modulation amplitude p_{pp} to depend linearly on $V_{\mathrm{THz}}^{\mathrm{pump}}$. Our picture is additionally supported by another intriguing observation: We repeat the pump-probe experiment illustrated in Fig. 3.10 and again time-resolve the transient switching probability on the very same molecule under identical experimental conditions. The only difference is that this time, we reverse the polarity of the pump waveform (schematic insets in Fig. 3.10b). We find that

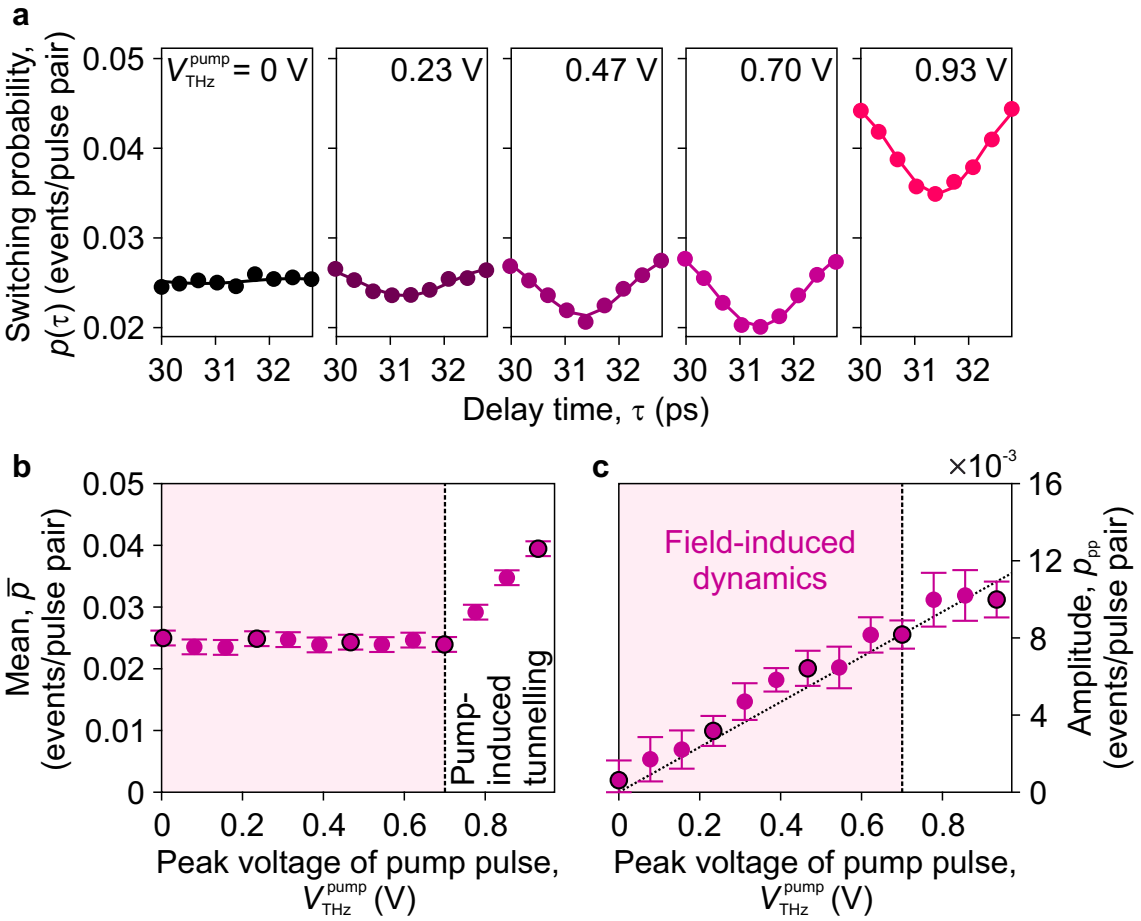

Figure 3.11 | Ultrafast near-field forces directly steer coherent dynamics. **a**, Force-driven coherent modulation of the switching probability, $p(\tau)$, for different amplitudes of the pump pulse, $V_{\mathrm{THz}}^{\mathrm{pump}}$. Mean value, $\overline{p}$, (**b**) and amplitude, p_{pp}, (**c**) of the oscillation as defined in Fig. 3.10. The data points that correspond to the five panels shown in **a** possess a black outline. Other pump-probe traces for intermediate pump amplitudes are not shown. $\overline{p}$ is approximately constant for pump pulses with a peak voltage below 0.7 V, but rises steeply at larger voltages where the pump pulse can trigger LUMO tunneling. p_{pp}, however, scales linearly with the applied waveform amplitude across the entire measured range, illustrating that the tip-confined fields can directly steer coherent dynamics, independent of electronic excitation.

$p(\tau)$ is modulated at the same frequency in this scenario, but with opposite phase (purple data points in Fig. 3.10b).

These results show that pump pulses below the tunneling threshold can imprint a coherent motion in the system directly by virtue of an ultrafast electric-field stimulus. Irrespective of the mechanism, these confined near fields must translate into a force acting locally: Whereas polar atoms or bonds will directly interact with the fields, all polarizable matter will react to the inhomogeneity of the near field.

Spatial definition of the ultrafast force. To test the local extension of the ultrafast force, we perform pump-probe experiments at different positions of the switch (Fig. 3.12). Throughout these experiments that I will discuss now, we keep $V_{\mathrm{THz}}^{\mathrm{pump}}$ just below the tunneling threshold. Evidently both $\overline{p}$ and p_{pp} vary across the molecule, but depend quite differently on the tip position. We find regions where the overall switching rate $\overline{p}$ is high, but no pump-induced modulation can be observed (Fig. 3.12a). Surprisingly, at other tip positions, less than 5 Å apart, $\overline{p}$ is comparatively low, but the force pulse induces an oscillation with a large amplitude (Fig. 3.12b). Figure 3.12c shows a schematic stick model of the molecular frame in state $|l\rangle$. Labeled crosses indicate the tip positions where the pump-probe curves shown in panels a and b were recorded.

This strong lateral variation of p_{pp} proves that the pump-induced femtosecond force acts locally, confined to the angstrom scale. Moreover, the different patterns of $\overline{p}$ and p_{pp} support the picture that our ultrafast force stimulus is independent of electronic excitation.

As $\overline{p}$ is determined by the mean efficiency of electron injection by the probe pulse, the corresponding spatial pattern follows the LUMO tunnel probability, similar to the maps illustrated in Fig. 3.7. This will also be confirmed experimentally by an ultrafast movie that I will show further below. So far, however, there is no indication of why p_{pp} would vary drastically across the molecule. It is not clear why local forces applied at certain coordinates efficiently induce a coherence in the switch, but forces applied elsewhere do not. The key question is which property of the system distinguishes these coordinates.

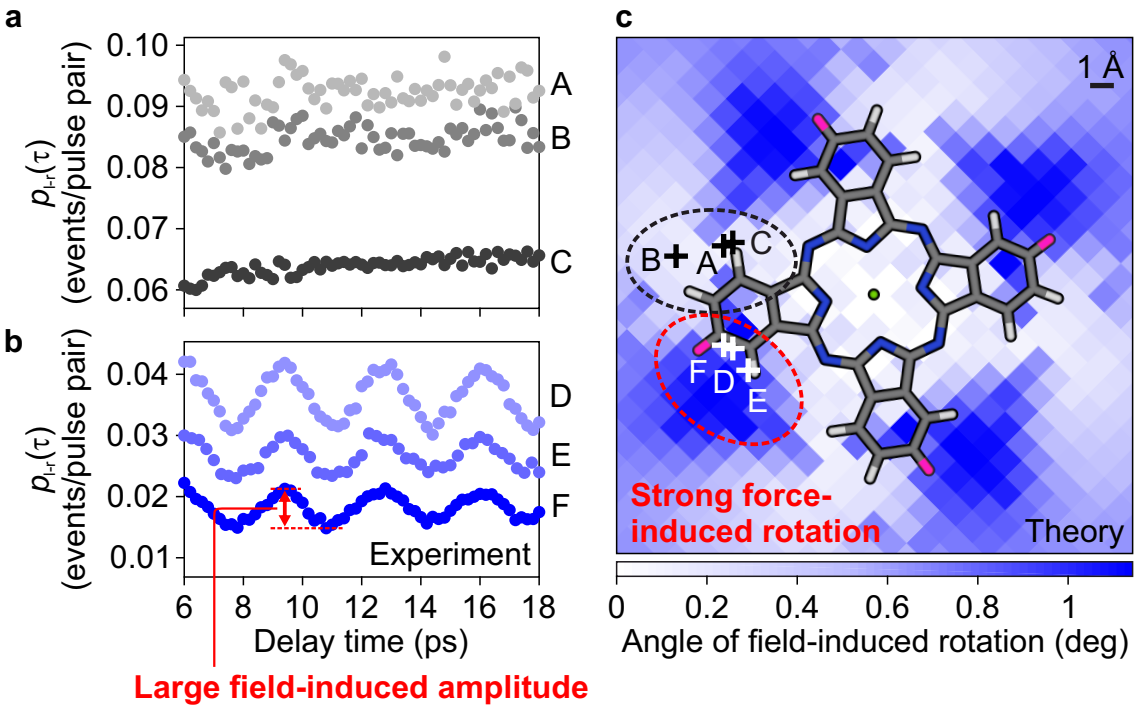

Figure 3.12 | Atom-scale spatial selectivity of the femtosecond force stimulus. **a**,**b**, Six traces of the time-resolved switching probability $p_{\text{l-r}}(\tau)$ at different tip positions (indicated by labeled crosses in **c**) reveal strong lateral variations in the amplitude of the force-induced modulation. **c**, A DFT calculation illustrates how a local out-of-plane electric field, centered at different locations across the molecule (pixel coordinates), acts as an atomic-scale force that induces an in-plane rotation of the MgPc frame. The map shows that the amplitude of the field-induced azimuthal excursion (color coded) varies strongly across the MgPc switch. A top view of the calculated geometry of the molecule in state $|l\rangle$ without applied field is overlaid with select hydrogen atoms highlighted in pink. Both experiment and theory consistently illustrate that local fields applying forces close to these atoms (region illustrated by a red dashed ellipse) induce the strongest molecular rotation and coherent dynamics. Fields applied in other regions (e.g. black dashed ellipse) hardly steer any azimuthal motion.

Effect of local fields on the in-plane rotation. Inspired by our impression that the pump-induced coherence might be an azimuthal rotation of the molecular frame, we perform a DFT study. All DFT calculations presented in this chapter have been implemented together with our collaboration partner Nikolaj Moll at IBM Zurich (Rüschlikon, Switzerland). Even though this is going to be a static simulation, it will produce insightful results that help us understand how local forces interact with the molecule. In the calculation, we incorporate local, atomically strong electric fields to simulate the effect of the pump pulses. The calculation includes the molecule and a few layers of the NaCl substrate as a single cluster. To induce external local fields, we add a pair of vertically separated point charges that enclose the molecule and substrate layers. Here, the vertical coordinate $z = 0\,\text{Å}$ denotes the position of the topmost NaCl layer, and $z > 0$ indicates the direction towards the tip.

We add a charge of $+1.6e$ at $z = +10\,\text{Å}$ above the molecule and a second charge of $-1.6e$ below the cluster at $z = -10\,\text{Å}$. e denotes the unsigned elementary charge. Both charges are located at the same lateral coordinate (x, y). Without considering any screening effects, we estimate such charge pairs to apply a vertical electric field of up to $0.5\,\text{V/Å}$ to the cluster. We keep the vertical coordinates of the point charges constant, but vary their lateral position. Hence the charge pairs generate a localized electric field, which we numerically apply at different locations of the switch.

For every position of the charges, we relax the entire geometry and analyze how the system reacts. In particular, we observe whether the external local fields cause the molecule to rotate azimuthally. Figure 3.12c illustrates the angle of field-induced azimuthal rotation of the molecular frame for every lateral coordinate of the point charges (color map in the background). Though this is a time-integrated simulation, the pattern might still give a first qualitative indication of how ultrafast local near fields prompt the molecule to rotate.

Indeed, the simulated pattern of rotational excursion agrees remarkably well with our experimental observations. In the region where the pump pulses efficiently drive a coherence of the switch (red dashed ellipse), local fields induce a strong rotation of the molecule in the calculation. Conversely, the area where we could not observe any pump-driven modulation of the switching rate (black dashed ellipse) also stands out in the simulation: Local fields applied at these coordinates hardly rotate the molecule.

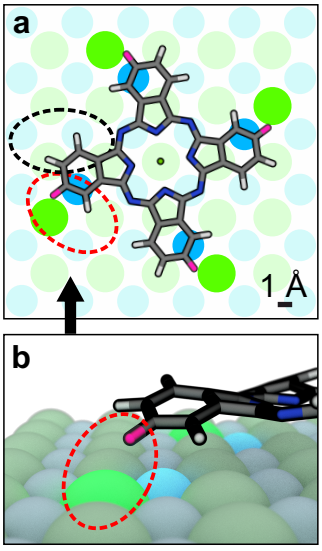

Figure 3.13 | Ground-state geometry indicates a local interaction of key atoms. a, Top view of the DFT-calculated molecular geometry in state $|l\rangle$ (stick model) including the underlying NaCl lattice (spheres). The regions where we observe efficient (red dashed ellipse) versus no (black dashed ellipse) field-induced in-plane motion as in Fig. 3.12 are marked here. **b**, Schematic side-view of the adsorption geometry, in which the z-excursion of the calculated atomic positions in MgPc is exaggerated by a factor of 6 for illustration. NaCl ions are shown as a regular cubic lattice. The geometry suggests an attractive interaction (red dashed ellipse) between specific hydrogen atoms (pink) with the underlying chlorine (intense green) and sodium atoms (intense blue), which might cause the bistable adsorption energetics. We note that these key atoms are centered in the region where we observe efficiently field-driven dynamics (red dashed ellipse in **a**).

Identification of key atoms of the bistable switch. In order to determine the physical significance of these regions, we analyze more subtle feature of the adsorption geometry. Figure 3.13 illustrates the calculated atomic positions in the ground state $|l\rangle$ without any fields applied externally. Na and Cl ions of the topmost substrate layer are drawn as spheres and the molecule is depicted as a stick model. The areas where we observe a strong versus absent response to external fields are highlighted via dashed ellipses as above.

A side-view zooming in to this region illustrates a remarkable detail of the geometry. In general, planar molecules do not bend very strongly when they are adsorbed on a flat substrate. The individual atomic coordinates usually do not change much more than a few picometers upon adsorption[a]. Specific hydrogen atoms of the adsorbed MgPc switch, however, are bent remarkably towards the substrate (sticks highlighted in pink). This deflection suggests a local polar interaction with the nearby ions of

[a] This can be rationalized by comparing variations of the typical carbon-carbon bond length in organic molecules. The most drastic difference in bond dimensions is expected when comparing single, double and triple bonds, for example. In these extremal cases of covalent character, the bonding distances vary by only a few tens of picometers[97]. Consequently, if a molecule is purely van-der-Waals bound to a substrate, the considerably weaker adsorption interactions should not deflect individual atoms within the molecule by such a drastic amount.

the underlaying NaCl lattice upon adsorption (Na atom highlighted in blue, Cl atom highlighted in green, interaction illustrated by red dashed ellipse).

We assume that this local polar interaction may play a dominant role in the overall adsorption energetics. This hypothesis could explain why local fields applied there efficiently induce structural changes of the system. In the following, a more thorough theoretical analysis will confirm this picture.

Connection between local atomic interactions and the adsorption geometry. We performed a number of DFT calculations of the switch-on-NaCl cluster that reveal how individual atoms contribute to the adsorption interaction. We start from the relaxed geometry without any external fields applied. Our intention is to see how the atoms react if we artificially rotate the molecule in-plane. To this end, we constrain the azimuthal angle to values in the range of 0 deg to 20 deg by fixing one of the in-plane coordinates of two nitrogen atoms, and then relaxing all other degrees of freedom. In particular, we want to examine whether certain atoms "interlock" in the adsorption ground states, for example at $\phi \approx +10$ deg in state $|l\rangle$, in a preferred way.

If such a local interaction occurs between atoms of molecule and substrate, forces should predominantly occur in the vertical direction. Then one might expect that, during adsorption, key atoms may deflect noticeably in z-direction, in particular because bending a planar molecule out-of-plane is generally a relatively soft degree of freedom[123]. To identify such interactions, we observe how the vertical coordinate z of different atoms responds when we force the molecule to rotate azimuthally in subsequent simulation runs.

Figures 3.14a,b show the result for a pair of atoms that are aligned almost on top of each other in state $|l\rangle$. The pair consists of a hydrogen atom of the molecule and a chloride ion of the top-most substrate layer, highlighted in pink and intense green in Fig. 3.14b. In this top-view panel, the geometry in state $|l\rangle$ is drawn, and all four equivalent pairs of atoms are highlighted. We note that these atoms are the same ones as discussed above and highlighted in Fig. 3.13b. Our previous assumption that the down-bent hydrogen atom indicates a local polar interaction with the underlying substrate is confirmed here: Panel 3.14a shows the z-coordinates[b] of this hydrogen

[b] Atomic z-coordinates are indicated relative to the average z-position of the topmost NaCl layer.

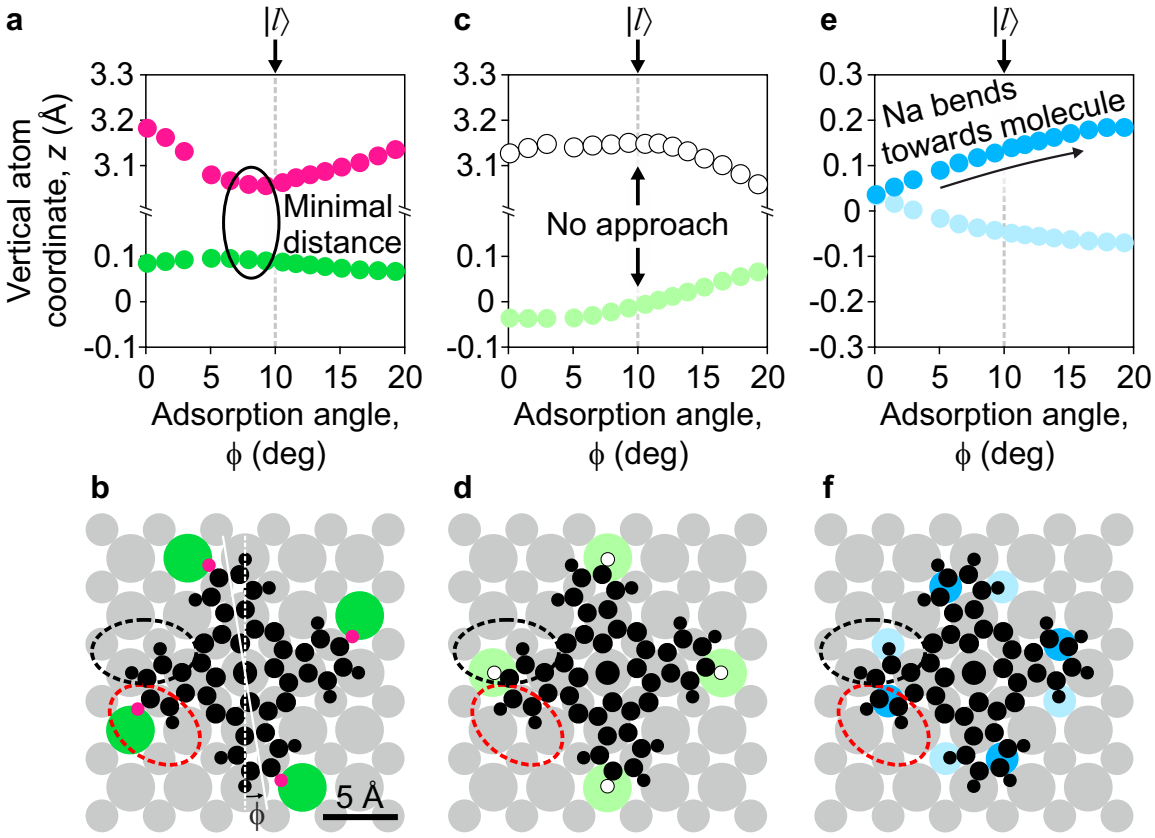

Figure 3.14 | Role of specific atoms regarding the adsorption energetics of in-plane rotational motion. DFT calculations of the adsorption geometry when the in-plane rotation of the molecule is constrained to fixed values of ϕ. **a**, Pink data points describe the z-coordinate of four equivalent hydrogen atoms of the molecule (highlighted in pink in **b**, top-view of molecule and NaCl layers) as a function of ϕ and show a clear excursion of the atoms towards the substrate for rotation angles around $\phi = 10\,\mathrm{deg}$ (z-coordinates relative to the topmost NaCl layer). Similarly, the z-coordinate of the closest Cl ion (green data points in **a** and green atoms in **b**) shows a clear upward deflection at similar angles. The vertical distance is minimal close to the ground state $|l\rangle$, suggesting a local interaction between these two atoms. **c**,**d**, In contrast, another pair of H and Cl atoms does not exhibit such behavior. **e**,**f**, The z-coordinate of four equivalent sodium atoms (intense blue) located below one of the C–C bonds of the molecule's peripheral benzene rings indicates a large excursion of up to almost 20 pm towards the molecule for increasing adsorption angles. Other sodium atoms (light blue) exhibit a vertical excursion away from the molecule. Notably, all three atoms that indicate attractive coupling when the in-plane rotation approaches ground state $|l\rangle$ are located in the lateral region where local fields induce the strongest coherent excitation (red dashed ellipses, compare Fig. 3.12 and 3.13).

atom, as well as the chloride ion beneath, upon rotation of the molecule. Remarkably, the atomic positions vary considerably in response to the rotation, in particular the hydrogen atom is deflected by more than 0.1 Å. The calculation shows that very close to the ground state at $\phi \approx +10\,\mathrm{deg}$ (dashed line in panel 3.14a), this pair of atoms aligns at a minimal distance, which marks a fingerprint of a local attractive interaction.

Moreover, this appears to be a unique local interaction, and not just simple electrostatic attraction as one would encounter between any pair of polar hydrogen and chlorine atoms. Comparing another pair of atoms supports this idea (Fig. 3.14c,d). The hydrogen atom on the other side of the isoindole unit is located on top of another chloride ion (highlighted in white and light green in panel 3.14d). However, these atoms do not approach to minimal distance in state $|l\rangle$, but rather deflect away from each other at $\phi \approx +10\,\mathrm{deg}$ (panel 3.14c).

Further, Fig. 3.14e,f show the z-coordinate of a particular sodium atom (intense blue) located below one of the C–C bonds of the molecule's peripheral benzene rings. We observe that this atom is deflected towards the molecule by up to almost 20 pm towards increasing adsorption angles. For comparison, we plot the z-coordinate of another sodium atom (light blue) that plays an analogous role in the opposing switch position $|r\rangle$, but bends away from the molecule in state $|l\rangle$.

Altogether we have identified three atoms[c] that indicate attractive coupling upon rotation of the molecule (pink, intense green, intense blue). Our conjecture, therefore, is that these atoms are key to the delicate balance of atomistic energies that gives rise to the adsorption potential landscape. Notably, all these atoms that apparently interlock in the ground state are located in a particular region of the cluster where, in the experiment, local fields induce the strongest coherent excitation of the switch (red ellipses in Fig. 3.12, 3.13 and 3.14).

We assume that local fields applied there translate into atom-scale forces that deflect the key atoms in a controlled and very distinct way, such that the molecule starts to rotate. Further DFT calculations confirm this picture and shed light on the microscopic mechanism by which the rotational mode is excited, which I will present in the next section.

[c] not counting equivalents due to rotational symmetry

3.3 Femtosecond forces selectively steer key atoms

The central question in the following study is how the system reacts in detail when we apply local fields at the hot spots that we have identified. To find out, we conduct further DFT calculations where we let the entire geometry relax without restricting any degree of freedom. Then we add local out-of-plane electric fields with a field strength of about 0.5 V/Å, similar to the way presented above, and relax the cluster again. What we now extract is how the additional field affects all three cartesian coordinates, (x_i, y_i, z_i), of every single atom i of the cluster. We calculate the field-induced deflections, $(\Delta x_i, \Delta y_i, \Delta z_i) = (x_i, y_i, z_i)_{\text{field}} - (x_i, y_i, z_i)_{\text{no field}}$. Figure 3.15a illustrates the vertical displacement Δz_i of every atom when we apply local fields at a position close to the key atoms of interaction (black cross). In this top-view, all atoms of the molecule are drawn as circles with a black outline, and the atoms of the top-most NaCl layer are shown in the background as circles with a gray outline. Every atom's respective vertical deflection Δz_i is color-coded via the fill color of the circles. Red colors correspond to a field-induced deflection $\Delta z_i > 0$ towards the tip, whereas blue colors indicate atomic motion $\Delta z_i < 0$ towards the substrate.

Locality of field-induced atom deflection. Interestingly, this pattern of vertical atom displacement unveils a very local response. Considerable atomic deflections are evident only around the center of the applied fields. In this region, just a handful of atoms react very strongly to the local field-induced force. The outer part of the isoindole unit is bent up noticeably, especially the out-most hydrogen atoms deflect by more than 0.5 Å. Also the ions underneath are strongly polarized in this region. Therefore the distance between the key hydrogen and chlorine atoms is increased substantially when the field is applied in the simulation. The key sodium atom identified above, slightly hidden behind the molecule in the panel, is also deflected considerably by almost 0.4 Å.

This region where we observe a strong response to the field-induced forces is only a few angstroms wide laterally. Further away, we observe only very weak displacements. Two of the three other isoindole units bend up a little, and the central ring consisting

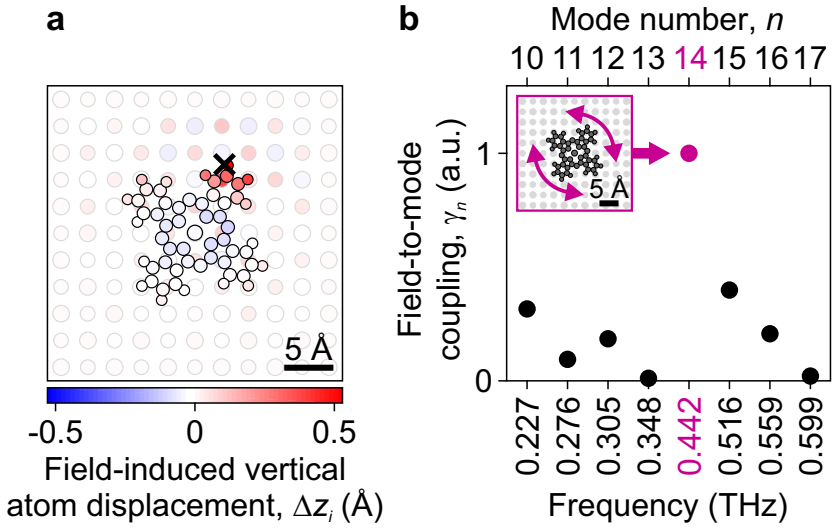

Figure 3.15 | Field-induced atom displacement couples to in-plane frustrated vibration. a, DFT simulation of how the adsorption geometry reacts to locally applied vertical electric fields with a field strength of about 0.5 V/Å, similar to Fig. 3.12c. A top-view of the molecule (circles with black outline) and top-most NaCl ions (circles with gray outline) shows the vertical deflection Δz_i of every single atom (color-coded fill of the circles) when the fields are centered close to the key atoms of local interaction identified above (black cross). Under these circumstances, the key atoms (in particular hydrogen and sodium) are affected very prominently in comparison with the overall structure. **b**, In an additional DFT simulation, we calculate all structural eigenmodes of the combined system of MgPc and NaCl layers. Then we project the full pattern of field-induced atomic displacement (**a**) onto several low-frequency eigenmodes to estimate the field-to-mode coupling γ_n for every mode n. One mode at a calculated frequency of 0.4 THz stands out, the motion pattern of which describes a frustrated azimuthal rotation of the molecule (inset).

of carbon and nitrogen atoms is slightly displaced towards the substrate. This picture shows that our femtosecond atomic forces can be applied locally, to only a handful of select atoms.

Structural eigenmode analysis. In principle, distorting the molecule and NaCl layer in such a local and asymmetric way could potentially excite many different structural eigenmodes of the system. It is hard to determine a priori which modes this pattern may couple to efficiently. To find out, we perform another DFT calculation where we start with the freely relaxed geometry of the cluster without external fields,

and subsequently, we diagonalize the Hessian matrix of the entire system. This gives us an approximate picture of all vibrational eigenmodes together with their energies and, thereby, frequencies. Particularly, this calculation also provides the patterns of motion for all modes. In the following, we label the oscillatory amplitude (including sign) of atom i in mode n, in cartesian coordinates, as $(\Delta\widetilde{x}_{i,n}, \Delta\widetilde{y}_{i,n}, \Delta\widetilde{z}_{i,n})$.

We note that boundary effects in this finite cluster might give rise to unphysical modes that would not exist when considering the complete physical system. As an example, we expect that this calculation includes twisting and shearing modes of the finite NaCl segment, which are actually inhibited when this layer is part of an extended crystal. Moreover, the interactions relevant for low-energy modes in the terahertz range include van-der-Waals and small local polar contributions. Describing such few-meV interactions quantitatively is technically demanding in DFT[124,125]. Therefore we do not claim that the vibrational energies we obtain were perfectly accurate. Without a more detailed theoretical analysis we find it even challenging to give an estimation for an error bar of the frequencies. Nevertheless, the DFT analysis proves to be internally consistent as detailed below, and provides very insightful results in the following way.

Coupling between field-induced atom displacement and vibrational modes. We want to examine how efficiently the local fields may excite different eigenmodes. To this end, we project the pattern of field-induced atom displacement (Fig. 3.15a) onto the cartesian motion pattern of every single calculated mode n:

$$\gamma_n = \sum_i (\Delta x_i, \Delta y_i, \Delta z_i) \cdot (\Delta\widetilde{x}_{i,n}, \Delta\widetilde{y}_{i,n}, \Delta\widetilde{z}_{i,n}). \tag{3.1}$$

This projection γ_n gives us an estimation of the coupling strength between local field-induced forces, applied at the hot spots of the switch, and structural vibrations of the geometry. Figure 3.15b illustrates that in the frequency range below 1 THz, one particular mode stands out. We find a comparatively large field-to-mode coupling for a vibration at a calculated frequency of approximately 0.4 THz, which is in good agreement with the 0.3 THz coherence observed in the experiment. Remarkably, the spatial pattern of this eigenmode describes exactly a frustrated azimuthal rotation of the molecule, corroborating our assumptions made above.

Degree of selective control. All the observations together draw a self-consistent picture that illustrates the degree of control in our experiments. We observed that a sub-resonant pump field that leaves the electronic system in its ground state can induce a strong coherence, which modulates the molecule's switching statistics at terahertz rates. The scaling behavior and phase of the modulation reveal that the near fields of the pump pulse steer these dynamics in a linear and coherent way. We found that the switching statistics can be modulated drastically by up to 39% at a frequency of 0.3 THz, suggesting that the dynamics that we steer are a structural vibration, most likely in azimuthal direction.

Moreover, we identified local hot spots where the tip-confined near fields act most efficiently on the switch. When we calculated whether local near fields induce an azimuthal deflection of the molecule, we obtained a similar pattern describing the same hot spots. The simulated atomic geometry revealed the distinguishing characteristic of these regions: They describe the positions where, in its ground state, the molecule interlocks with the substrate by a local polar interaction between single atoms and ions.

Our conjecture that local fields could perturb these interactions and thereby steer azimuthal motion are confirmed by further calculations: We found that our local fields deflect only a few key atoms of the switch. Calculating all eigenmodes of the system showed that this field-induced, highly localized pattern of motion couples most efficiently to an azimuthal vibration. Not only is the calculated frequency of this vibration in agreement with the coherence observed in the experiment. Also, both the calculated hot spots of azimuthal excursion and the projected main eigenmode confirm our picture: Local fields can exert atom-scale forces on key atoms of the switch, loosening its interlock with the substrate by a particular and well-defined pattern of atomic motion. In this way, our ultrafast forces controllably steer molecular motion along a select degree of freedom, providing us with unprecedented coherent control of a single-molecule functional device.

Femtosecond reaction videography. This overall picture, and in particular the local definition of the atom-scale force, are impressively confirmed in a molecular movie of the switchability. To this end, we performed pump-probe experiments as above where the pump pulse was tuned to exert local forces, but not tunnel electrons.

Then we varied both the lateral tip position (x, y) across the molecule as well as the delay time τ and resolved the switching probability, $p(x, y, \tau)$, in both space and time.

The technical challenge here is to cover this three-dimensional parameter space (x, y, τ) with spatio-temporal increments fine enough to resolve both sub-molecular details and oscillatory dynamics. At the same time, the maximum overall measurement time is limited to approximately 48 h by the capacity of the cryostats. We solved this issue by making use of the symmetry of the system, which allowed us to restrict the parameter space and avoid to measure any redundant data: Along the time axis, we detected about one period of the 0.3 THz vibration, covering delay times from $\tau = 15$ ps to 18 ps. In real space, we probed only a fraction of the molecule, i. e. a pizza-slice shaped region that covers 1/8 of the molecule's azimuthal extent. The remaining 7/8 of the area were deduced from the measured data by mirroring equivalent positions. To obtain less granular images, the individual frames of the movie have been interpolated onto a finer cartesian spatial grid.

The resulting frames of the switching probability $p_{\text{l-r}}(x, y, \tau)$ from state $|l\rangle$ to state $|r\rangle$ are shown in Fig. 3.16a. The top row of the panel displays the individual, full snapshot images of transient switching probability, for increasing delay time from left to right. In the overall picture, all frames exhibit similar features reminiscent of the maps of switching probability in the absence of an excitation force, which were presented earlier in Fig. 3.7: Four pairs of regions with locally increased switching rate are aligned around the molecular isoindole axes (dashed lines in Fig. 3.16a). Every other lobe is more prominent, which stems from the internal torsion of the molecule in the adsorption ground state. In the bottom row of the panel, zoomed-in views of the individual frames detail one pair of lobes. The regions with maximum switching rate (labeled A) are located beside the molecular axes in clockwise direction, and the less prominent regions in counterclockwise direction (labeled B).

Interestingly, when we analyze how the switching rate changes from frame to frame with increasing delay time, the two regions show a qualitatively different behavior. While region A retains an approximately constant rate throughout all delay times, region B reveals one period of a beating pattern. We confirm this observation by extracting the spatial average of the switching rate within these two regions separately:

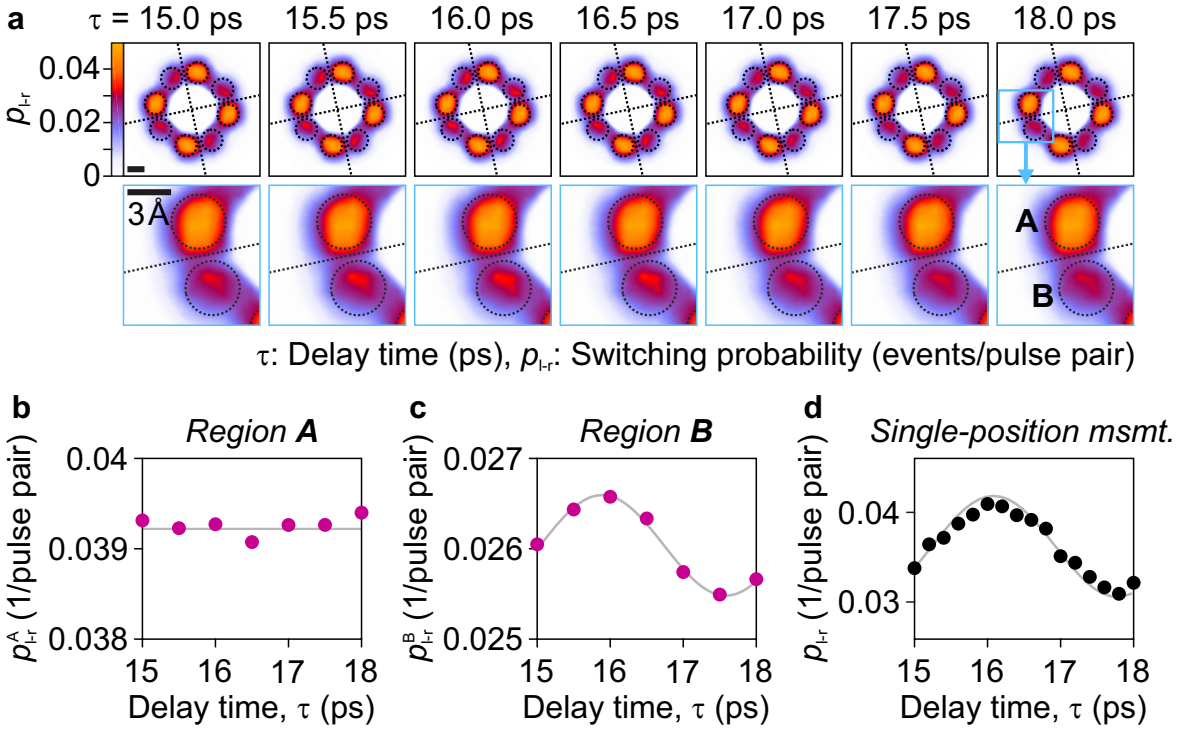

Figure 3.16 | Ultrafast movie of the single-molecule switching statistics. **a**, Snapshot images of the spatio-temporal switching probability $p_{\text{l-r}}(x, y, \tau)$ of a force-excited molecule time-resolve the reaction statistics with combined sub-molecular and sub-cycle precision. Seven snapshots of $p_{\text{l-r}}$ cover one period of the previously observed azimuthal vibration ranging from $\tau = 15\,\text{ps}$ to $18\,\text{ps}$ (top panels, guides to the eye as in Fig. 3.7). Zoomed-in detail views of each map display one pair of local maxima (bottom panels, regions A and B indicated). **b**,**c**, Time-resolved switching probabilities $p^{\text{A}}_{\text{l-r}}(\tau)$ and $p^{\text{B}}_{\text{l-r}}(\tau)$, spatially averaged over region A and B, respectively (data points). $p^{\text{A}}_{\text{l-r}}(\tau)$ indicates hardly any temporal variation (gray horizontal line as guide to the eye). In contrast, $p^{\text{B}}_{\text{l-r}}(\tau)$ exhibits the same coherent modulation observed previously in single-position measurements (data points in **d**, data from Fig. 3.10b; gray sine fits in **c** and **d** as guide to the eye). As region B is centered on the key atoms of the adsorption energetics, atomic forces applied there can efficiently steer in-plane molecular motion, in agreement with the discussed mechanism of local atomic-force control.

$$p^{\mathrm{A}}_{\mathrm{l\text{-}r}}(\tau) = \mathrm{Ar(A)}^{-1} \iint\limits_{(x,y)\in \mathrm{A}} p_{\mathrm{l\text{-}r}}(x,y,\tau)\,\mathrm{d}x\,\mathrm{d}y, \tag{3.2}$$

where Ar(A) denotes the area of region A, and $p^{\mathrm{B}}_{\mathrm{l\text{-}r}}(\tau)$ analogously. The quantities are shown in Fig. 3.16b,c. Indeed, region A reveals a rather large and approximately constant switching probability (gray horizontal line as guide to the eye). The values in region B, however, clearly describe one period of a harmonic oscillation.

To put this into perspective, we compare the data to the coherent modulation that we measured at a single tip position, as presented above in Fig. 3.10. Panel 3.16d shows a part of the same data again, restricted to the delay time window which is resolved by the movie. Sinusoidal fits are drawn in panels 3.16c,d (gray lines). It is evident that both the single-position measurement and the movie observe the same 0.3 THz oscillation. In addition, the movie demonstrates the spatial extent of the force. When the tip is positioned in B, the local forces can efficiently drive the azimuthal rotation of the molecule. With the tip in A, however, no force-induced modulation manifests. This observation is in perfect agreement with all considerations detailed above: The hot-spots of molecule-substrate interaction that we identified are located precisely in the vicinity of region B. Consequently, local forces applied there (B) can efficiently induce the azimuthal vibration of the molecule, whereas forces applied elsewhere (A) hardly do.

○

This movie impressively demonstrates the degree of coherent control that we obtain with local dynamical forces. By addressing key atoms of a bistable single-molecule switch, we can controllably steer a select rotational mode that drastically modulates the switching probability on the femtosecond scale.

We hope that this novel approach will allow future experiments to choreograph a chemical reaction between individual molecules, and resolve the electronic and structural dynamics in statistical femtosecond movies.

4 Quantitative sampling of atomic-scale near-field waveforms

Nano-confinement of light has opened new avenues across scientific disciplines. Custom nanoantennas[64–66,126], nanoparticles[127], nanogaps[67,68,128], and tips[70,71,74] have been used to concentrate electromagnetic waves down to extremely sub-wavelength scales. This toolkit has introduced new prospects in biochemical sensing[129], light harvesting[129], lightwave electronics[20,23–25,69–71,74], nanoimaging[16,20,23–25,76] and spectroscopy[16,40,76,130], even down to sub-molecular resolution[20,109] as also illustrated by this work.

To tailor such crucial applications of nanooptics, having a detailed picture of the confined electromagnetic waveforms is vital. With this goal, a given nanostructure's coupling efficiency, plasmonic propagation and near-field screening as well as geometrical phase retardation could in principle be described by classical electrodynamics. *Atomically* confined fields, however, will also depend on angstrom-scale details of the geometry[128], and can even be strongly influenced by quantum-mechanical effects[43,44]. In particular, atom-scale light-matter interaction depends critically on the absolute field strength and the precise time evolution of the carrier near field, both of which may be severely affected by quantum dynamics, such as tunneling. This currently renders a priori predictions of atomically confined near-field waveforms impossible.

Meanwhile, the ability to map out the optical carrier wave of light as it oscillates, directly in the time domain, has prompted a vivid field of research exploring light-matter dynamics faster than one cycle of light[5,20,21,29–35,70,71,74]. Electro-optic sampling and streaking techniques now routinely resolve electro-magnetic waveforms

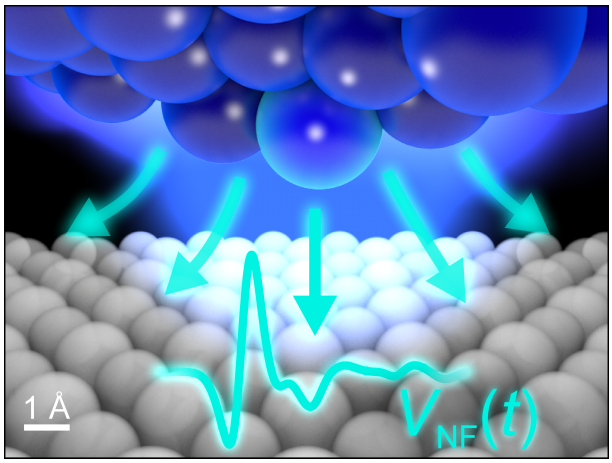

Figure 4.1 | Schematic STM near-field waveform. When light is coupled to an STM tip (blue glow), strongly enhanced near fields (turquoise arrows) oscillate between the atoms of the tip apex (top spheres) and the substrate (bottom spheres), giving rise to an ultrafast voltage, $V_{\mathrm{NF}}(t)$. The amplitude and temporal evolution of the near field (turquoise waveform) may be strongly influenced by quantum light-matter dynamics at the atomic scale.

by stroboscopically scanning them with a short gate pulse. Combining this technique with near-field microscopy[16,76] allows detection of local near-field waveforms with combined 10 nm spatial and subcycle temporal resolution. Sophisticated nanostructures have further confined light to even smaller volumes below the skin depth of metals[68,69,126]. But measuring electro-magnetic waveforms at the atomic scale, where novel non-classical dynamics have been predicted to shape local fields[43,44], has remained extremely challenging.

Lightwave-driven electron emission from sharp metal tips[70,71,74] has accessed complex electron dynamics including interfering trajectories, quiver motion and interferometric backscattering. But the interaction of lightwaves and electrons is not rigorously localized in space, hence it is challenging to fully reconstruct the near field. In lightwave STM experiments, optically gated semiconductor samples have been used to capture the transient fields in the lightwave-biased STM junction[27]. Yet this scheme depends on the assumptions that the carriers relax extremely fast, and that the steady-state conductance of the semiconductor applies equally for lightwave-driven tunneling, both of which are not a priori clear. Detection of a femtosecond waveform with atomic resolution has remained an open challenge, let alone in a calibrated measurement that provides absolute field units.

In this chapter, I will introduce a novel sampling scheme in lightwave STM that resolves a *quantitative atomic near-field waveform*, for the first time (Fig. 4.1). Our

parameter-free calibration exploits a single molecule as an atom-scale voltage sensor, which allows us to directly sense the near-field waveform in the tunnel junction (section 4.1). The near-field transients we observe differ remarkably from the waveforms coupled into the STM (section 4.2). We implement a classical solution of Maxwell's equations to describe all plasmonic dynamics of the far-to-near-field transfer. While salient features of this coupling qualitatively follow classical electrodynamics, we develop a comprehensive understanding of the atom-scale light-matter dynamics that locally shape the near field with time-dependent density functional theory (section 4.3). The simulations validate our quantitative near-field calibration and confirm that operating deeply in the single-electron regime of tunneling ensures minimal back-action of the measurement process on the local fields. Our results provide the first direct access to an uncharted domain of atom-scale light-matter interaction where femtosecond waveforms are determined by local quantum dynamics.

This chapter follows the presentation in reference 22.

4.1 Interference sampling using a single-molecule voltage sensor

The experimental setup that we implement for near-field waveform sampling is similar to what was described in chapters 2 and 3. Terahertz pulses are focused onto the STM junction, where the metallic tip and substrate act as an antenna that enhances the gap-confined near field by several orders of magnitude. The oscillating electric near field, $E_{\mathrm{NF}}(t)$, translates into an ultrafast bias voltage, $V_{\mathrm{NF}}(t)$, which is transiently applied across the tunnel junction (Fig. 4.1). To map out the near-field waveform locally and quantitatively, our idea is to exploit the same single-molecule switch introduced in chapter 3 as an atomically small voltage gauge directly within the tunneling gap. The switch can be activated only if the local voltage suffices to charge the molecule via orbital tunneling. We make use of this threshold behavior to apply the molecule as a calibrated atom-scale voltage sensor. To add temporal resolution, we developed a novel interference sampling scheme that allows us to directly trace the tip-confined near-field waveform in the time domain.

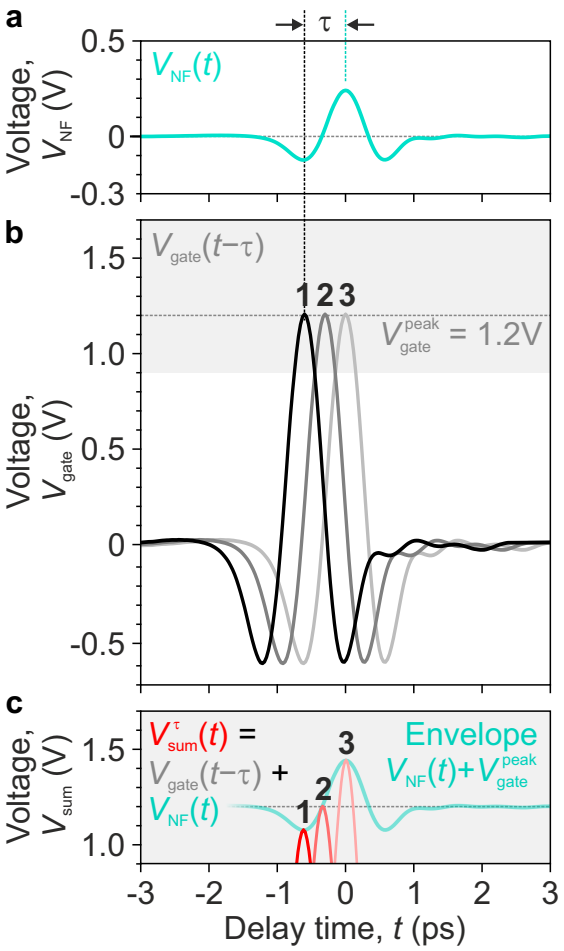

Figure 4.2 | Near-field waveform sampling by interference. We let a weak test waveform, $V_{\mathrm{NF}}(t)$, (**a**) and a delayed, comparatively strong gate waveform, $V_{\mathrm{gate}}(t-\tau)$, (**b**, labeled 1, 2, 3 for different delay times τ) interfere in the nanotip's near field. The test waveform is imprinted on the resulting sum waveforms, $V_{\mathrm{sum}}^{\tau}(t)$, (**c**, red curves labeled as in **b**) as an envelope for the sub-cycle waveform crests (turquoise curve). When the peak voltage of $V_{\mathrm{sum}}^{\tau}(t)$ is detected for different delay times τ, one can retrieve the test waveform, directly in the time domain and calibrated in absolute units of volts. All waveforms shown here are schematic to illustrate the temporal sampling scheme.

Interference waveform sampling. We superimpose the coveted test waveform (Fig. 4.2a), $V_{\mathrm{NF}}(t)$, with a delayed gate transient (Fig. 4.2b), $V_{\mathrm{gate}}(t-\tau)$. As the near fields are a priori unknown, we illustrate our sampling concept via schematic transients (Fig. 4.2 and 4.3) and note upfront that the working principle of the technique does not depend on the precise shape of the waveforms. We only require that the gate transient contains only one single prominent half cycle. In our experiment, the pulse pairs are generated in a Michelson interferometer, hence both waveforms possess the same shape. In the linear regime of field enhancement, this holds true for the respective near-field waveforms as well.

We tune the amplitude of the gate pulse much larger than that of the test waveform (factor 5 in Fig. 4.2). Hence, when the two pulses interfere, the sum waveform is mostly determined by the gate pulse. Evidently the waveform crest of $V_{\mathrm{gate}}(t-\tau)$ is

much shorter than the oscillatory period – or even any temporal feature – of $V_{\mathrm{NF}}(t)$. As a result, upon interference, this peak value is essentially offset by the instantaneous amplitude of the test waveform, $V_{\mathrm{NF}}(\tau)$. When the delay time, τ, is now varied, the peak of the sum waveforms, $V_{\mathrm{sum}}^{\tau}(t) = V_{\mathrm{gate}}(t-\tau) + V_{\mathrm{NF}}(t)$, directly traces the test waveform in the time domain. Figure 4.2c shows the peak crest of V_{sum}^{τ} for different delay times τ. The envelope of these field crests (turquoise curve) describes precisely the test waveform $V_{\mathrm{NF}}(t)$, which is to be detected. Hence, if we develop a way to retrieve the tip-confined peak voltage, V^{peak}, of a given waveform, we can vary τ to directly trace this envelope, and thereby obtain the near-field waveform $V_{\mathrm{NF}}(t)$.

Local peak-voltage detection via a single molecule. We include a MgPc switch in the tunnel junction. As introduced in chapter 3, we can use a non-resonant detection current to monitor the switching rate p, which is proportional to the rate of lightwave-driven orbital tunneling. What turns the molecule into a local voltage sensor is the well-defined relation between the applied peak voltage we seek, and the resulting lightwave-driven switching rate that we can measure.

In chapter 2 we have discussed the generic onset behavior of steady-state orbital-resonant tunneling. Here we now probe the onset of lightwave-driven LUMO tunneling in a single-pulse measurement. We gradually increase the terahertz field strength using a pair of crossed polarizers and monitor the switching rate p of the molecule (Fig. 4.3). As soon as the waveform peak V^{peak} accesses the LUMO resonance voltage (Fig. 4.3a), the switch starts to toggle. Figure 4.3b shows the monotonic onset behavior of $p(V^{\mathrm{peak}})$ (data points), which describes an error function (black curve). Its derivative (gray Gaussian curve) mimics the phonon-broadened LUMO resonance at $V_{\mathrm{LUMO}} = 1.2\,\mathrm{V}$.

This derivative $\mathrm{d}p/\mathrm{d}V^{\mathrm{peak}}$ is the ultrafast analogue of steady-state $\mathrm{d}I/\mathrm{d}V$ tunnel spectroscopy. We will support this conjecture with a quantum-mechanical ab initio calculation below in section 4.3. With this connection, we superimpose the resonance curves obtained by steady-state (violet) and femtosecond (gray) spectroscopy to calibrate the tip-confined peak voltage V^{peak} directly in units of volts (vertical axis in Fig. 4.3b).

We are now set to detect the peak voltage of any similarly shaped waveform. In particular, we can implement our interference sampling scheme as illustrated

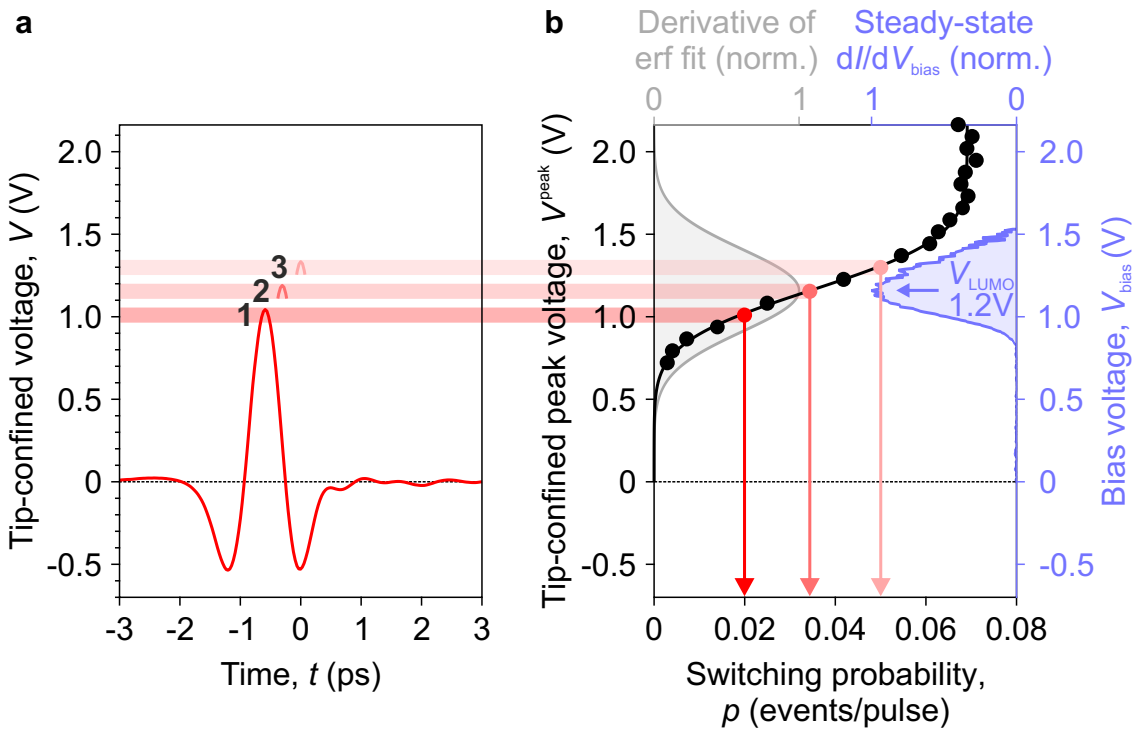

Figure 4.3 | Quantitative single-molecule peak-voltage sensor. A MgPc single-molecule switch as introduced in chapter 3 is used as an atomic-scale voltage probe. When the local peak voltage accesses an orbital resonance, electron tunneling statistically induces switching events. Due to the phonon-broadened linewidth of the tunnel resonance (c. f. Fig. 2.15a), waveforms with different peak voltages (**a**, labeled 1, 2, 3) induce different tunnel rates, such that the resulting switching probability, p, directly encodes the localized peak voltage, V^{peak} (**b**, data points). This calibration curve describes an error function (black line), the derivative of which ($\mathrm{d}p/\mathrm{d}V^{\mathrm{peak}}$, gray Gaussian curve) represents the ultrafast analogue of steady-state $\mathrm{d}I/\mathrm{d}V_{\mathrm{bias}}$-spectroscopy (violet curve). The latter determines the LUMO resonance to be centered at $V_{\mathrm{bias}} = +1.2\,\mathrm{V}$ (right vertical axis). Comparing the two resonance peaks allows us to gauge the calibration curve (left vertical axis) such that we can quantify the tip-confined peak voltage directly in units of volts without any free parameter.

above and apply any of the sum waveforms V_{sum}^{τ} (Fig. 4.2c). When we detect the lightwave-driven switching rate $p(\tau)$, we can now use the inverted onset $V^{\mathrm{peak}}(p)$ as a calibration curve to directly retrieve the local peak voltage of V_{sum}^{τ}, calibrated in absolute units of volts.

In the following section, I will present how we deployed this scheme to resolve the first atom-scale near-field waveform, and discuss the very distinct details of its shape and magnitude.

4.2 Near-field waveform shaped by plasmonic features

We applied the far-field waveform shown in Fig. 4.4a in our first near-field sampling experiment. This transient has been detected electro-optically outside the STM chamber. In order to retrieve the actual far-field waveform that is incident at the tunnel junction, we mimic the beam geometry that is implemented in the STM, as well as the relevant in-situ optical components, on the optical table. In particular, we realize the same focussing geometry and emulate the aperture of the STM thermal shields that clip a minor fraction of the low-frequency terahertz components. Also, the beam paths along which terahertz pulses propagate to the STM and to the electro-optic detector possess comparable path lengths, such that both beams undergo a similar amount of diffraction. We set the terahertz fields polarized vertically in the electro-optic crystal, and then detect the z-component of the electric field in the center of the mode. To abbreviate our notation, we denote this vertical component $E_{\mathrm{FF}}(t)$.

The far-field waveform that we resolve in this way is shaped cosine-like (Fig. 4.4a). It features only one prominent positive half-cycle, and two half cycles in the opposite direction with a considerably weaker amplitude only half as strong. Apart from that the waveform appears almost featureless, hardly chirped and there are virtually no trailing oscillations, indicating a smooth spectrum with almost transform-limited, flat phase. The peak field of 0.9 kV/m was chosen such that our sampling method covers the steepest region of the calibration curve (Fig. 4.3b) to maximize sensitivity. Strikingly, the near-field waveform induced by this transient looks very different.

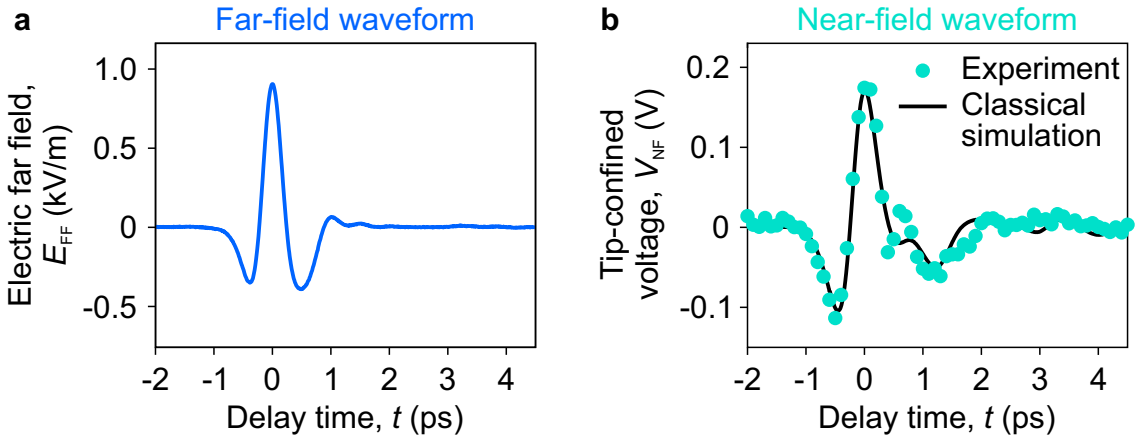

Figure 4.4 | Calibrated atomic-scale near-field waveform. a, A cosine-like far-field waveform is coupled to the tunnel junction. The transient is hardly chirped and contains no phase jumps, suggesting an almost transform-limited spectrum. **b**, The evolution of the induced near-field voltage is remarkably different (data points). This waveform exhibits a clearly different carrier-envelope phase, and subtle sub-cycle features like a kink at $t = 0.6\,\mathrm{ps}$ are resolved, indicating a more structured spectrum. A classical numerical simulation of the plasmonic coupling and propagation from the far field to the near field reproduces most of these features in detail (black line).

First atom-scale near-field waveform. Figure 4.4b displays the corresponding tip-confined near-field waveform (data points), which we obtained using the sampling scheme introduced above. We retrieved these data directly calibrated in units of volts, rendering this transient the first quantitative measurement of atom-scale femtosecond fields. Remarkably, this waveform is longer than its far-field counterpart, and possesses a different carrier-envelope phase. Sharp sub-cycle features like a kink at $t = 0.6\,\mathrm{ps}$ are clearly resolved, which suggest a slightly more structured spectrum. After a delay time of $t \approx 1\,\mathrm{ps}$ where the far-field waveform has basically vanished, in the near field, we still observe trailing dynamics. For delay times larger than $t \approx 2\,\mathrm{ps}$, however, no strong near-field oscillations remain. Apparently the geometry of our junction does not feature any long-lived mode like a sharp antenna resonance would for example. Hence we successfully avoid trailing oscillations of the near field that would compromise the sub-cycle nature of this local stimulus. This conclusion becomes clearly visible when we compare the spectra of the far-field and near-field waveform.

Far-field and near-field spectra. We obtain the spectrum, $A_{\mathrm{FF}}(f)$, of the far-field transient $E_{\mathrm{FF}}(t)$ via a Fourier transform

$$A_{\mathrm{FF}}(f) = \mathcal{F}\{E_{\mathrm{FF}}(t)\}(f) \tag{4.1}$$

and similarly for the tip-confined voltage $V_{\mathrm{NF}}(t)$. f labels the frequency. Here and in the following, $\mathcal{F}$ and $\mathcal{F}^{-1}$ denote the Fourier transform[a] and its reverse operation, respectively. The complex-valued spectra are displayed in Fig. 4.5.

The far-field amplitude (Fig. 4.5a) is centered at a frequency of 0.9 THz and possesses a spectral width of 1 THz (FWHM) that spans more than 1.6 optical octaves. Hardly any structure can be recognized in this smooth spectrum. The spectral phase (Fig. 4.5b) is almost perfectly flat at approximately 0 rad.

In contrast, the measured near-field spectrum (Fig. 4.5c, data points) peaks at a lower frequency around 0.5 THz and exhibits a subtle oscillatory structure. The near-field spectral phase (Fig. 4.5d, turquoise line) is almost as flat as that of the far field, but shifted by a CEP offset of approximately $-\pi/3$ rad. Also the phase features a slight modulation similar to the minor structure of the near-field amplitude.

In the following, we summarize the full spectral characteristics of the far-to-near-field transfer in a single transfer function. To describe this transition quantitatively, we will first discuss the relation between tip-confined electric fields and the tip-sample voltage they induce.

Local voltage and tip-confined electric fields. While our waveform sampling measurement directly samples the physical tip-sample voltage $V_{\mathrm{NF}}(t)$ in absolute units, it is insightful to consider the time-dependent electric field in the tunnel gap as well. This allows us, for example, to study the field-enhancement effect quantitatively, and describe the relation between far field and near field by dimensionless quantities. To this end, we start with the simplest description where we assume that the electric field within the tunnel gap is largely homogeneous and polarized vertically. Further below, an atom-scale ab initio quantum simulation will put these hypotheses into perspective. For now we assume that we can describe the electric near field by its

[a] Concerning the sign convention of the phase, we define the Fourier transform (omitting real-valued prefactors) as $\mathcal{F}\{f(x)\}(y) \propto \int f(x) e^{-2\pi i x y} \mathrm{d}x$, where i is the imaginary unit.

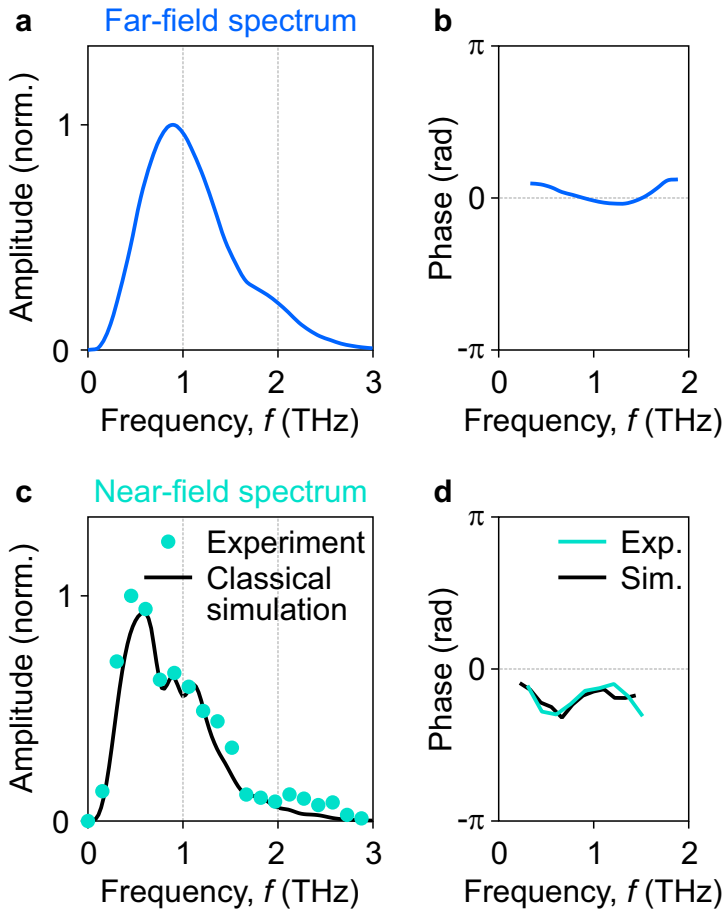

Figure 4.5 | Far-field and near-field spectra. The Fourier spectrum of the far-field waveform shown in Fig. 4.4a is centered at 0.9 THz (**a**) and possesses a flat phase of approximately 0 rad (**b**). **c**, The spectral amplitude of the induced near-field transient displayed in Fig. 4.4b, however, is shifted to lower frequencies and exhibits a minor oscillatory structure with a period of 1.3 THz (data points). **d**, A similar slight modulation is visible in the spectral phase of the near-field waveform, which is otherwise flat and shifted by approximately −1 rad with respect to the far-field phase (**b**). A classical numerical simulation reproduces most details of the near-field amplitude and phase very accurately (black lines in **c** and **d**).

z-component, which we denote $E_{\mathrm{NF}}(t)$, and which is approximately constant across the tunnel gap. Then the time-dependent near field $E_{\mathrm{NF}}(t)$ induces a linear voltage drop across the tip-sample junction. In this scenario, both the near-field and the voltage waveform $V_{\mathrm{NF}}(t)$ share the same temporal profile, and are related linearly via

$$V_{\mathrm{NF}}(t) = d \times E_{\mathrm{NF}}(t), \tag{4.2}$$

where d is the tip-sample distance. From $E_{\mathrm{NF}}(t)$ in electric-field units, we can calculate the quantitative amplitude spectrum of the electric near field

$$A_{\mathrm{NF}}(f) = \mathcal{F}\{E_{\mathrm{NF}}(t)\}(f) \tag{4.3}$$

and relate it to the far-field spectrum $A_{\mathrm{FF}}(f)$.

Transfer function. In a linear regime of electrodynamics where all spectral components are independent, one can describe the full spectral evolution of the far-to-near-field transfer by a single universal transfer function. We define the complex-valued transfer function for the field, $T_E(f)$, via

$$A_{\mathrm{NF}}(f) = T_E(f) \times A_{\mathrm{FF}}(f) \tag{4.4}$$

where $A_{\mathrm{FF}}(f)$ and $A_{\mathrm{NF}}(f)$ are the far-field and near-field spectra given in equations (4.1) and (4.3).

Figure 4.6 shows the result when we assume a gap size of $d = 10\,\text{Å}$. As a function of frequency, the absolute value of the transfer function $|T_E|$ indicates the field enhancement in the tunnel gap (data points). Its complex argument $\arg(T_E)$ (turquoise curve) describes the phase shift induced by the structure. In other words, one can directly read off from the transfer function how an oscillatory electric field of a given frequency is modified by the presence of the nanostructure. At a frequency of 1 THz, for example, incident electric fields are enhanced by a factor of almost 2×10^5 within the tunnel gap. And their oscillatory phase is shifted by approximately $-\pi/3\,\text{rad}$. The field enhancement increases steeply for low frequencies, in agreement with the typical $1/f$-like response of nanoantennas[86]. Also the order of magnitude of the field enhancement can be rationalized as follows: The far field is provided in a focus with

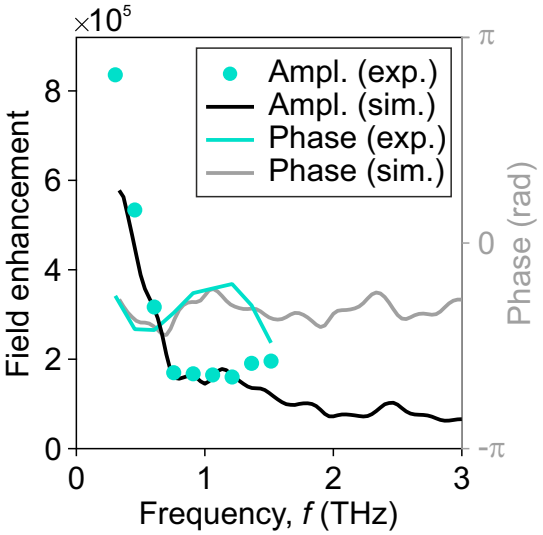

Figure 4.6 | Transfer function. The full spectral evolution of a waveform that is coupled to the tunnel junction can be summarized in a complex-valued function. Relating the near-field and far-field spectra and assuming a locally homogeneous electric field across a tip-sample distance of 10 Å yields the transfer function that visualizes the f^{-1}-like field enhancement (data points) and CEP shift of approximately $-\pi/3$ rad (turquoise curve). A classical electrodynamic simulation reproduces these results including fine details (black and gray curve).

a diameter comparable to the terahertz wavelength ($\approx 10^{-4}$ m). The nanostructure couples the electromagnetic potentials into the tunnel gap ($\approx 10^{-9}$ m), effectively squeezing the fields by a factor of roughly 10^5 in z-direction.

Dynamics encoded in the near field. In detail, all the shown near-field data contain much finer features than discussed so far. The near-field waveform (Fig. 4.4b), for example, exhibits an interesting sequence of fast kinks and slower field dynamics subsequent to the main half cycle. And in the corresponding spectrum and transfer function, amplitude and phase seem to be connected by a slight modulation. We suppose that such subtle features of the sampled near field may accurately encode elusive details of the involved light-matter dynamics.

On the one hand, the far-to-near-field coupling must be governed by plasmonic electrodynamics. Design aspects of the geometry, such as the macroscopic tip shape or the incoupling angle, might induce peculiar features in the near-field waveform. Understanding this connection would not only allow us to advance lightwave tunnel microscopy via ideally tailored near-field waveforms. In a broader sense, we believe that quantitative measurements as introduced here will gauge nano-plasmonic simulations of local fields and thereby pave the way towards predictive design of quantitative and coherent nano-optical tools.

On the other hand, at the atomic scale, even quantum-mechanical light-matter

interaction could shape local fields. In particular, lightwave-driven currents could significantly modify near fields and lead to retardation effects via accumulating charge imbalance, as recent theoretical simulations have shown[44]. Our sampled waveforms provide the first direct access to this regime of light-matter interaction at quantum-mechanical spatio-temporal scales. We anticipate that locally detected femtosecond fields may reveal novel phenomena that can only be described by ab initio simulations of coupled light-matter quantum dynamics.

In the following, I will present a classical solution of Maxwell's equations to describe the plasmonic dynamics of the far-to-near-field transfer. Subsequently, in the next section, I will introduce a quantum-mechanical simulation of the atomic-scale light-matter interaction in lightwave STM.

Classical simulation of far-to-near-field transfer. We implement a numerical solution of Maxwell's equations to visualize how electromagnetic fields couple to the STM junction. This analysis will demonstrate which characteristics of the near-field transfer arise from classical electrodynamics.

As discussed above, expressing the electric fields in the time or frequency domain contains the same information, directly connected via Fourier transform. Describing the far-to-near-field transfer in frequency space has the benefit that we can treat each frequency separately and summarize the overall coupling in a single, universal transfer function that can be applied to any waveform. We use the commercial frequency-domain finite-element solver COMSOL Multiphysics[131] to solve Maxwell's equations for complex-valued electromagnetic fields on a discrete mesh. As a result we obtain three-dimensional maps of the amplitude and phase distributions of the electric field, $\mathbf{E}(x, y, z, f)$, for a given frequency f. Classical wave propagation, plasmonic coupling to the tip shaft, screening and localization in the angstrom-sized tip-sample gap are accounted for via the complex-valued dielectric properties of the materials used in the experiment.

The macroscopic geometry of the experimental STM junction is modeled within a cuboid simulation cell. We shape the geometry based on electron microscope images of the actual tungsten tip used in the waveform-sampling experiments (Fig. 4.7a,b). The tip is a cylindrical wire terminated with a $200\,\mu$m long etched region, as the image illustrates. This taper converges under an opening angle of $\theta = 15\,$deg towards

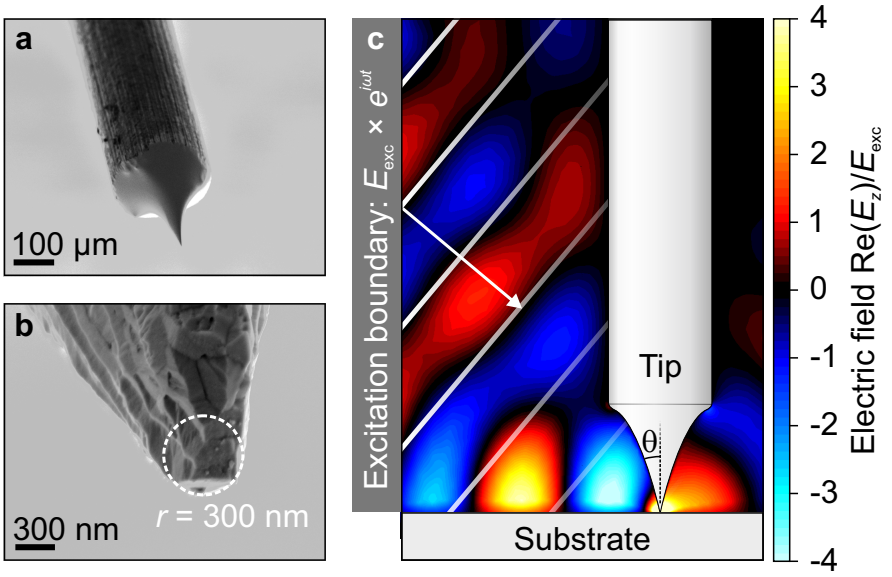

Figure 4.7 | Parameter-free classical simulation of atomic-scale near-field coupling. Electron microscope images of the tip employed in the experiments (**a**,**b**) allow accurate modeling of the macroscopic geometry of the STM junction in a classical numerical simulation (r, tip apex radius of curvature). We solve Maxwell's equations on a three-dimensional graded mesh for complex-valued electromagnetic fields of a given frequency under external excitation. **c**, A cross section of the obtained field distribution for a frequency of 1 THz visualizes the real part of the electric field component perpendicular to the substrate, E_z, (normalized to this component's excitation strength) in a color-coded map. The pattern reveals interference of the incident wavefronts with reflections off the substrate and, in the vicinity of the tip apex (θ, opening angle), plasmonic field enhancement and phase retardation effects. Analyzing the spatial field distributions for different frequencies shows that the small frequency-periodic modulation of the near-field spectrum observed in Fig. 4.5c,d stems from a resonator for surface plasmon waves formed by the etched tip geometry.

an apex with a radius of curvature of $r = 300\,\text{nm}$ (Fig. 4.7b,c). We place the tip at a height of 10 Å above a flat gold substrate. The dielectric functions of gold and tungsten are adopted from the literature[132,133]. Employing perfectly matched layers as boundary conditions avoids reflections and allows us to mimic an infinitely extended surrounding volume. The incident electromagnetic radiation is coupled into the simulation cell via oscillatory boundary conditions at one face of the volume (Fig. 4.7c). We let the beam enter as plane waves under an angle of 40 deg with respect to the substrate surface, which emulates the geometry in the STM. The

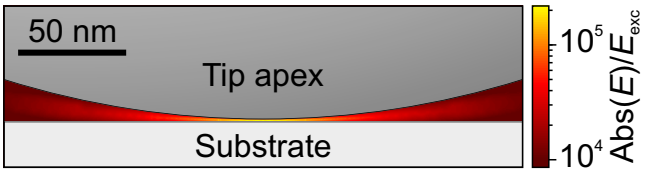

Figure 4.8 | Plasmonic field enhancement at the tip apex. At a frequency of 1 THz, incident electric fields are enhanced by a factor of 2×10^5 across the 10 Å tunnel gap.

dimensions of the simulation cell are smaller than the focal diameter of the terahertz radiation in the STM scanhead, which is 5.4 mm (intensity $1/e^2$). This corresponds to a Rayleigh length of 75 mm at a frequency of 1 THz. Therefore, exposing the 1 mm^3-scale simulation volume to plane waves as incident radiation is a reasonable approximation.

To cover length scales from millimeter wavelengths to atomically localized near fields, the volume is partitioned into a graded mesh of tetrahedrals with sizes ranging from 25 μm to 5 Å. In the vicinity of all surfaces, the grid is distributed fine enough to resolve skin depth effects. The tunnel junction contains at least two mesh points between tip and substrate. For any given frequency, a direct matrix solver computes the solutions of Maxwell's equations on the grid to a predefined tolerance level.

Figure 4.7c displays the simulated field distribution upon excitation at a frequency of 1 THz from the left-hand-side boundary. The panel color-codes the real part of the vertical electric-field component $E_z(x, y = 0\,\mathrm{mm}, z)$ across the plane that is spanned by the tip axis and the direction of incident radiation, which can be written as $y = 0$ mm. The electric field is normalized to the excitation amplitude, such that regions where the field is enhanced or decreased by the presence of the structure can be identified easily.

In the top left corner of the panel, the incident plane waves that propagate towards the junction are visible. Their profile is hardly affected by the geometry. Further towards the junction, though, the wavefronts appear transversally structured, which stems from interference with a reflection off the flat substrate. In proximity to the tip apex, the electric fields exhibit strong amplitude enhancement and phase retardation.

We find that directly in the tunnel gap, the electric field is polarized vertically. At a frequency of 1 THz, we obtain a field enhancement factor of approximately 2×10^5 at a tip-sample distance of 10 Å. Figure 4.8 illustrates how sharply the enhanced fields are confined to the tip-substrate gap.

Simulated transfer function. We analyze the calculated electric fields directly in the tunnel gap in more detail. In particular, we aim to simulate the transfer function $T_E(f)$ to describe the full spectral impact of the geometry on incident fields. To this end, we perform our simulation for a range of frequencies and extract both amplitude and phase of the gap-confined electric field. Finally, we remove artifactual diffraction with the following method: We repeat all calculations using the same simulation volume and mesh, but replace the entire geometry with vacuum. Relating both simulations with and without the tip-substrate structure allows us to extract the pure influence of the geometry on incident fields. In this way we directly obtain the transfer function $T_E(f)$, in absolute numbers, and without any free parameter. Figure 4.6 illustrates the resulting complex-valued function.

Both its amplitude (black line) and phase (gray line) agree remarkably well with the experimental transfer function. The simulated field enhancement approximately scales with the inverse frequency $1/f$, as described by antenna theory[86]. Also the absolute scale of the calculated field enhancement coincides with the experimental values, which we obtained assuming the same tip-sample distance that we chose in the simulation. The phase shift that we observe in the experiment is reproduced as well. Most surprisingly, though, even the subtle oscillatory structure of both amplitude and phase is accurately captured by the simulation.

We find that this modulation exhibits a periodicity of approximately 1.3 THz. Its origin is revealed by the spatial pattern of the field distribution. The curved part of the tip that converges towards the apex is formed by electro-chemical etching. In case of the particular tip employed here, for example, this process created a sharp edge at the circumference of the shaft where etching began, i. e. at the top edge of the curved region, as shown in Fig. 4.7a and c. This edge serves as a reflector for surface plasmon waves, such that a standing-wave pattern can form vertically across the ~200 μm large etched region of the tip. Hence we observe a periodic sequence of frequencies with slightly amplified or attenuated coupling efficiency.

Based on the simulated transfer function, we now extract a quantitative prediction of the local voltage waveform that does not rely on any free parameter.

Parameter-free quantitative simulation of local voltage. In the simulation, the tip-sample distance has been a free parameter so far. Moreover, in the experiment,

the size of the tunnel gap has not been determined. It turns out, though, that in the regime of classical electrodynamics, the local voltage transient is independent of the tip-sample distance d.

Classical antenna theory predicts that the tip-confined electric field is inversely proportional to the gap size[86],

$$E_{\mathrm{NF}}(t) \propto 1/d. \tag{4.5}$$

In the picture discussed here, we approximate the tip-sample voltage as the product of the vertical electric field in the gap times the gap size, see equation (4.2). Then the tip-sample voltage $V_{\mathrm{NF}}(t)$ is independent of d. This consideration allows us to generalize a given numerical simulation with a particular tip-sample distance d to predict the local voltage for any gap size.

So far we have described the far-to-near-field transfer with a spectral transfer function $T_E(f)$ that relates the electric fields as

$$E_{\mathrm{NF}}(t) = \mathcal{F}^{-1}\{T_E(f) \times \mathcal{F}\{E_{\mathrm{FF}}(t)\}(f)\}(t). \tag{4.6}$$

Now we define the transfer function for the local voltage, $T_V(f)$, via

$$V_{\mathrm{NF}}(t) \overset{(4.2)}{=} d \times E_{\mathrm{NF}}(t) \overset{(4.6)}{=} \mathcal{F}^{-1}\{ \underbrace{d \times T_E(f)}_{T_V(f),\ \text{independent of } d} \times \mathcal{F}\{E_{\mathrm{FF}}(t)\}(f)\}(t) \tag{4.7}$$

and note that $T_V(f)$ must be independent of d. Hence we can extract this universal transfer function from a given simulation, and apply it to predict the experimental voltage, irrespective of the actual gap size.

We built on the simulation carried out for $d = 10\,\text{Å}$, for which $T_E(f)$ is illustrated in Fig. 4.6. Then we determined the universal transfer function for the local voltage

$$T_V(f) = d \times T_E(f) \tag{4.8}$$

and applied it in equation (4.7) using the experimental far-field waveform $E_{\mathrm{FF}}(t)$. As a result, we obtained a parameter-free prediction of the local voltage waveform, which is shown in Fig. 4.4b (solid line).

Simulated voltage waveform and spectrum. The simulated waveform agrees remarkably well with the measured voltage transient. Its overall carrier-envelope phase is reproduced accurately, and the intense half cycles of the measured waveform are tracked very precisely by the simulation. Even more subtle features like the kink at a delay time of 0.6 ps are described, and the overall pulse lengths match.

Remarkably, the simulation describes the measured waveform even quantitatively. We find that the detected and simulated peak voltages differ by only 2%. This is almost surprising since several uncertainties could in principle contribute to the error bar of the simulated near-field voltage. The major ones are the applicability and accuracy of our plasmonic model at sub-nanometer length scales, and the scaling of the measured far-field waveform. This scaling was calibrated based on a power measurement of the terahertz beam, and cross-checked through electro-optic polarization rotation.

In detail, in the latter approach, the terahertz field strength in the center of the focus is directly derived from the electro-optic polarization rotation. Since the optics in the EOS setup mimic the focusing geometry within the STM chamber, this calibration should accurately describe the far-field waveform incident at the tunnel junction. From the photodiode signals A and B at a given delay time, we obtain the terahertz electric field E_{FF} as[89,134]

$$E_{\mathrm{FF}} = \sin^{-1}\left(\frac{A-B}{A+B}\right)\left(\frac{\lambda_{\mathrm{gate}}}{2\pi n_0^3 r_{41} t_{\mathrm{ZnTe}} L}\right) \tag{4.9}$$

with the wavelength of the gating beam, $\lambda_{\mathrm{gate}} = 800\,\mathrm{nm}$, refractive index of ZnTe at a wavelength of 800 nm[135], $n_0 = 2.853$, relevant electro-optic coefficient of ZnTe[134], $r_{41} = 4\,\frac{\mathrm{pm}}{\mathrm{V}}$, Fresnel transmission coefficient of ZnTe at a frequency of 1 THz[136], $t_{\mathrm{ZnTe}} = 0.48$, and the crystal length, $L = 0.5\,\mathrm{mm}$ The major uncertainty here is the electro-optic coefficient r_{41}.

We confirmed this calibration by a second method: We assumed that E_{FF} follows the shape of the waveform retrieved by electro-optic sampling, but we derived the absolute amplitude of the transient from a separate measurement. To this end, we determined the terahertz pulse energy ϵ_{THz} by measuring the beam power at a certain laser repetition rate and taking multi-reflections of the employed silicon beam splitter into account. Based on the energy density of a classical electromagnetic field, one can

relate this pulse energy to the spatial profile and temporal evolution of the terahertz beam. We assume that the terahertz beam describes a Gaussian TEM_{00} profile in the focus. σ describes the lateral distance from the beam axis where the field strength is lower by $1/e$ as compared to the center of the mode. Then the temporal evolution of the electric field in the center of the mode fulfills

$$\int_{-\infty}^{\infty} E_{\mathrm{FF}}^2(t)\mathrm{d}t = \frac{2\epsilon_{\mathrm{THz}}}{\varepsilon_0 c\pi\sigma^2} \tag{4.10}$$

where ε_0 denotes the vacuum permittivity and c the speed of light. Both calibrations agree up to 4%.

Moreover, as mentioned above, to obtain the far-field waveform incident on the tip, we had to mimic beam clipping and diffraction induced by the vacuum chamber in the electro-optic detection branch. The uncertainty of this particular step is most difficult to estimate. Altogether we recognize that, for a quantitative understanding of atom-scale near fields, a direct local measurement such as the sampling scheme introduced here is vital.

Also the simulated near-field spectrum agrees to a remarkable degree of detail with the measurement. The calculated spectral amplitude (Fig. 4.5c, solid line) precisely traces the red-shifted peak that we observed in the experiment. The slight modulation that stems from the etched region at the tip apex can be identified as well, which enables a straightforward interpretation and future improvement of the near field. Also the phase that we obtain from the plasmonic simulation (Fig. 4.5d, black line) mimics the measurement very accurately, including the CEP shift and the small periodic modulation.

Predictive design of plasmonic near-field coupling. In future experiments, we will use such simulations to optimize the tip shape and avoid edges that reflect surface plasmons. This modification should smoothen the transfer function and thereby also the near-field spectra. As a result, any trailing features of the near-field waveform subsequent to the main half cycle should be removed, which would allow us to access earlier pump-probe delay times and, hence, resolve faster dynamics. Moreover we aim to use our simulations to tailor near-field waveforms in future next-generation lightwave tunnel microscopes. When aiming for a different carrier

frequency, such as mid-infrared pulses around 30 THz, for instance, one can employ similar calculations to predict the transfer function. Then we may precondition the incident waveforms to counter-act the dispersion of the far-to-near-field transfer in order to obtain perfectly transform-limited near-field transients with an ideal carrier-envelope phase. In this way, also femtosecond atomic forces as introduced in chapter 3 may be tailored at will. We anticipate that harnessing gauged plasmonic near-field simulations for predictive design of nano-optical tools, even down to the atomic scale, will open new avenues in nanotechnology.

Influence of quantum-mechanical dynamics on atom-scale near fields. At sub-Å length scales, quantum-mechanical effects could strongly influence local dynamics and electromagnetic near fields. From a practical point of view, this regime is vastly unconquered territory for the lack of experimental access so far. We anticipate that seizing this domain of non-classical light-matter interaction, and at some point maybe even harnessing quantum-dynamical near-field phenomena ad lib., will introduce a new era in nanoscience and -technology. To this end, a thorough understanding of quantum-mechanical light-matter phenomena at combined ultrafast temporal and atomic spatial scales needs to be developed.

Previous assumptions during waveform sampling. Our scheme of waveform sampling is based on two implicit assumptions, which are a priori questionable.

First, we detect the local voltage in absolute numbers based on accessing a molecular orbital resonance. Our gauge builds on comparing the resonance curves obtained via steady-state and lightwave-driven tunnel spectroscopy. Hence we require lightwave-induced and quasi-static biasing to drive tunneling in the same way.

Second, to avoid perturbing the local waveform by the measurement, our tunneling-based detection should exhibit minimal back-action on the voltage to be measured. This requirement is however questioned due to recent theoretical simulations of light-matter interaction at atomic scales. Calculations have shown that light-driven electron tunneling can significantly affect near fields via retardation effects due to accumulated charge imbalance[44].

Given these challenges, it is somewhat surprising that the waveform we detected agrees so remarkably well with a classical simulation that does not even take the

presence of molecule into account. This calls for a thorough investigation of the influence of the ultrafast light-induced tunnel currents on the near field. To clarify the role of non-classical phenomena, we developed a full ab initio description of our experiment with time-dependent density functional theory (TDDFT).

4.3 Quantum-mechanical simulation of atom-scale light-matter interaction

State-of-the-art theoretical approaches have shed first light on a novel regime of ultrafast atomistic light-matter interaction where femtosecond near fields are determined by local quantum dynamics[43,44]. Testing such predictions, however, has been out of reach so far, for the lack of a sensor for atom-scale near-field waveforms. Our quantitative waveform detection provides the first direct access to this experimentally uncharted domain of nano-opto-electronics.

In particular, in our experimental scenario where lightwaves are coupled to an atom-scale STM junction, non-classical dynamics might already influence the local fields drastically. Hence these experiments provide an ideal first testbed at the crossover between classical electrodynamics and quantum-dynamical light-matter phenomena. In this spirit, we conducted a first-principles simulation of the quantum dynamics that occur in our lightwave-driven tunnel junction. While the calculation confirms our general picture of lightwave-steered electron tunneling, we learn that a fundamental quantum-mechanical principle distinguishes two key regimes of single-particle light-matter interaction.

This study is, to the best of our knowledge, the first to synthesize bleeding-edge approaches of both theory and experiments on quantum-mechanical light-matter interaction at extreme spatio-temporal scales. We hope that the ideas presented in this last section, and future similar studies, will pave the way towards full quantum control of atom-scale light-matter dynamics faster than a cycle of light.

Simulation geometry and technical setup. Together with our collaboration parters Franco Bonafé, Dominik Sidler, Michael Ruggenthaler and Ángel Rubio from the Max Planck Institute for the Structure and Dynamics of Matter (Hamburg, Ger-

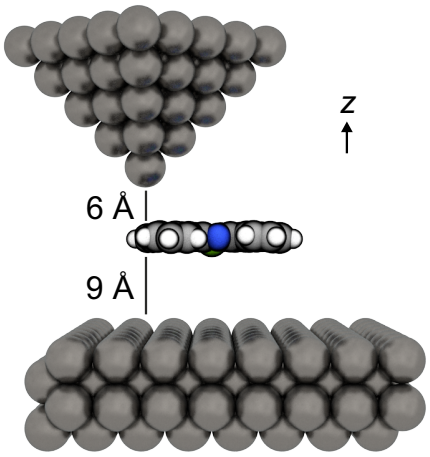

Figure 4.9 | Quantum-mechanical simulation of atomic-scale light-matter interaction. In a time-dependent DFT simulation, a tetrahedral tip (top spheres) is positioned above four layers of substrate atoms (bottom spheres). The molecule (central spheres) is placed within the junction in the same geometry as during the waveform-sampling experiments (tip apex above isoindole unit). A comparatively large vacuum gap of 9 Å decouples the molecule from the metallic substrate in the simulations, accounting for the additional experimental NaCl tunnel barrier.

many), an ab initio calculation was implemented to simulate the quantum-mechanical dynamics within the tunnel junction under external electromagnetic excitation. Figure 4.9 shows the geometric model of the simulation. We adopt the molecular structure from the DFT calculations presented in chapter 3. The tip is modeled as a tetrahedral cluster of metal atoms placed 6 Å above the molecule, and several atomic layers of a metallic substrate are included 9 Å below. This large molecule-substrate distance accounts for the tunnel barrier that the NaCl decoupling layer causes in the experiment, which we omit in the simulation to spare computational cost. We place the tip at the same lateral position that was chosen in the experiment, which is approximately on top of a phenyl H atom, as indicated by a cross in Fig. 3.15a.

The numerical calculations are performed on a real-space grid with a spatial increment of 0.4 atomic units, and time-propagated with time steps of 2.15 as. We perturb the system with an incident electric-field waveform that mimics the experimental gap-confined fields. To obtain results within a reasonable computation time and at affordable computational cost (320 cores), we squeeze the excitation waveform in the time domain and thereby scale the carrier frequency to 40 THz (photon energy of 0.17 eV). Since the atoms are clamped in our simulations, vibrational excitations are suppressed. Plasmonic modes have higher energies on the order of 1 eV. Hence our approach to approximate the experiment with a higher-frequency excitation pulse should remain accurate.

We compute the transient lightwave-driven current as well as static and dynamical

screening effects induced by the presence of the molecule, for different field strengths. The range of applied local fields is chosen such that it covers the onset of orbital-resonant tunneling, which we observe at a field strength of around 0.2 V/Å. In what follows, all local observables (electric field, current) are averaged over the whole (x, y)-plane and in a vertical region spanning 3.7 Å around the center of the molecule.

Further technical details about the simulation are elaborated in reference 22.

Outline of the theoretical analysis. In the remainder of this chapter, the results of the quantum-mechanical simulation will be presented and analyzed in two steps.

First, the influence that the presence of the molecule exerts on the local field distribution will be examined. In particular, it will be studied to which extent electron tunneling affects sub-cycle features of the near field.

Subsequently, it will be investigated whether our sampling scheme detects the transient gap voltage in a non-invasive manner, i.e. whether the two assumptions stated above are valid. It will be verified, to be specific, whether the main detection process – the onset of orbital-resonant tunneling – perturbs the local voltage to be observed.

Influence of the molecule on the local potential landscape. Our simulation describes local screening of fields by the molecule as well as electron tunneling between tip and molecule in a self-consistent way. To visualize the impact of the molecule on the gap-confined electrodynamics, we calculate snapshot maps of the local potential landscape. Figure 4.10 shows cross sections of the simulated Hartree potential at the moment where the excitation waveform peaks. Values are indicated relative to the apex potential at a time before the incident fields arrive.

When we include the molecule in the gap (Fig. 4.10a), the potential landscape and, hence, the near field distribution change drastically as compared to a bare vacuum junction (Fig. 4.10b). For example, the localized peak of the potential around the apex atom of the tip is skewed by the presence of the molecule. Also we observe that the vertical gradient of the potential within the molecule is locally reversed (Fig. 4.10c and d). To understand the sub-cycle dynamics that cause these screening effects, we follow the local electric field over time.

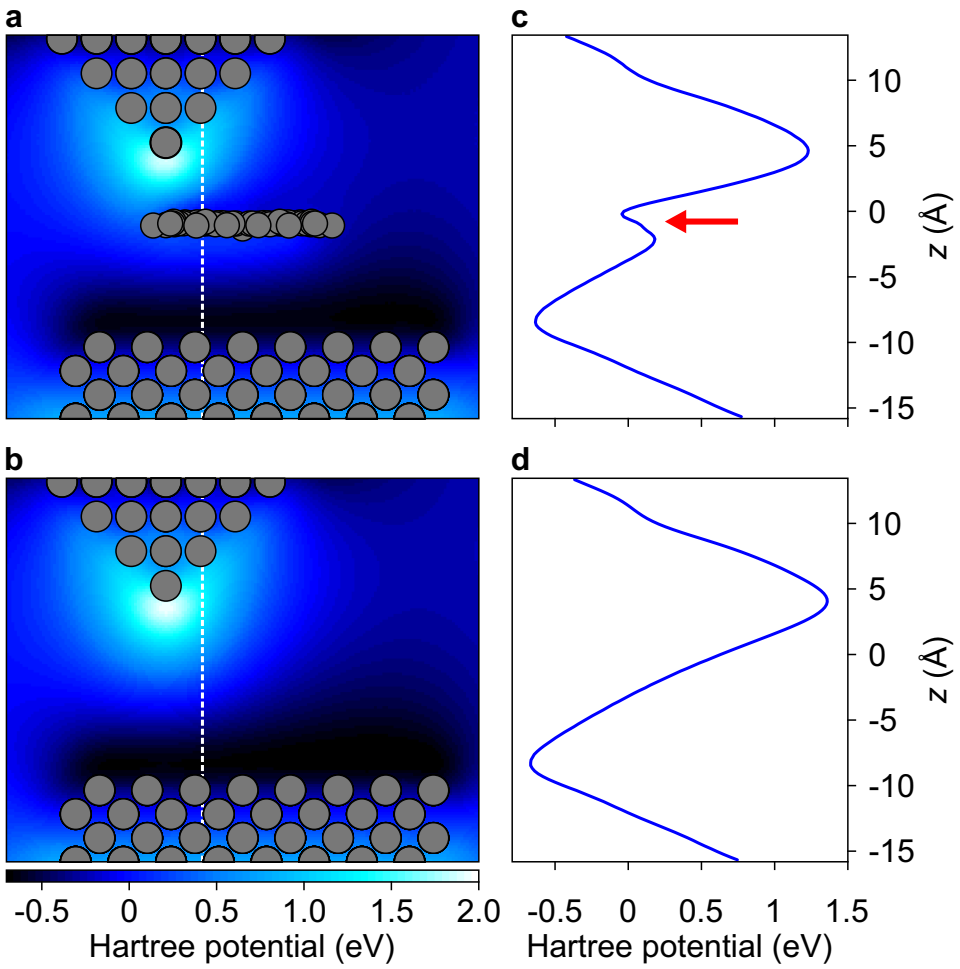

Figure 4.10 | Tip-confined potential landscape influenced by the molecule. Waveforms shaped like in the experiment excite the junction as a z-polarized field transient, in both scenarios with (**a**) and without (**b**) the MgPc molecule included. The peak field is tuned to the onset of lightwave-driven tunneling at 0.2 V/Å. Shown is a vertical cross section of the dynamical Hartree potential (relative to the apex atom at $t = -25$ fs), which reveals inhomogeneous near fields strongly localized around the front-most apex atom. Including the molecule in the junction locally alters the field distribution at angstrom scales. **c**,**d**, Line cuts through both maps (position indicated by white dashed lines in **a** and **b**) show that the vertical gradient of the potential within the molecule is locally reversed (red arrow in **c**).

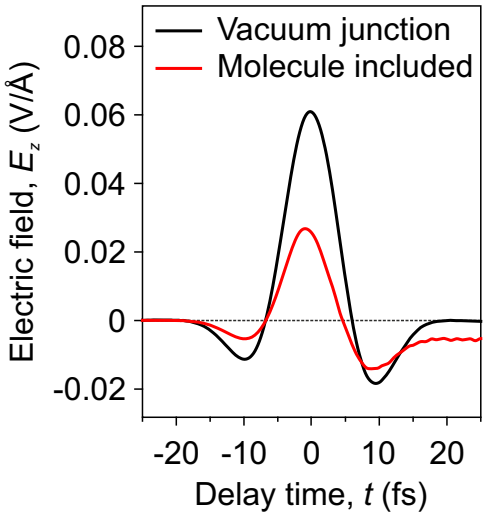

Figure 4.11 | Molecule-induced modification of the near field. We extract the vertical electric-field component, E_z, averaged across the molecular region, as a function of delay time, t. Compared to a free junction without molecule (black curve), the field transient is strongly influenced by the presence of the molecular sensor (red curve). Its peak value is decreased by a factor of two, and accumulation of tunneled charge leads to retardation effects and a trailing field offset. The peak field of the incident waveform is tuned to the onset of tunneling at 0.2 V/Å.

Tunnel-induced offset of the local field. Figure 4.11 shows the temporal evolution of the vertical electric field, averaged in the molecular region. When no molecule is present in the gap, this local field follows the incident waveform. If we include the molecule, however, the local waveform is modified strongly.

Most prominently, the overall fields are decreased by a factor of approximately two. Moreover, the molecule induces distinct sub-cycle features on the transient. While the initial, negative half-cycle is hardly affected by the molecule, the simulation shows that the most intense, positive half-cycle drives orbital tunneling, which drastically affects the subsequent fields. Charge accumulation in the molecule, together with a hole left behind in the tip, induce an electric field opposite to the waveform peak. This static component adds to the local field subsequent to the tunnel event. Hence the third half-cycle appears offset, and the second zero-crossing of the waveform is shifted to an earlier delay time, due to the presence of the molecule. Even after the excitation has faded out, the tunneled charge maintains a negative field offset.

Altogether it is apparent that the presence of the molecule has a significant impact on the local and transient field distribution. It remains to be examined whether our sampling of the gap voltage waveform is compromised by the sub-cycle lightwave-driven dynamics. In the following this will be assessed by testing the two key assumptions spelled out above.

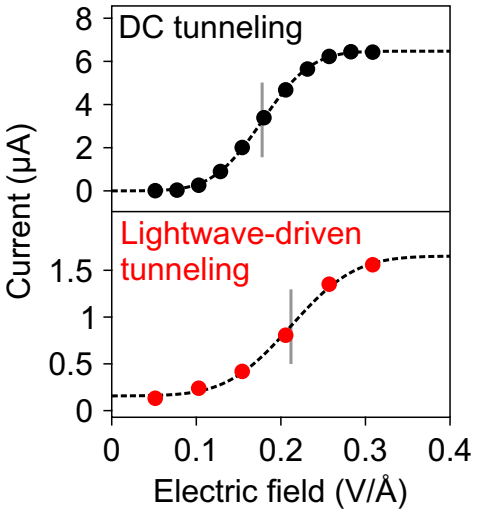

Figure 4.12 | Simulated onset of steady-state and lightwave-driven tunneling. In our near-field sampling scheme, we exploit the onset of orbital-resonant tunneling, i. e. the calibration curve Fig. 4.3b, for local voltage detection. To calibrate our single-molecule sensor, it is key whether lightwave-driven tunneling (red data points) describes a similar onset curve as steady-state spectroscopy with quasi-static biasing (black data points), which is confirmed by our TDDFT simulation. Dashed lines show error function fits as guide to the eye. Gray lines indicate the inflection points.

Assessment of the spectroscopic voltage calibration. Our waveform measurement is based on detecting the peak voltage across the tunnel gap via orbital tunneling. To yield quantitative results, the experiment relies on the conjecture that the onset of lightwave-driven LUMO tunneling occurs at a similar voltage as in steady-state spectroscopy. The first-principles simulation confirms this picture.

Figure 4.12 shows the onset behavior of the tunnel current as a function of the external field, which translates into the voltage drop across the gap. We observe a similar threshold at a field strength of around 0.2 V/Å for both lightwave and quasi-static biasing. In addition, the simulation shows that retardation effects are not strong enough to drive a significant current in the opposite direction, which could alter the onset behavior. Hence our gauge that connects lightwave-driven and quasi-static tunneling proves to be valid. The current-to-peak-voltage relation that our experiments rely on appears not compromised by sub-cycle electron tunneling. Moreover, we had not expected that the tunneling process itself differs when comparing steady-state and terahertz-driven tunneling: The Keldysh parameter $\kappa < 1$ justifies a quasistatic picture of lightwave-steered tunneling, since the tunnel event is much faster than a half cycle.

So the first of the two assumptions that our waveform detection builds on is confirmed. We conclude that, while the near field in the junction is distributed very inhomogeneously, the total voltage across the tunnel junction is probed accurately by our atomic-scale sensor.

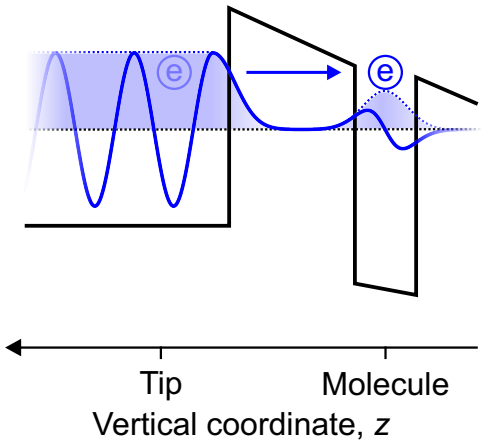

Figure 4.13 | One-electron tunneling without back-action. Schematic picture of a symbolic electron wavefunction (blue curve, dashed envelope) distributed across the potential landscape (black curve) described by tip and molecule. In the single-electron tunneling regime, the electron wave packet does not affect its own potential landscape. This fundamental quantum-mechanical principle warrants minimal back-action of our measurements on the near field itself.

Lack of electron self-interaction. The remaining issue is whether the detection process perturbs the voltage waveform to be detected. We have seen that, subsequent to a tunnel event, back-action of charges onto the near field can drastically alter local transients (Fig. 4.11). Our sampling scheme, however, senses the gap voltage by the peak-field-driven tunnel event itself, and is not sensitive to the subsequent evolution of the gap-confined fields. So the question is whether lightwave-driven tunneling perturbs the tunnel process itself.

For this matter, we consider the quantum mechanical principle that a particle does not alter its own potential. When one isolated electron tunnels through a potential barrier (Fig. 4.13), it leaves the energy landscape unchanged. At the same time, other particles or an external observer could sense the electric fields of the electron and notice altered potentials.

This distinction describes two regimes, which have to be discriminated in such experiments that involve atom-scale lightwave electronics. When less than one electron is tunneled on average per light pulse, the voltage transient that we resolve is unperturbed by the tunneling event. This is the regime in which we conducted our waveform sampling experiments. However, if more than one electron tunnels during every single lightwave, these charges might interact and severely modify the local potential landscape. In this scenario, back-action could modify the voltage waveform, and the tunnel dynamics might not even be quasi-static anymore. Moreover, in an intermediate regime of few tunneling electrons, even pulse-to-pulse quantum fluctuations might need to be considered.

○

Coherent (quantum) control at sub-cycle and atomic precision. These results conclude our initial works on lightwave-steered femtosecond tunnel microscopy, and tie all the presented studies together. The observed near fields closely follow a plasmonic model, which retrospectively confirms our initial design considerations on lightwave biasing of an STM. From this knowledge, we anticipate future studies where even the sub-cycle dynamics of lightwave-driven electron motion are examined. For example, details of the biasing waveform could influence the statistics of electron injection during one half-cycle – particularly in systems where multi-electron tunneling is possible. Local correlations could be quantified in this way, in absolute numbers and on combined atomic and ultrafast scales.

Moreover, from the precise knowledge of the gap-confined fields, coherent control can be interpreted on a sub-cycle scale. Similar to our femtosecond atomic forces, we expect strong gap-confined fields to steer sharp coherent dynamics in different systems under study. We believe that, based on accurately sampled near fields, future coherent-control mechanisms may be clearly interpreted. Also, with a predictive simulation at hand, tailoring sub-cycle control will be straightforward.

Finally, the first-principles calculation explored fundamental quantum-mechanical facets of light-matter interaction at atomic and femtosecond spatio-temporal scales. We believe that this experimental platform will directly access the limits of classical nanooptics, and immediately visualize the quantum nature of atomistic light-matter dynamics.

5 Conclusion and outlook

This work demonstrates the first femtosecond videography as well as the first ultrafast electronic and structural control at the atomic scale. Lightwave-driven low-temperature STM allowed us to track single-molecule vibrations, steer molecular reactions with atomic forces and resolve angstrom-scale near fields – all with sub-optical-cycle temporal precision, for the first time (Fig. 5.1, center). These novel experiments presented here did not only provide first moving images of elementary dynamics, such as molecular surface modes and switching reactions, directly in real space. Our observations also set the stage for a variety of exciting future studies, across the natural sciences (Fig. 5.1, periphery).

Femtosecond tunnel microscopy. We successfully applied tip-confined terahertz waveforms in STM to drive electron tunneling through a select orbital of one single molecule. This energy-selective process allowed us to trigger single-electron tunnel events with combined 0.6 Å and ~100 fs spatio-temporal accuracy. The spatial distribution of the lightwave-driven current rendered the first femtosecond snapshot of a single-molecule orbital.

At the same time, electron injection indirectly triggered a dominantly vertical vibration of the molecular frame, which we resolved in pump-probe experiments. We found that the observed dynamics encode the interaction between molecule and substrate: Varying the surface structure or the molecular species influenced the frequency of the oscillatory mode considerably.

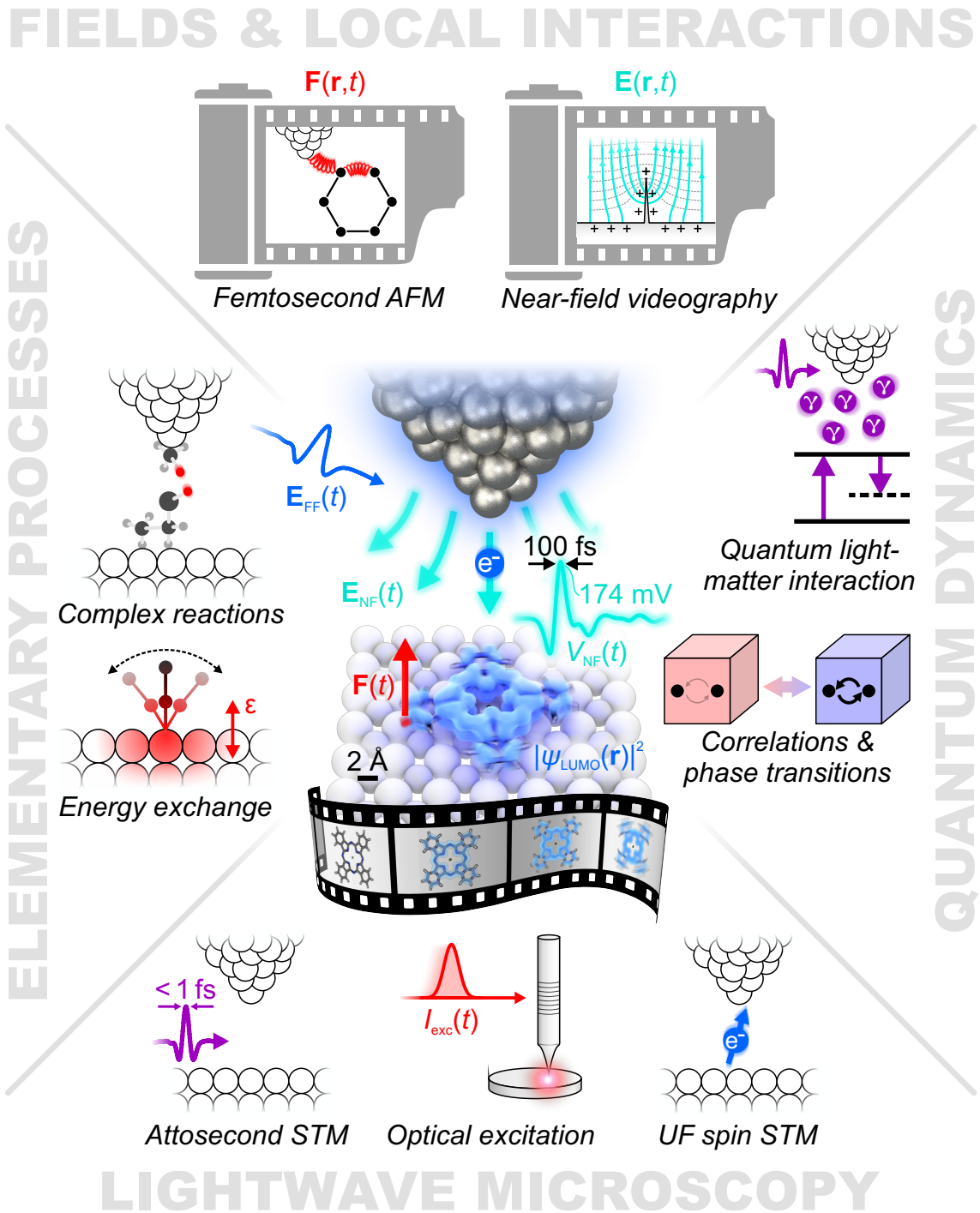
FIELDS & LOCAL INTERACTIONS
ELEMENTARY PROCESSES
QUANTUM DYNAMICS
LIGHTWAVE MICROSCOPY
F(r,t)
E(r,t)
Femtosecond AFM
Near-field videography
Complex reactions
Energy exchange
Quantum light-matter interaction
Correlations & phase transitions
E_FF(t)
E_NF(t)
100 fs
174 mV
V_NF(t)
F(t)
2 Å
|ψ_LUMO(r)|²
ε
< 1 fs
I_exc(t)
Attosecond STM
Optical excitation
UF spin STM

Figure 5.1 | Schematic illustration of explored phenomena and future perspectives in lightwave STM. The main innovations presented in this thesis are summarized in the center of the figure. Lightwaves $\mathbf{E}_{\mathrm{FF}}(t)$ induced a near-field distribution $\mathbf{E}_{\mathrm{NF}}(t)$ in an atom scale STM junction. The local fields could drive ultrafast electron tunneling to sense the density $|\psi_{\mathrm{LUMO}}(\mathbf{r})|^2$ (blue glow) of a select single-molecule orbital. Moreover we used femtosecond local forces $\mathbf{F}(t)$ to steer structural motion (blur) of a molecular switch. For the first time, these processes resolved ultrafast single-molecule dynamics and reactions, as well as local fields and light-matter interaction with combined atomic and femtosecond precision (film strip), and thereby set the stage for a variety of exciting future experiments (surrounding sketches). Following our initial observations, we anticipate that more complex elementary dynamics will be uncovered across the natural sciences (left). For example, the formation of a chemical bond between two individual molecules might be spatio-temporally resolved, and mechanisms of energy exchange at the atomic scale could be examined. More fundamentally, we assume that tip-confined electromagnetic fields will harness local light-matter interaction for unprecedented means of atom-scale videography (top). Ultrafast movies of local field distributions $\mathbf{E}(\mathbf{r},t)$ could revolutionize design strategies in nanotechnology, and lightwave-driven forces $\mathbf{F}(\mathbf{r},t)$ might facilitate femtosecond atomic force microscopy (AFM). Technical developments can be expected to improve the degree of control in lightwave STM (bottom). While higher optical driving frequencies may control tunnel events faster to access the domain of attosecond dynamics, ultrafast (UF) spin-polarized STM could visualize single-spin evolution in space and time. Also, optical excitation may prepare novel types of localized non-equilibrium states. We assume that these advances will eventually allow probing new types of quantum dynamics (right). Particularly, local correlations that shape phase transitions in solids could be observed at the single-particle level. Ultimately we believe that harnessing the full quantum-mechanical properties of atom-scale light-matter interaction (γ, photons) will provide unprecedented access to the quantum dynamics that lie at the heart of all natural sciences.

Outlook: Elementary energy exchange. We expect that extending the presented experiments will provide quantitative insights into elementary processes that underlie all natural sciences (Fig. 5.1, left). For example, observing molecular vibrations up to much longer delay times may directly reveal the coupling mechanisms of surface adsorbates. While we have not observed any significant decay of single-molecule oscillations so far, more polar molecular species should in principle couple strongly to the electron bath and phonons of the substrate[137,138].

In fact, the question through which mechanisms adsorbates exchange energy with a surface, and how fast, has far-reaching consequences for the entire domains of catalysis and surface (photo)chemistry[12,13,139–141], as well as photovoltaics[14,15]. For many reactions, multifaceted potential-energy landscapes are known to give rise to a variety of microscopic transition paths. Characterizing the ultrafast molecular motion that lies at the heart of such reactions and transitions, however, has so far almost entirely relied on theoretical modeling[138]. Lifetime measurements could gauge transport simulations[142] to scrutinize energy exchange at the single-quantum level. Particularly, the interplay of internal vibrations and electronic wavepacket motion – the key quantum-chemical coordinates[1] – might be disentangled.

We expect that future lightwave-STM experiments will systematically capture the ultrafast motion and excitation dynamics of adsorbates on various chemically active surfaces directly in ultrafast movies. In this way, the kinetics of surface chemistry will become visible in the most direct way.

Ultrafast action spectroscopy. We explored that, in order to observe reactions that may involve multiple different transition paths, single-event detection is vital. To this end, we implemented a strategy that allows us to monitor individual switching events of a single bistable molecule. We found that charging the molecule by single-electron tunnel injection statistically triggers switching reactions. Our ultrafast action spectroscopy resolved these reaction rates non-invasively, separately for both switching directions, and with an accuracy on the order of 10^{-4}.

Outlook: Complex reactions. We expect that resolving more complex transitions including on-surface reactions between multiple constituents[143] will pave the way towards chemical videography. In particular, we anticipate probing of three-

dimensional structures such as upright-oriented functional molecules[63] and folding networks of a single protein molecule[144] on their intrinsic time scales.

Eventually combining our approach with functionalized tips might enable four-dimensional probing of local chemical function (Fig. 5.1, left). Preliminary experiments not detailed in this work have shown that lightwave-STM snapshot imaging also works with tips functionalized via single carbon monoxide molecules. In other time-integrated studies, reactions between molecules that cling to an STM tip with substrate-adsorbed species have shed light on how local fields can modify single-molecule chemistry[145]. We expect that combining this idea with ultrafast lightwave control will observe the build-up of chemical interaction between multiple molecules in space and time, possibly with statistical specificity.

Femtosecond atomic forces. To control matter dynamically in the most direct way, we introduced femtosecond atomic forces as a novel stimulus that steers structural motion locally, with atomic precision. The forces derive from tip-confined electric-field waveforms that we tailor externally. In our qualitatively new experiments, we could apply ultrafast forces to coherently steer ultrafast motion of a molecular switch, which directly modulated its reaction statistics on the femtosecond scale. A more detailed examination of the control mechanism revealed that the dynamical forces can act locally on key atoms of the switch to steer a select vibrational degree of freedom at will. The first ultrafast molecular movie resolved the spatio-temporal switching statistics of the molecule in motion, confirming the atomic definition of the force stimulus.

Outlook: Detection of ultrafast atomic forces. The rich near-field interactions accessed by lightwave STM promise that a variety of local observables will be captured in ultrafast movies in the future (Fig. 5.1, top). For example, detecting local forces in time-integrated experiments has resolved most subtle interactions at atomic scales, and imaged matter with unparalleled spatial resolution. Atomic force microscopy extends the scope of scanning probe techniques to insulating samples. Owing to steep technological progress[146], AFM has become a standard tool for nano-scale topographic sensing, even down to sub-atomic precision[147]. Compared to tunnel microscopy, AFM can also sense bound electrons with an energy far below the Fermi

edge, allowing for a detailed structural analysis of (artificial) quantum objects[62,143].

When synchronized light pulses are coupled to a force microscope, tip-confined transient dipole fields[16] might ultimately allow time-resolved sensing of atomic femtosecond forces. The major technical challenge of ultrafast AFM is measuring such extremely small force contributions that are strongly confined in time and space at the same time. To this end, novel detection strategies are under development[148,149]. We anticipate that combining femtosecond-force control and detection will probe kinetics at the atomic scale with unprecedented clarity: Reactions at the single-molecule level might be captured in ultrafast movies that resolve individual chemical bonds breaking and forming.

Quantitative atom-scale near fields. All these present and potential future experiments are intimately connected with light-matter interaction at atomic length scales. While local electromagnetic waveforms steer the respective dynamics, back-action may drastically reshape the near fields, possibly even non-classically.

To provide clear access to these mostly unexplored phenomena, we developed the first quantitative detection of atom-scale femtosecond near fields. The measurement utilized a molecular switch as a gauged local voltage probe. We resolved tip-confined terahertz waveforms, which exhibit rich sub-cycle details distinct from the external excitation field. These features are reproduced very accurately by a plasmonic simulation that visualizes how the far-field waves couple to the tip-sample geometry. Surprisingly, the classical simulation even describes the far-to-near-field transfer quantitatively.

A full ab initio calculation of the light-matter dynamics in the tunnel junction unveils how sub-cycle electron tunneling and local screening affect the near fields. The simulation confirms our quantitative calibration and shows that, while single-electron tunneling warrants minimal back-action, multi-electron quantum dynamics may dominate future more complex scenarios.

Outlook: Near-field videography and predictive nanodesign. With our local sampling scheme, atom-scale near fields can now be spatio-temporally mapped. We expect that similar experiments will make use of the non-linear tunneling onset instead of a molecular sensor, allowing us to capture ultrafast movies of sub-angstrom

field distributions (Fig. 5.1, top). The electromagnetic dynamics of a variety of elementary excitations could then be directly visualized, ranging from individual quasiparticles to on-chip implementations of future information processing.

Also, ultrafast near-field movies may revolutionize the design of nano-plasmonic technology: State-of-the-art simulations that bridge the gap between macroscopic light and atomic waveforms can now be precisely calibrated. In the future, novel metamaterials and atomic-scale devices may harness quantitatively-tailored coherent near fields for opto-electronic function faster than a cycle of light.

While structural motion such as the molecular vibrations examined in this thesis often occur on picosecond time scales, such opto-electronic dynamics naturally occur at a much faster femtosecond pace. To directly watch electron wavefunctions evolve in ultrafast movies, we anticipate to improve the temporal resolution of lightwave STM drastically.

Outlook: Attosecond STM. We expect that a number of technical developments will further improve the performance of lightwave STM, add novel control mechanisms and provide access to additional atomistic degrees of freedom (Fig. 5.1, bottom). These developments may provide a qualitatively new access to quantum-mechanical dynamics that lie at the heart of fundamental light-matter interaction as well as new materials (Fig. 5.1, right).

We expect that scaling the optical source to higher driving frequencies[28] will ramp up the temporal resolution of lightwave STM. At mid-infrared (MIR) and near-infrared frequencies of 30 to 300 THz, lightwave-driven tunnel control in the strong-field regime of light-matter interaction should still be possible. To this end, novel specifically tailored schemes for waveform generation are required. This demand has triggered a recent surge in the development of new MIR sources which provide CEP-stable sub-cycle waveforms at high field strengths and large repetitions rates[150–152]. We assume that future MIR-based lightwave STM will enable attosecond atomic microscopy, opening the door to a wealth of dynamics at the time scale of electron motion.

Fascinatingly, videography in this spatio-temporal regime will resolve qualitatively different physics that have not been directly watched in slow-motion so far. Electrons in solids may be prepared in non-equilibrium distributions that induce ex-

ceptional transport properties on few-femtosecond time scales. Even the dephasing of (quasi)particles might be visualized, which could shed light on the microscopic mechanisms of high-temperature superconducting phases, or any bosonic condensation. Observing such dynamics at combined atomic and few-femtosecond scales will naturally display correlations.

Outlook: Correlations and phase transitions. We anticipate that upcoming lightwave-STM experiments will examine phase transitions in solids locally, at the scale of individual atoms. Ultrafast movies of angstrom-scale phase-change dynamics could disentangle electronic, structural and other quantum-mechanical degrees of freedom directly in the time domain. This may resolve the microscopic workings of a variety of transitions including insulator-metal and superconducting phases, topologically protected states and (pseudo)spin order (Fig. 5.1, right).

More specifically, we envisage perturbing the inner "functioning" of a certain phase *locally* by electron injection, atomically strong fields or tip-confined optical pulses. This may not only shed light on the spatial structure of complex phases, for example in highly-correlated materials. We expect that such experiments will also clarify the role of defects, wavefunction pinning and symmetry-breaking edges, all at the intrinsic spatio-temporal scale of condensed matter. Resolving these atomistic details might clear the path towards technological implementations of new platforms for quantum information processing.

For instance, time-resolved tunnel spectroscopy of solids might track the opening and closing of energy gaps, with atomic precision. This could, for example, visualize phase transitions locally, such as a build-up of Kondo screening in an impulsively perturbed Kondo insulator. Moreover, one might also map spatial order such as charge density waves[113] directly in femtosecond movies. Hence, identifying and characterizing order parameters in different phases of a material could become as direct and clear as possible.

Also competing orders in highly correlated materials such as the widely studied copper oxides[2] could be followed dynamically. This might visualize their interplay during ultrafast phase transitions, at the length scale of one atom: For example in cuprates, one could resolve the spatial nematic texture of the electronic wavefunctions[59] during quench or (re)formation of the pseudogap[153].

We expect that also phase correlations will be resolved in space and time, and maybe even their statistics. For example, tracking phase coherence[154] in ultrafast movies might answer the question how phase fluctuations of preformed Cooper pairs shape the phase diagram of high-temperature superconductors.

Outlook: Physical limits and new regimes. To resolve even faster dynamics, another physical regime will be encountered presumably. From a fundamental point of view, one may assume that the temporal resolution in lightwave STM will be limited by the plasma frequency of the tip material. Experiments such as our waveform sampling, however, might explore non-classical physics that eventually grant access to even faster dynamics. For instance, one could envision that squeezed states of light might provide more specific quantum control of gap-confined light-matter dynamics: Eventually, locally correlating light and matter quantum fields could allow for a tailored information transfer beyond classical restrictions. In particular at driving frequencies that mix strong-field dynamics and (multi-)photon excitation, even pulse-to-pulse quantum fluctuations may have to be considered.

Besides possible future probing of even faster dynamics, the photon regime of light-matter interaction can be readily used as an intriguing new excitation path: We intend to prepare optically accessible non-equilibrium states and time-resolve their evolution via terahertz-driven STM.

Outlook: Optical excitation. Light pulses in the visible domain[23] can resonantly pump local transitions, or create electron-hole pairs. Technically, one could make use of plasma resonances of the tip to propagate optical pulses efficiently into the tunnel gap (Fig. 5.1, bottom). Grating structures can facilitate coupling to the tip and tailor dispersion of the apex-confined pulses[155,156]. Such optical pulses could excite elementary dynamics in promising opto-electronic platforms such as two-dimensional van der Waals materials. The effect of atom-scale textures such as defects or Moiré patterns on femtosecond electron motion might be directly watched. Also localized electronic states[56] could be spatio-temporally mapped. Tailoring the polarization of optical pulses might even allow spin- or valley-selective excitation, accessing select trajectories in reciprocal space for ultrafast valleytronics[5].

Outlook: Spin-controlled electron tunneling. Complementary, spin-selective probing of transient local states could be attained by combining lightwave tunnel control with spin-polarized STM. Making use of the tunnel magnetoresistance through spin-polarized STM tips, writing and detection of individual skyrmions[157] as well as single-atom magnets[54] has been attained. Also spin relaxation dynamics on nanosecond time scales could be resolved[19]. We anticipate that lightwave control of spin-polarized STM will allow spin-selective injection and read-out of a single electron, with simultaneous atomic and sub-cycle precision (Fig. 5.1, bottom).

This toolkit could characterize fundamental atom-scale magnetic interactions and excitations, and resolve dynamics induced by spin-orbit coupling. Molecular spintronics[158] may access spin-orbit dynamics within single molecules[159] directly in the time domain. Also, we expect that transport phenomena will be monitored directly on the relevant spatio-temporal scales, and with spin selectivity. Wavepacket motion and spin relaxation could be time-resolved, and local dynamics at defects and custom-engineered edges might be directly observed. In particular, we anticipate femtosecond videography of lightwave-driven transport through spin-textured channels such as topologically-protected Dirac surface states[34] or edge channels in graphene nanoribbons[160].

Outlook: Quantum light-matter interaction and molecular bionics. From a fundamental point of view, we hope that our exploration of atomically confined lightwaves will inspire studies that reveal the limits of classical nanooptics, and directly visualize the quantum nature of atom-scale light-matter interaction (Fig. 5.1, right). In this spirit, some day, elementary processes like the absorption of light during an electronic transition may be directly visualized. Such observations could help us understand and copy those molecular bio-processes that evolution has evolved to unparalleled elegance.

For example, if we mastered solar-energy conversion in a way similar to natural light-harvesting complexes[7,8] – almost perfectly efficient, bio-degradable and based on cheap organic materials – the human energy crisis would be solved. Moreover, both the future of medical treatment as well as a next-generation sustainable chemical industry seem to depend on the mastery of protein dynamics, at the single-molecule level. Directed evolution of enzymes[161], which are proteins that catalyze chemical

reactions, has generated levels of activity and specificity not known to exist in nature[162]. Today's routine uses include more environmentally friendly manufacturing of chemical substances, such as pharmaceuticals, and the production of renewable fuels for a more sustainable transport sector.

The key challenge in discovering novel enzymatic tools is understanding the relationship between the protein sequence, ultrafast molecular dynamics and their (bio)chemical function. So far, these connections need to be deduced from structural data, with new approaches employing artificial intelligence to optimize in-vitro evolution[163]. We hope that femtosecond videography of individual enzymes at work will eventually uncover these connections in the most direct way. One might directly observe which dynamics evolution prefers, and how they affect bio-chemical function, possibly even with quantum-statistical sensitivity. We could watch and learn from nature's most efficient elementary processes – possibly the most fruitful ambition of interdisciplinary natural science.

Scientific record

Publications in peer-reviewed journals

- Tyler L. Cocker*, Dominik Peller*, Ping Yu, Jascha Repp & Rupert Huber
  * equal contributions
  Tracking the ultrafast motion of a single molecule by femtosecond orbital imaging
  Nature **539**, 263–267 (2016) | doi:10.1038/nature19816

  ▶ This work has been featured in a News and Views article by Nicholas Camillone III
  Nanoscience: Single-molecule instant replay
  Nature **539**, 170–171 (2016) | doi:10.1038/539170a

  ▶ This work has been highlighted in a News feature by Mark Peplow
  The next big hit in molecule Hollywood
  Nature **544**, 408–410 (2017) | doi:10.1038/544408a

- Matthias Knorr, Jürgen Raab, Maximilian Tauer, Philipp Merkl, Dominik Peller, Emanuel Wittmann, Eberhard Riedle, Christoph Lange & Rupert Huber
  Phase-locked multi-terahertz electric fields exceeding 13 MV/cm at 190 kHz repetition rate
  Optics Letters **42**, 4367–4370 (2017) | doi:10.1364/OL.42.004367

- Philipp Merkl, Matthias Knorr, Christian Meineke, Lukas Kastner, Dominik Peller & Rupert Huber
  Multibranch pulse synthesis and electro-optic detection of subcycle multi-terahertz electric fields
  Optics Letters **44**, 5521–5524 (2019) | doi:10.1364/OL.44.005521

- Dominik Peller, Lukas Z. Kastner, Thomas Buchner, Carmen Roelcke, Florian Albrecht, Nikolaj Moll, Rupert Huber & Jascha Repp
  Sub-cycle atomic-scale forces coherently control a single-molecule switch
  Nature, accepted

- Dominik Peller, Carmen Roelcke, Lukas Z. Kastner, Thomas Buchner, Alexander Neef, Johannes Hayes, Franco Bonafé, Dominik Sidler, Michael Ruggenthaler, Ángel Rubio, Jascha Repp & Rupert Huber
  Quantitative sampling of atomic-scale electromagnetic waveforms
  Nature Photonics, under review

Publications in international conference proceedings

- Dominik Peller, Tyler L. Cocker, Ping Yu, Rupert Huber & Jascha Repp
  Watching a single molecular orbital move
  Proceedings of the International Conference on Ultrafast Phenomena 2016 | doi:10.1364/UP.2016.UTh5A.7

- Dominik Peller, Tyler L. Cocker, Ping Yu, Jascha Repp & Rupert Huber
  Tracking the ultrafast motion of a single molecular orbital
  Proceedings of the International Conference on Infrared, Millimeter, and Terahertz Waves 2016 | doi:10.1109/IRMMW-THz.2016.7758414

Contributions at international conferences

- **International Conference on Ultrafast Phenomena 2016**
  18–22 July 2016 | Santa Fe, USA
  Postdeadline talk

  Dominik Peller, Tyler L. Cocker, Ping Yu, Rupert Huber & Jascha Repp
  Watching a single molecular orbital move

  ▶ **Honored with *Best Student Talk Award***

- **International Conference on Infrared, Millimeter, and Terahertz Waves 2016**
  26–30 September 2016 | Copenhagen, Denmark
  Invited keynote talk

  Dominik Peller, Tyler L. Cocker, Ping Yu, Jascha Repp & Rupert Huber
  Tracking the ultrafast motion of a single molecular orbital

- **24th International Colloquium on Scanning Probe Microscopy**
  14–16 December 2016 | Honolulu, USA
  Invited talk

  Dominik Peller, Tyler L. Cocker, Ping Yu, Jascha Repp & Rupert Huber
  Recording femtosecond sub-Å snapshots with lightwave-STM

- **6th International Symposium on Organic and Inorganic Electronic Materials and Related Nanotechnologies**
  19–21 June 2017 | Fukui, Japan
  Invited talk

  Dominik Peller, Tyler L. Cocker, Ping Yu, Jascha Repp & Rupert Huber
  Femtosecond slow-motion of a molecular orbital in a single vibrating molecule

- **Gordon Research Conference – Dynamics at Surfaces**
  29 July – 04 August 2017 | Newport, USA
  Invited poster presentation and talk

  Dominik Peller, Tyler L. Cocker, Ping Yu, Jascha Repp & Rupert Huber
  Watching ultrafast surface dynamics of a single molecule in slow motion

- **CLEO: Conference on Lasers and Electro-Optics 2018**
  13–18 June 2018 | San Jose, USA
  Invited talk

  Dominik Peller, Tyler L. Cocker, Ping Yu, Jascha Repp & Rupert Huber
  Watching a single molecular orbital move

  ▶ **Awarded the *Maiman Student Paper Competition Grand Prize***

- **Inaugural Workshop on Molecular Videography**
  18–21 September 2018 | Telluride, USA
  Invited talk

  Dominik Peller
  From molecular movies to single quantum events

- **International Conference on Optical Terahertz Science and Technology**
  11–15 March 2019 | Santa Fe, USA
  Contributed talk

  Dominik Peller, Thomas Buchner, Lukas Kastner, Tyler L. Cocker, Rupert Huber & Jascha Repp
  Single switching events of one molecule observed by femtosecond STM

- **Spring Meeting of the Deutsche Physikalische Gesellschaft 2019**
  01–05 April 2019 | Regensburg, Germany
  Contributed talk

  Dominik Peller, Thomas Buchner, Lukas Kastner, Carmen Roelcke, Rupert Huber & Jascha Repp
  Single switching events of one molecule observed by femtosecond STM

- **National Meeting of the American Chemical Society 2019**
  26–29 August 2019 | San Diego, USA
  Invited talk

  Dominik Peller, Thomas Buchner, Lukas Kastner, Carmen Roelcke, Rupert Huber & Jascha Repp
  Single switching events of one molecule observed by femtosecond STM

- **CLEO: Conference on Lasers and Electro-Optics 2020**
  10–15 May 2020 | San Jose, USA
  Invited talk, withdrawn

  Dominik Peller, Lukas Z. Kastner, Thomas Buchner, Carmen Roelcke, Florian Albrecht, Nikolaj Moll, Jascha Repp & Rupert Huber
  Femtosecond Atomic Forces Coherently Control Single-Molecule Switching Reactions

- **7th Ultrafast Dynamics and Metastability & Ultrafast Bandgap Photonics Conference**
  18–20 May 2021 | Hersonissos, Greece
  Invited talk

  Dominik Peller, Lukas Z. Kastner, Thomas Buchner, Carmen Roelcke, Florian Albrecht, Nikolaj Moll, Jascha Repp & Rupert Huber
  Sub-Cycle Atomic Forces Coherently Control Single-Molecule Switching Reactions

References

1. Yarkony, D. R. Nonadiabatic Quantum Chemistry – Past, Present, and Future. *Chemical Reviews* **112**, 481–498 (2012).

2. Keimer, B., Kivelson, S. A., Norman, M. R., Uchida, S. & Zaanen, J. From quantum matter to high-temperature superconductivity in copper oxides. *Nature* **518**, 179–186 (2015).

3. Awschalom, D. D., Bassett, L. C., Dzurak, A. S., Hu, E. L. & Petta, J. R. Quantum Spintronics: Engineering and Manipulating Atom-Like Spins in Semiconductors. *Science* **339**, 1174–1179 (2013).

4. Kues, M. *et al.* On-chip generation of high-dimensional entangled quantum states and their coherent control. *Nature* **546**, 622–626 (2017).

5. Langer, F. *et al.* Lightwave valleytronics in a monolayer of tungsten diselenide. *Nature* **557**, 76–80 (2018).

6. Atatüre, M., Englund, D., Vamivakas, N., Lee, S. Y. & Wrachtrup, J. Material platforms for spin-based photonic quantum technologies. *Nature Reviews Materials* **3**, 38–51 (2018).

7. Herek, J. L., Wohlleben, W., Cogdell, R. J., Zeidler, D. & Motzkus, M. Quantum control of energy flow in light harvesting. *Nature* **417**, 533–535 (2002).

8. Hildner, R., Brinks, D., Nieder, J. B., Cogdell, R. J. & van Hulst, N. F. Quantum Coherent Energy Transfer over Varying Pathways in Single Light-Harvesting Complexes. *Science* **340**, 1448–1451 (2013).

9. Lambert, N. *et al.* Quantum biology. *Nature Physics* **9**, 10–18 (2013).

10. Romero, E., Novoderezhkin, V. I. & van Grondelle, R. Quantum design of photosynthesis for bio-inspired solar-energy conversion. *Nature* **543**, 355–365 (2017).

11. Scholes, G. D. *et al.* Using coherence to enhance function in chemical and biophysical systems. *Nature* **543**, 647–656 (2017).

12. Bonn, M. Phonon- Versus Electron-Mediated Desorption and Oxidation of CO on Ru(0001). *Science* **285**, 1042–1045 (1999).

13. Dell'Angela, M. *et al.* Real-Time Observation of Surface Bond Breaking with an X-ray Laser. *Science* **339**, 1302–1305 (2013).

14. Zimmerman, P. M., Zhang, Z. & Musgrave, C. B. Singlet fission in pentacene through multi-exciton quantum states. *Nature Chemistry* **2**, 648–652 (2010).

15. Tabachnyk, M. *et al.* Resonant energy transfer of triplet excitons from pentacene to PbSe nanocrystals. *Nature Materials* **13**, 1033–1038 (2014).

16. Eisele, M. *et al.* Ultrafast multi-terahertz nano-spectroscopy with sub-cycle temporal resolution. *Nature Photonics* **8**, 841–845 (2014).

17. Huang, S.-W. *et al.* High conversion efficiency, high energy terahertz pulses by optical rectification in cryogenically cooled lithium niobate. *Optics Letters* **38**, 796–798 (2013).

18. Feist, A. *et al.* Ultrafast transmission electron microscopy using a laser-driven field emitter: Femtosecond resolution with a high coherence electron beam. *Ultramicroscopy* **176**, 63–73 (2017).

19. Loth, S., Etzkorn, M., Lutz, C. P., Eigler, D. M. & Heinrich, A. J. Measurement of Fast Electron Spin Relaxation Times with Atomic Resolution. *Science* **329**, 1628–1630 (2010).

20. Cocker, T. L., Peller, D., Yu, P., Repp, J. & Huber, R. Tracking the ultrafast motion of a single molecule by femtosecond orbital imaging. *Nature* **539**, 263–267 (2016).

21. Peller, D. *et al.* Sub-cycle atomic-scale forces coherently control a single-molecule switch. *Nature, accepted* (2020).

22. Peller, D. *et al.* Quantitative sampling of atomic-scale electromagnetic waveforms. *Nature Photonics, under review* (2020).

23. Cocker, T. L. *et al.* An ultrafast terahertz scanning tunnelling microscope. *Nature Photonics* **7**, 620–625 (2013).

24. Yoshioka, K. *et al.* Real-space coherent manipulation of electrons in a single tunnel junction by single-cycle terahertz electric fields. *Nature Photonics* **10**, 762–765 (2016).

25. Jelic, V. *et al.* Ultrafast terahertz control of extreme tunnel currents through single atoms on a silicon surface. *Nature Physics* **13**, 591–598 (2017).

26. Yoshioka, K. *et al.* Tailoring Single-Cycle Near Field in a Tunnel Junction with Carrier-Envelope Phase-Controlled Terahertz Electric Fields. *Nano Letters* **18**, 5198–5204 (2018).

27. Yoshida, S. *et al.* Subcycle Transient Scanning Tunneling Spectroscopy with Visualization of Enhanced Terahertz Near Field. *ACS Photonics* **6**, 1356–1364 (2019).

28. Garg, M. & Kern, K. Attosecond coherent manipulation of electrons in tunneling microscopy. *Science* **367**, 411–415 (2020).

29. Corkum, P. B. & Krausz, F. Attosecond science. *Nature Physics* **3**, 381–387 (2007).

30. Goulielmakis, E. *et al.* Attosecond Control and Measurement: Lightwave Electronics. *Science* **317**, 769–775 (2007).

31. Ghimire, S. *et al.* Observation of high-order harmonic generation in a bulk crystal. *Nature Physics* **7**, 138–141 (2011).

32. Schubert, O. *et al.* Sub-cycle control of terahertz high-harmonic generation by dynamical Bloch oscillations. *Nature Photonics* **8**, 119–123 (2014).

33. Hohenleutner, M. *et al.* Real-time observation of interfering crystal electrons in high-harmonic generation. *Nature* **523**, 572–575 (2015).

34. Reimann, J. *et al.* Subcycle observation of lightwave-driven Dirac currents in a topological surface band. *Nature* **562**, 396–400 (2018).

35. Schlauderer, S. *et al.* Temporal and spectral fingerprints of ultrafast all-coherent spin switching. *Nature* **569**, 383–387 (2019).

36. Liu, N., Tang, M. L., Hentschel, M., Giessen, H. & Alivisatos, A. P. Nanoantenna-enhanced gas sensing in a single tailored nanofocus. *Nature Materials* **10**, 631–636 (2011).

37. Kosaka, P. M. *et al.* Detection of cancer biomarkers in serum using a hybrid mechanical and optoplasmonic nanosensor. *Nature Nanotechnology* **9**, 1047–1053 (2014).

38. Linic, S., Christopher, P. & Ingram, D. B. Plasmonic-metal nanostructures for efficient conversion of solar to chemical energy. *Nature Materials* **10**, 911–921 (2011).

39. Fiorino, A. *et al.* Nanogap near-field thermophotovoltaics. *Nature Nanotechnology* **13**, 806–811 (2018).

40. Li, S., Chen, S., Li, J., Wu, R. & Ho, W. Joint Space-Time Coherent Vibration Driven Conformational Transitions in a Single Molecule. *Physical Review Letters* **119**, 176002 (2017).

41. Böckmann, H. *et al.* Near-Field Spectral Response of Optically Excited Scanning Tunneling Microscope Junctions Probed by Single-Molecule Action Spectroscopy. *The Journal of Physical Chemistry Letters* **10**, 2068–2074 (2019).

42. Wimmer, L. *et al.* Terahertz control of nanotip photoemission. *Nature Physics* **10**, 432–436 (2014).

43. Barbry, M. *et al.* Atomistic Near-Field Nanoplasmonics: Reaching Atomic-Scale Resolution in Nanooptics. *Nano Letters* **15**, 3410–3419 (2015).

44. Jestädt, R., Ruggenthaler, M., Oliveira, M. J. T., Rubio, A. & Appel, H. Light-matter interactions within the Ehrenfest–Maxwell–Pauli–Kohn–Sham framework: fundamentals, implementation, and nano-optical applications. *Advances in Physics* **68**, 225–333 (2019).

45. Peplow, M. The next big hit in molecule Hollywood. *Nature* **544**, 408–410 (2017).

46. Binnig, G., Rohrer, H., Gerber, C. & Weibel, E. Surface Studies by Scanning Tunneling Microscopy. *Physical Review Letters* **49**, 57–61 (1982).

47. Feynman, R. P. There's plenty of room at the bottom. *Engineering and Science* **23**, 22–36 (1960).

48. Binnig, G., Rohrer, H., Gerber, C. & Weibel, E. 7×7 Reconstruction on Si(111) Resolved in Real Space. *Physical Review Letters* **50**, 120–123 (1983).

49. Crommie, M. F., Lutz, C. P. & Eigler, D. M. Confinement of Electrons to Quantum Corrals on a Metal Surface. *Science* **262**, 218–220 (1993).

50. Heinrich, A. J., Lutz, C. P., Gupta, J. A. & Eigler, D. M. Molecule Cascades. *Science* **298**, 1381–1387 (2002).

51. Stroscio, J. A. & Celotta, R. J. Controlling the Dynamics of a Single Atom in Lateral Atom Manipulation. *Science* **306**, 242–247 (2004).

52. Pavliček, N., Swart, I., Niedenführ, J., Meyer, G. & Repp, J. Symmetry Dependence of Vibration-Assisted Tunneling. *Physical Review Letters* **110**, 136101 (2013).

53. Loth, S., Baumann, S., Lutz, C. P., Eigler, D. M. & Heinrich, A. J. Bistability in Atomic-Scale Antiferromagnets. *Science* **335**, 196–199 (2012).

54. Natterer, F. D. *et al.* Reading and writing single-atom magnets. *Nature* **543**, 226–228 (2017).

55. Rutter, G. M. *et al.* Scattering and Interference in Epitaxial Graphene. *Science* **317**, 219–222 (2007).

56. Pan, Y. *et al.* Quantum-Confined Electronic States Arising from the Moiré Pattern of MoS_2–WSe_2 Heterobilayers. *Nano Letters* **18**, 1849–1855 (2018).

57. Spinelli, A., Bryant, B., Delgado, F., Fernández-Rossier, J. & Otte, A. F. Imaging of spin waves in atomically designed nanomagnets. *Nature Materials* **13**, 782–785 (2014).

58. Hanneken, C. *et al.* Electrical detection of magnetic skyrmions by tunnelling non-collinear magnetoresistance. *Nature Nanotechnology* **10**, 1039–1042 (2015).

59. Lawler, M. J. *et al.* Intra-unit-cell electronic nematicity of the high-T_c copper-oxide pseudogap states. *Nature* **466**, 347–351 (2010).

60. Pascual, J. I. *et al.* Seeing molecular orbitals. *Chemical Physics Letters* **321**, 78–82 (2000).

61. Repp, J., Meyer, G., Stojković, S. M., Gourdon, A. & Joachim, C. Molecules on Insulating Films: Scanning-Tunneling Microscopy Imaging of Individual Molecular Orbitals. *Physical Review Letters* **94**, 026803 (2005).

62. Pavliček, N. *et al.* Synthesis and characterization of triangulene. *Nature Nanotechnology* **12**, 308–311 (2017).

63. Esat, T., Friedrich, N., Tautz, F. S. & Temirov, R. A standing molecule as a single-electron field emitter. *Nature* **558**, 573–576 (2018).

64. Merlein, J. *et al.* Nanomechanical control of an optical antenna. *Nature Photonics* **2**, 230–233 (2008).

65. Liu, M. *et al.* Terahertz-field-induced insulator-to-metal transition in vanadium dioxide metamaterial. *Nature* **487**, 345–348 (2012).

66. Spektor, G. *et al.* Revealing the subfemtosecond dynamics of orbital angular momentum in nanoplasmonic vortices. *Science* **355**, 1187–1191 (2017).

67. Seo, M. A. *et al.* Terahertz field enhancement by a metallic nano slit operating beyond the skin-depth limit. *Nature Photonics* **3**, 152–156 (2009).

68. Savage, K. J. *et al.* Revealing the quantum regime in tunnelling plasmonics. *Nature* **491**, 574–577 (2012).

69. Rybka, T. *et al.* Sub-cycle optical phase control of nanotunnelling in the single-electron regime. *Nature Photonics* **10**, 667–670 (2016).

70. Krüger, M., Schenk, M. & Hommelhoff, P. Attosecond control of electrons emitted from a nanoscale metal tip. *Nature* **475**, 78–81 (2011).

71. Herink, G., Solli, D. R., Gulde, M. & Ropers, C. Field-driven photoemission from nanostructures quenches the quiver motion. *Nature* **483**, 190–193 (2012).

72. Herink, G., Wimmer, L. & Ropers, C. Field emission at terahertz frequencies: AC-tunneling and ultrafast carrier dynamics. *New Journal of Physics* **16**, 123005 (2014).

73. Feist, A. *et al.* Quantum coherent optical phase modulation in an ultrafast transmission electron microscope. *Nature* **521**, 200–203 (2015).

74. Förg, B. *et al.* Attosecond nanoscale near-field sampling. *Nature Communications* **7**, 11717 (2016).

75. Müller, M., Kravtsov, V., Paarmann, A., Raschke, M. B. & Ernstorfer, R. Nanofocused Plasmon-Driven Sub-10 fs Electron Point Source. *ACS Photonics* **3**, 611–619 (2016).

76. Basov, D. N., Fogler, M. M. & Garcia de Abajo, F. J. Polaritons in van der Waals materials. *Science* **354**, 195 (2016).

77. Hamers, R. J. & Cahill, D. G. Ultrafast time resolution in scanned probe microscopies. *Applied Physics Letters* **57**, 2031–2033 (1990).

78. Weiss, S., Ogletree, D. F., Botkin, D., Salmeron, M. & Chemla, D. S. Ultrafast scanning probe microscopy. *Applied Physics Letters* **63**, 2567–2569 (1993).

79. Groeneveld, R. H. M. & van Kempen, H. The capacitive origin of the picosecond electrical transients detected by a photoconductively gated scanning tunneling microscope. *Applied Physics Letters* **69**, 2294–2296 (1996).

80. Nunes, G. & Freeman, M. R. Picosecond Resolution in Scanning Tunneling Microscopy. *Science* **262**, 1029–1032 (1993).

81. Terada, Y., Yoshida, S., Takeuchi, O. & Shigekawa, H. Real-space imaging of transient carrier dynamics by nanoscale pump-probe microscopy. *Nature Photonics* **4**, 869–874 (2010).

82. Dolocan, A., Acharya, D. P., Zahl, P., Sutter, P. & Camillone, N. Two-Color Ultrafast Photoexcited Scanning Tunneling Microscopy. *The Journal of Physical Chemistry C* **115**, 10033–10043 (2011).

83. Keldysh, L. V. Ionization in the Field of a Strong Electromagnetic Wave. *Journal of Experimental and Theoretical Physics* **10**, 1307–1314 (1965).

84. FEMTO Messtechnnik GmbH, DLPCA-200 Variable Gain Low Noise Current Amplifier Datasheet (accessed 2020-04-28). URL `https://www.femto.de/images/pdf-dokumente/de-dlpca-200.pdf`.

85. Abbe, E. Beiträge zur Theorie des Mikroskops und der mikroskopischen Wahrnehmung. *Archiv für Mikroskopische Anatomie* **9**, 413–418 (1873).

86. Kang, J. H., Kim, D. S. & Park, Q.-H. Local Capacitor Model for Plasmonic Electric Field Enhancement. *Physical Review Letters* **102**, 093906 (2009).

87. Hebling, J., Almasi, G., Kozma, I. & Kuhl, J. Velocity matching by pulse front tilting for large area THz-pulse generation. *Optics Express* **10**, 1161 (2002).

88. Boyd, R. W. *Nonlinear Optics* (Academic Press, 2008), 3rd edn.

89. Hirori, H., Doi, A., Blanchard, F. & Tanaka, K. Single-cycle terahertz pulses with amplitudes exceeding 1 MV/cm generated by optical rectification in $LiNbO_3$. *Applied Physics Letters* **98**, 091106 (2011).

90. Valdmanis, J. A., Mourou, G. & Gabel, C. W. Picosecond electro-optic sampling system. *Applied Physics Letters* **41**, 211–212 (1982).

91. Wu, Q. & Zhang, X. C. Free-space electro-optic sampling of terahertz beams. *Applied Physics Letters* **67**, 3523 (1995).

92. Kübler, C., Huber, R., Tübel, S. & Leitenstorfer, A. Ultrabroadband detection of multi-terahertz field transients with GaSe electro-optic sensors: Approaching the near infrared. *Applied Physics Letters* **85**, 3360–3362 (2004).

93. Peller, D. *Ultrafast scanning tunneling microscopy of a molecular orbital in a single pentacene molecule.* (Master's Thesis, 2015).

94. Chen, C. J. *Introduction to Scanning Tunneling Microscopy* (Oxford University Press, 1993).

95. Park, H. *et al.* Nanomechanical oscillations in a single C_{60} transistor. *Nature* **407**, 57–60 (2000).

96. Steurer, W., Gross, L. & Meyer, G. Local thickness determination of thin insulator films via localized states. *Applied Physics Letters* **104**, 231606 (2014).

97. Rumble, J. R. *CRC Handbook of Chemistry and Physics* (CRC Press, 2019), 100th edn.

98. Binnig, G., Rohrer, H., Gerber, C. & Weibel, E. (111) facets as the origin of reconstructed Au(110) surfaces. *Surface Science* **131**, L379–L384 (1983).

99. Witte, G. & Wöll, C. External vibrations of hydrocarbons on Cu(100). *The Journal of Chemical Physics* **103**, 5860–5863 (1995).

100. Witte, G. *et al.* Damping of Molecular Motion on a Solid Substrate: Evidence for Electron-Hole Pair Creation. *Physical Review Letters* **80**, 121–124 (1998).

101. Hla, S.-W., Bartels, L., Meyer, G. & Rieder, K.-H. Inducing All Steps of a Chemical Reaction with the Scanning Tunneling Microscope Tip: Towards Single Molecule Engineering. *Physical Review Letters* **85**, 2777–2780 (2000).

102. Ternes, M., Lutz, C. P., Hirjibehedin, C. F., Giessibl, F. J. & Heinrich, A. J. The Force Needed to Move an Atom on a Surface. *Science* **319**, 1066–1069 (2008).

103. Ladenthin, J. N. *et al.* Force-induced tautomerization in a single molecule. *Nature Chemistry* **8**, 935–940 (2016).

104. García-López, V. *et al.* Molecular machines open cell membranes. *Nature* **548**, 567–572 (2017).

105. Garcia-Manyes, S. & Beedle, A. E. M. Steering chemical reactions with force. *Nature Reviews Chemistry* **1**, 0083 (2017).

106. Wu, S. W. & Ho, W. Two-photon-induced hot-electron transfer to a single molecule in a scanning tunneling microscope. *Physical Review B* **82**, 085444 (2010).

107. Lee, J., Perdue, S. M., Rodriguez Perez, A. & Apkarian, V. A. Vibronic Motion with Joint Angstrom-Femtosecond Resolution Observed through Fano Progressions Recorded within One Molecule. *ACS Nano* **8**, 54–63 (2014).

108. Yampolsky, S. *et al.* Seeing a single molecule vibrate through time-resolved coherent anti-Stokes Raman scattering. *Nature Photonics* **8**, 650–656 (2014).

109. Lee, J., Crampton, K. T., Tallarida, N. & Apkarian, V. A. Visualizing vibrational normal modes of a single molecule with atomically confined light. *Nature* **568**, 78–82 (2019).

110. Prokhorenko, V. I. *et al.* Coherent Control of Retinal Isomerization in Bacteriorhodopsin. *Science* **313**, 1257–1261 (2006).

111. Wörner, H. J., Bertrand, J. B., Kartashov, D. V., Corkum, P. B. & Villeneuve, D. M. Following a chemical reaction using high-harmonic interferometry. *Nature* **466**, 604–607 (2010).

112. Wolter, B. *et al.* Ultrafast electron diffraction imaging of bond breaking in di-ionized acetylene. *Science* **354**, 308–312 (2016).

113. Eichberger, M. *et al.* Snapshots of cooperative atomic motions in the optical suppression of charge density waves. *Nature* **468**, 799–802 (2010).

114. Kim, K. W. *et al.* Ultrafast transient generation of spin-density-wave order in the normal state of $BaFe_2As_2$ driven by coherent lattice vibrations. *Nature Materials* **11**, 497–501 (2012).

115. Nicholson, C. W. *et al.* Beyond the molecular movie: Dynamics of bands and bonds during a photoinduced phase transition. *Science* **362**, 821–825 (2018).

116. Ichikawa, H. *et al.* Transient photoinduced 'hidden' phase in a manganite. *Nature Materials* **10**, 101–105 (2011).

117. Stojchevska, L. *et al.* Ultrafast Switching to a Stable Hidden Quantum State in an Electronic Crystal. *Science* **344**, 177–180 (2014).

118. Zhang, J. *et al.* Cooperative photoinduced metastable phase control in strained manganite films. *Nature Materials* **15**, 956–960 (2016).

119. Durr, M. Probing High-Barrier Pathways of Surface Reactions by Scanning Tunneling Microscopy. *Science* **296**, 1838–1841 (2002).

120. Elsaesser, T. Introduction: Ultrafast Processes in Chemistry. *Chemical Reviews* **117**, 10621–10622 (2017).

121. Miwa, K., Imada, H., Kawahara, S. & Kim, Y. Effects of molecule-insulator interaction on geometric property of a single phthalocyanine molecule adsorbed on an ultrathin NaCl film. *Physical Review B* **93**, 165419 (2016).

122. Patera, L. L., Queck, F., Scheuerer, P., Moll, N. & Repp, J. Accessing a Charged Intermediate State Involved in the Excitation of Single Molecules. *Physical Review Letters* **123**, 016001 (2019).

123. Jiang, J., Bao, M., Rintoul, L. & Arnold, D. P. Vibrational spectroscopy of phthalocyanine and naphthalocyanine in sandwich-type (na)phthalocyaninato and porphyrinato rare earth complexes. *Coordination Chemistry Reviews* **250**, 424–448 (2006).

124. Tkatchenko, A. & Scheffler, M. Accurate Molecular Van Der Waals Interactions from Ground-State Electron Density and Free-Atom Reference Data. *Physical Review Letters* **102**, 073005 (2009).

125. Ruiz, V. G., Liu, W., Zojer, E., Scheffler, M. & Tkatchenko, A. Density-Functional Theory with Screened van der Waals Interactions for the Modeling of Hybrid Inorganic-Organic Systems. *Physical Review Letters* **108**, 146103 (2012).

126. Yoshida, K., Shibata, K. & Hirakawa, K. Terahertz Field Enhancement and Photon-Assisted Tunneling in Single-Molecule Transistors. *Physical Review Letters* **115**, 138302 (2015).

127. Esmann, M. *et al.* Vectorial near-field coupling. *Nature Nanotechnology* **14**, 698–704 (2019).

128. Benz, F. *et al.* Single-molecule optomechanics in "picocavities". *Science* **354**, 726–729 (2016).

129. Barnes, W. L., Dereux, A. & Ebbesen, T. W. Surface plasmon subwavelength optics. *Nature* **424**, 824–830 (2003).

130. Böckmann, H. *et al.* Near-Field Enhanced Photochemistry of Single Molecules in a Scanning Tunneling Microscope Junction. *Nano Letters* **18**, 152–157 (2018).

131. COMSOL Multiphysics ®, COMSOL AB, Stockholm, Sweden.

132. Ordal, M. A. *et al.* Optical properties of the metals Al, Co, Cu, Au, Fe, Pb, Ni, Pd, Pt, Ag, Ti, and W in the infrared and far infrared. *Applied Optics* **22**, 1099–1119 (1983).

133. Olmon, R. L. *et al.* Optical dielectric function of gold. *Physical Review B* **86**, 235147 (2012).

134. Lee, Y. S. *Principles of Terahertz Science and Technology* (Springer, 2009).

135. Li, H. H. Refractive Index of ZnS, ZnSe, and ZnTe and Its Wavelength and Temperature Derivatives. *Journal of Physical and Chemical Reference Data* **13**, 103–150 (1984).

136. Gallot, G., Zhang, J., McGowan, R. W., Jeon, T.-I. & Grischkowsky, D. Measurements of the THz absorption and dispersion of ZnTe and their relevance to the electro-optic detection of THz radiation. *Applied Physics Letters* **74**, 3450–3452 (1999).

137. Krishna, V. & Tully, J. C. Vibrational lifetimes of molecular adsorbates on metal surfaces. *The Journal of Chemical Physics* **125**, 054706 (2006).

138. Saalfrank, P., Juaristi, J. I., Alducin, M., Blanco-Rey, M. & Muiño, R. D. Vibrational lifetimes of hydrogen on lead films: An ab initio molecular dynamics with electronic friction (AIMDEF) study. *The Journal of Chemical Physics* **141**, 234702 (2014).

139. Petek, H. Photoexcitation of adsorbates on metal surfaces: One-step or three-step. *The Journal of Chemical Physics* **137**, 091704 (2012).

140. LaRue, J. L. *et al.* THz-Pulse-Induced Selective Catalytic CO Oxidation on Ru. *Physical Review Letters* **115**, 036103 (2015).

141. Neugebohren, J. *et al.* Velocity-resolved kinetics of site-specific carbon monoxide oxidation on platinum surfaces. *Nature* **558**, 280–283 (2018).

142. Shi, T., Cirac, J. I. & Demler, E. Ultrafast molecular dynamics in terahertz-STM experiments: Theoretical analysis using Anderson-Holstein model. *arXiv preprint* (2019). arXiv:1904.00932.

143. Repp, J., Meyer, G., Paavilainen, S., Olsson, F. E. & Persson, M. Imaging Bond Formation Between a Gold Atom and Pentacene on an Insulating Surface. *Science* **312**, 1196–1199 (2006).

144. Stigler, J., Ziegler, F., Gieseke, A., Gebhardt, J. C. M. & Rief, M. The Complex Folding Network of Single Calmodulin Molecules. *Science* **334**, 512–516 (2011).

145. Aragonès, A. C. *et al.* Electrostatic catalysis of a Diels-Alder reaction. *Nature* **531**, 88–91 (2016).

146. Giessibl, F. J. Advances in atomic force microscopy. *Reviews of Modern Physics* **75**, 949–983 (2003).

147. Giessibl, F. J., Hembacher, S., Bielefeldt, H. & Mannhart, J. Subatomic Features on the Silicon (111)-(7×7) Surface Observed by Atomic Force Microscopy. *Science* **289**, 422–425 (2000).

148. Jahng, J. *et al.* Ultrafast pump-probe force microscopy with nanoscale resolution. *Applied Physics Letters* **106**, 083113 (2015).

149. Schumacher, Z., Spielhofer, A., Miyahara, Y. & Grutter, P. The limit of time resolution in frequency modulation atomic force microscopy by a pump-probe approach. *Applied Physics Letters* **110**, 053111 (2017).

150. Knorr, M. *et al.* Phase-locked multi-terahertz electric fields exceeding 13 MV/cm at a 190 kHz repetition rate. *Optics Letters* **42**, 4367–4370 (2017).

151. Merkl, P. *et al.* Multibranch pulse synthesis and electro-optic detection of subcycle multi-terahertz electric fields. *Optics Letters* **44**, 5521–5524 (2019).

152. Yoshioka, K. *et al.* Subcycle mid-infrared coherent transients at 4 MHz repetition rate applicable to light-wave-driven scanning tunneling microscopy. *Optics Letters* **44**, 5350–5353 (2019).

153. Madan, I. *et al.* Evidence for carrier localization in the pseudogap state of cuprate superconductors from coherent quench experiments. *Nature Communications* **6**, 6958 (2015).

154. Corson, J., Mallozzi, R., Orenstein, J., Eckstein, J. N. & Bozovic, I. Vanishing of phase coherence in underdoped $Bi_2Sr_2CaCu_2O_{8+\delta}$. *Nature* **398**, 221–223 (1999).

155. Ropers, C. *et al.* Grating-Coupling of Surface Plasmons onto Metallic Tips: A Nanoconfined Light Source. *Nano Letters* **7**, 2784–2788 (2007).

156. Kravtsov, V., Ulbricht, R., Atkin, J. M. & Raschke, M. B. Plasmonic nanofocused four-wave mixing for femtosecond near-field imaging. *Nature Nanotechnology* **11**, 459–464 (2016).

157. Romming, N. *et al.* Writing and Deleting Single Magnetic Skyrmions. *Science* **341**, 636–639 (2013).

158. Sanvito, S. Molecular spintronics. *Chemical Society Reviews* **40**, 3336 (2011).

159. Siegert, B., Donarini, A. & Grifoni, M. Effects of spin-orbit coupling and many-body correlations in STM transport through copper phthalocyanine. *Beilstein Journal of Nanotechnology* **6**, 2452–2462 (2015).

160. Koller, S., Mayrhofer, L. & Grifoni, M. Spin-dependent transport through interacting graphene armchair nanoribbons. *New Journal of Physics* **12**, 033038 (2010).

161. Chen, K. & Arnold, F. H. Tuning the activity of an enzyme for unusual environments: sequential random mutagenesis of subtilisin E for catalysis in dimethylformamide. *Proceedings of the National Academy of Sciences* **90**, 5618–5622 (1993).

162. Packer, M. S. & Liu, D. R. Methods for the directed evolution of proteins. *Nature Reviews Genetics* **16**, 379–394 (2015).

163. Yang, K. K., Wu, Z. & Arnold, F. H. Machine-learning-guided directed evolution for protein engineering. *Nature Methods* **16**, 687–694 (2019).